HOKKAIDO UNIVERSITY

Title	Study on High-Temperature Corrosion of Ni-based Alloys in Atmosphere Containing Alkali Metal Chloride Vapor
Author(s)	HUBBY, 'IZZUDDIN
Citation	. ( ) 14228
Issue Date	2020-09-25
DOI	10.14943/doctoral.k14228
Doc URL	http://hdl.handle.net/2115/86932
Type	theses (doctoral)
File Information	Hubby_Izzuddin.pdf

Instructions for use

Study on High-Temperature Corrosion
of Ni-based Alloys
in Atmosphere Containing Alkali Metal Chloride Vapor

A Dissertation Submitted as Partial Fulfillment of the Requirement
for the Degree of Doctor of Philosophy in Engineering

Hubby 'Izzuddin

Division of Materials Science and Engineering
Graduate School of Engineering

北海道大学
HOKKAIDO UNIVERSITY

September 2020

TABLE OF CONTENTS

LIST OF TABLES

5

LIST OF FIGURES

8

ABSTRACT

In the waste incineration environments, the corrosion become the major problem due to high chlorine concentration in waste and its ability to cause rapid corrosion of metal components such as boiler tubes and heat exchanger tubes during the combustion process. During combustion, alkali salts are released into the oxidizing environments and react with the metallic component. The chlorine from salts strongly accelerates the corrosion/oxidation and results in faster degradation of materials. Thus, improving the corrosion resistance of the material used in the boiler component directly links to the lifetime of the plants. Ni based alloys and coatings are widely used for the boiler component because their excellent corrosion performance. Mo and Fe are widely used as alloying elements to improve the corrosion performance, however, the effect of those elements on the corrosion behavior of alloys in atmosphere containing alkali metal chlorides has not been fully understood, yet. Thus, in this study, the corrosion behavior of Ni20Cr-based alloy with Mo or Fe additions in atmospheres containing air and salt-vapor was evaluated.

This thesis consists of seven chapters in total. Chapter 1 introduced the research background, the literature studies, the scope and aims of research study, and the outline of study.

Chapter 2 described the details of experimental methods. Ni20Cr-based alloy were fabricated with variations of Mo (0, 1, 3, 7 in wt.%) and Fe (0, 4, 30 in wt.%) additions. The corrosion was performed at 570 ℃ in oxidizing atmosphere (air with salt vapor) and low oxidizing atmosphere (Ar with salt vapor).

Chapter 3 investigated the corrosion performance of Ni20Cr alloys with combinations of Mo and Fe additions and evaluated the combination effect of each element on corrosion performance of alloys. The results showed that combination of Mo and Fe additions gives better corrosion resistance to the Ni20Cr-based alloys. The corrosion performance was found to be improved with increased both Mo and Fe contents.

Chapter 4 investigated the effects of Mo addition on the corrosion behavior of Ni20Cr-based alloys in oxidizing-chlorine containing atmosphere. The Mo-free Ni20Cr-based alloy corroded with a high corrosion rate due to a formation of chromates. Chromate formation was considered to be the main reason to increase the corrosion rate, since it caused

breakdown of the protective Cr_2O_3 scale accompanied with generation of chlorine. The Mo addition has given better corrosion performance because it promoted NiO scale formation, which was able to suppress the chromate formation.

Chapter 5 investigated the effects of Mo on the corrosion behavior of Ni20Cr-based alloy in the low oxidizing atmosphere in order to confirm the mechanism proposed in the chapter 4. The corrosion mass gain of Mo-free Ni20Cr-based alloy decreased significantly comparing to that in the oxidizing-chlorine containing atmosphere. But the corrosion rate of the Mo-containing alloys was found to increase. Decreasing the corrosion rate in the Mo-free alloy was attributed by less chromate formation, by which the corrosion mechanism proposed in chapter 4 was confirmed.

Chapter 6 investigated the effects of Fe on the corrosion behavior of Ni20Cr-based alloy in the oxidizing atmosphere. Fe addition to Ni20Cr-based alloy was also found to improve the corrosion resistance in the oxidizing-chlorine containing atmosphere. Although the oxide scale structure formed on the Fe containing alloys were similar to that formed on the Fe-free alloy. Lesser extent of chromate formation due to the Fe oxide formation resulted in thinner internal Cr-chloride penetration and Cr-depleted zone. Thus, a continuous Cr_2O_3 scale was able to protect the alloy substrate.

In Chapter 7, the main conclusion of the research was discussed.

CHAPTER 1
INTRODUCTION

1.1 Current Status and Trend of Waste-to-Energy (WtE) Industry

Massive growth in the amounts of municipal solid waste (MSW) and biomass generated around the world in every year. World Bank estimated solid waste generated in the urban area globally were 0.68 billion tons/year at 2002, 1.2 billion tons/year at 2012 and up to 4.2 billion tons/year at 2025[1]. With such high solid waste generated, the demands of new waste to energy (WtE) power plants will always be increased, as shown in Fig. 1 where the number of municipal solid waste incineration (MSWI) capacity and plants globally has been accelerated from 1980 to 2015.
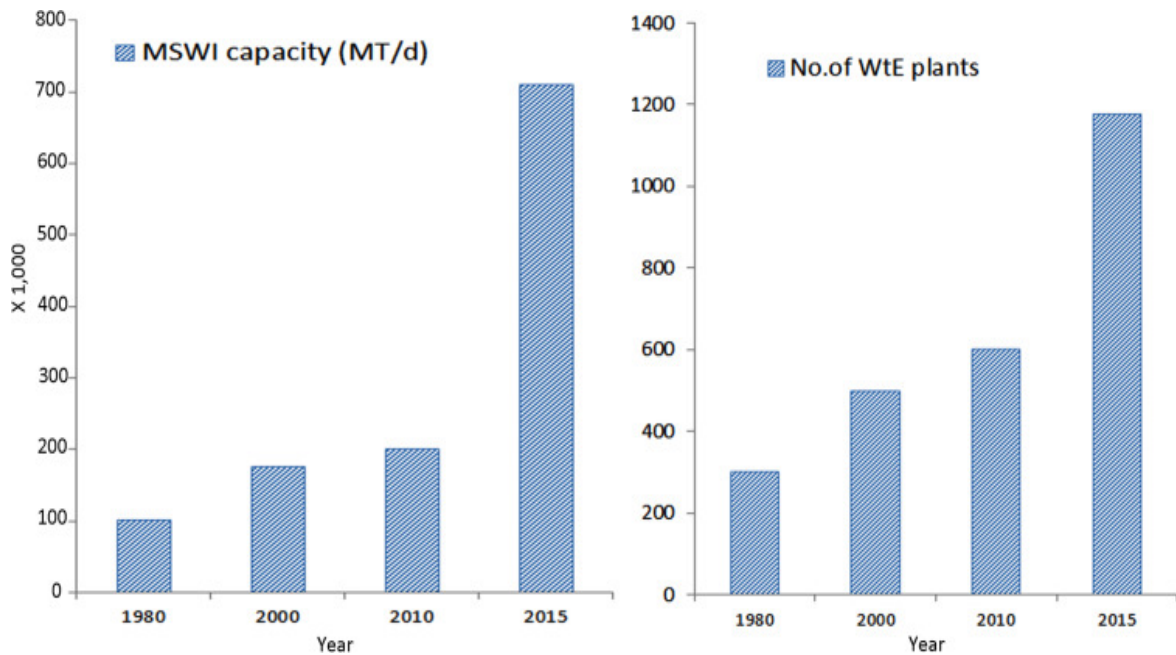
Fig. 1 Growth of MSWI globally between 1980 and 2015. Source [2].

However, closed to end of the 20th century, the growth expansion of MSWI in developed countries, some European countries and U.S. became decelerated as illustrated in Fig. 2. The deceleration happened mainly because the change of environmental policy with more strict emission control after United Nations Framework Convention on Climate Change (UNFCCC) at 1992. Later Japan also has reduced enlarging their MSWI after Kyoto

Protocol at 1997. But, China who just started the MWSI by end of the 20th century, strongly kept the MSWI enlarging capacity due to a less harmful and more effective option than landfill, and became the largest MSWI capacity in the world.
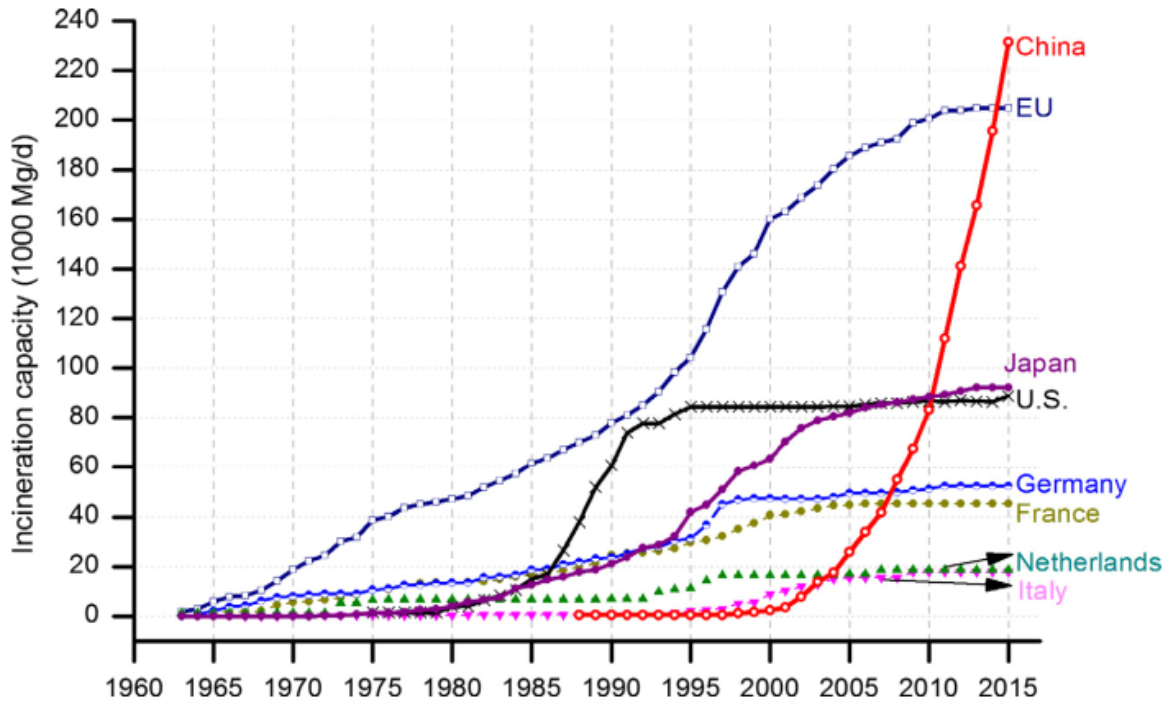
Fig. 2 Cumulative capacity of solid waste incineration in representative regions. Source [3].

For developed countries who have enough MSWI capacity, they began modernized and increased the utilization factor their incinerator. Table 1 shows that some countries has still not operate at its full strength. The International Renewable Agency has estimated that the world has a potential generating approximately 13 GW of energy from MSWI[4]. Because there are 75% of global MSW which are still being landfilled. Thus, the trend of MSWI will continue to rise globally as this is the most effective option to reduce generated waste with additional benefit in providing renewable energy[2].

Table 1 Status of MSW incineration around the world until 2015. Source [3].

Region	Number		Total capacity (Mg/d)	Average capacity (Mg/d)		Amount of MSW incineration (10³ Mg/a)	Utilization rate (%)
	Plants	Incinerators		Plant	Incinerator		
China (2015)	268	552	231,600	864	420	61,755	80
EU (2012)	469	917	207,104	442	226	59,023	85
Germany	79	192	52,554	665	274	17,192	98
France	127	248	45,334	357	183	11,951	79
Netherlands	13	42	18,660	1435	444	4515	73
Italy	52	97	17,825	343	184	5529	93
Sweden	34	67	14,477	426	216	2233	46
Denmark	29	64	10,900	376	170	2307	63
U.S. (2014)	80	210	88,765	1110	423	29,665	100
Japan (2013)	234	551	92,203	394	167	33,729	59
South Korea (2013)	39	72	13,580	348	189	4475	99
Taiwan area (2006)	24	62	24,650	1027	398	4036	49
Other regions (2013)	65	144	49,903	768	347	—	—
Total	*1179*	*2508*	*707,805*	*600*	*282*	—	—

1.2   Incineration Technologies in The WtE

There are some methods of the conversion process to produce energy/electricity from MSW: thermal conversion, biological conversion and landfilling with gas recovery[5]. The thermal conversion is the most common method of waste disposal treatment due to the ability to reduce the waste mass and volume up to 70% and 90% respectively, and has the highest electric generation efficiency about 30-31% and 20-24% in large and small-medium plan respectively[6].

Table 2 Typical reaction and products of thermal conversion methods[5].

Parameters		Incineration	Pyrolysis	Gasification
Principle		Full oxidative combustion	Thermal degradation of organic material in the absence of oxygen	Partial oxidation
Operating temperature (°C)		850–1200	400–800	800–1600
Atmosphere		Presence of sufficient oxygen	Absence of oxygen	Controlled supply of oxygen
Reaction products	Solid	Bottom ash, fly ash, slag, other non-combustible substances like metals and glass	Ash, char (combination of non-combustible and carbon)	Ash, slag
	Liquid		Condensate of pyrolysis gas (pyrolysis oil, wax, tar)	
	Gas	CO_2, H_2O, O_2, N_2	Pyrolysis gas (H_2, CO, hydrocarbons, H_2O, N_2)	Syngas (H_2, CO, CO_2, CH_4, H_2O, N_2)
Pre-treatment		Not necessary	Required	Required
Raw MSW		Usually preferred	Usually not preferred	Usually not preferred

In the thermal conversion method, dry waste with low moisture content and biomass were transformed into energy/electricity by employing process at high temperature, including incineration, pyrolysis and gasification, as shown in Table 2. Thermal conversion sometimes was applied to Refuse Derived Fuel (RDF) which is combustible material with high calorie value. Operating temperature and quantity of oxygen in the atmosphere are the main difference of these technologies. Consequently, the final product might be different, either CO_2 and water as maximum heat generation or intermediate products e.g. hydrocarbons and syngas[5,7].

The incineration is the first thermal conversion method since late of 19th century and was initially used for volume reduction and protecting the men and environment from the hazardous waste[9]. Until now, the incineration was still the most applied thermal conversion method due to its reliability and economically. MSW or industrial waste (IW) can directly feed to be burned directly to produce electricity, without any pre-treatment.

Other advantageous, the incineration process produces excess solid products as bottom and fly ash which can be utilized in road construction, cement production and recovery of ferrous and non-ferrous substance [5].
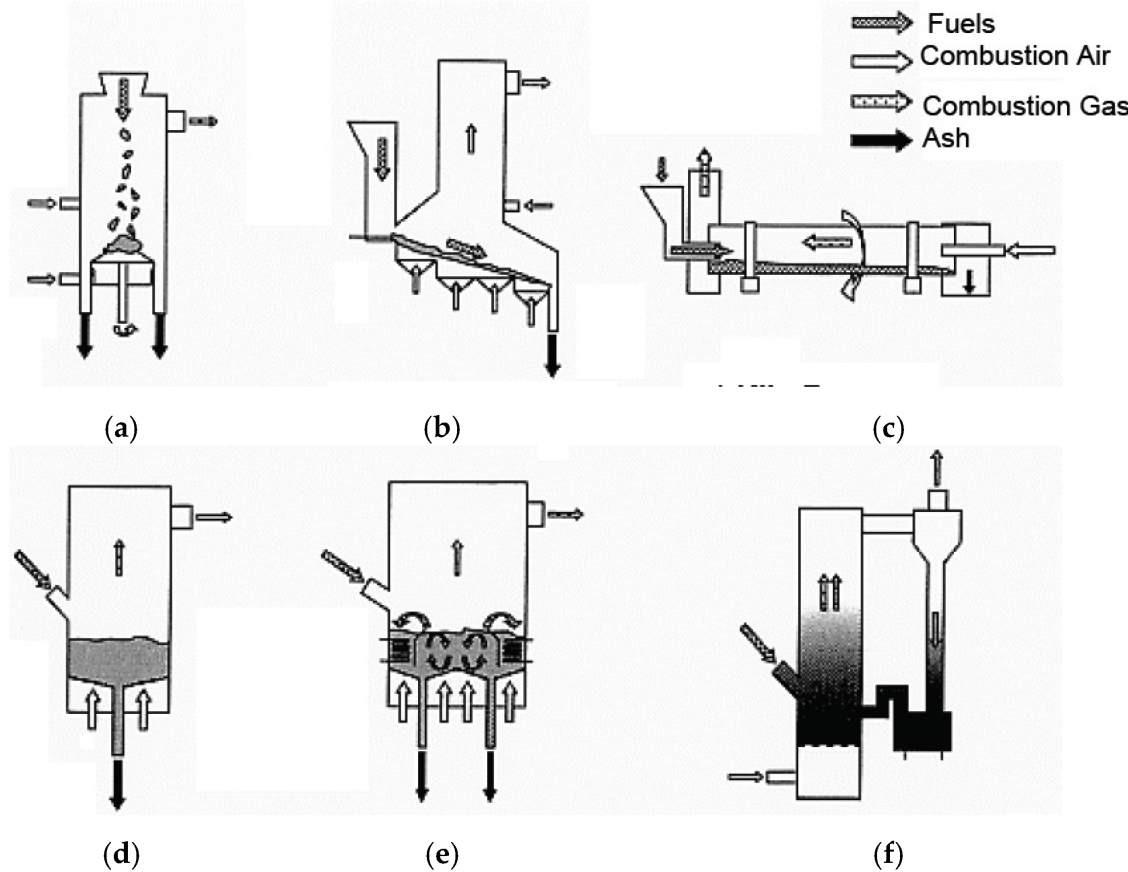
Fig. 3 Schematic illustration of typical combustion systems in WTE and biomass boilers. (a) Fixed Stoker; (b) Moving Stoker; (c) Kiln Furnace; (d) Bubbling Fluidized (BFBC); (e) Inside Circulated Fluidized Bed (ICFBC); (f) Outside Circulated Fluidized Bed (OCFBC)[8].

Until now, the incinerator was developed into main three types, e.g. stoker, rotary kiln furnace and fluidized bed incinerator as shown in Fig. 3. The main difference between these types are the different bed shape and additional pre-processing waste before combustion process in the incinerator. Other than these, any of type has the same configuration.

In the moving stoker type, as illustrated in Fig. 4, overhead crane grabs the waste and drop it into the hopper, the waste material slowly descends to the combustion chamber while is pushed by a piston onto the moving grate until end of the grate. During this movement, the waste was combusted with air which was injected from the bottom part of

incinerator. The waste is combusted inside the incinerator and the generated excess heat is recovered by the boiler, economizer and superheater leading to the steam turbine to generate the electricity. Meanwhile, the exhaust gas is purified by exhaust gas treatment and dust removal, then is collected into the smokestack. Ash, slag and incombustible waste are mostly discharged through space between the grate or collected from the end of grate. A part of ash is flying in the flue gas and collected in the bag filter as flying ash.
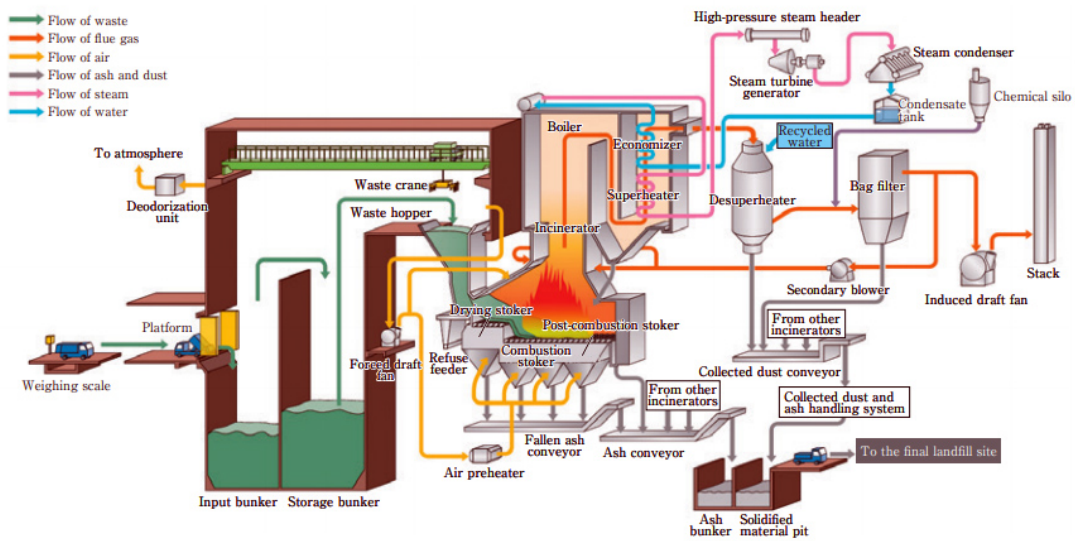
Fig. 4 Schematic process flow of typical MSW incinerator[10].

In the fluidized bed incinerator, the waste material needs to undergo shredding and size reduction prior the combustion process, apart the basic separation[2]. Then, in the combustion chamber, the waste is crushed and mixed with hot bed material while moving/circulating together with high velocity pressurized air, dried and partially incinerated. This is the reason that the fluidized bed is the best to process heterogenous waste material. The remaining fractions are incinerated above the combustion chamber in the freeboard. Later, the ash is removed with the flue gas. The fluidized bed was also divided into three types[7]:

a) Bubbling Fluidized (BFBC)

In BFBC, as shown Fig. 3d, the bed media and fine waste material are fluidized from the bottom of the bed with high-pressurized air by distribution of gas nozzle with

velocity between 1-3 m/s. Under this condition, the bed material is fully fluidized and behave like boiling liquid.

b) Inside Circulated Fluidized Bed (ICFBC)

ICFBC technology uses higher velocity of high-pressurized than in BFBC, in a range 3 up to 9 m/s. Inside the ICFB, as shown in Fig. 3e., a partition wall is added to separate the main combustion and heat recovery cell. With the partition wall, the circulation flow in the hat recovery cell become an opposite direction as in the combustion cell and is maintained by the fluidizing air flow which was supplied from the bottom edge of the heat recovery cell[11]. Thus, there are 3 circulation zone in the ICFB: 1) internal circulation inside the combustion cell, 2) circulation to the heat exchange cell, and 3) circulation char back to the main combustion cell. With the heat exchange tubes are installed inside the heat recovery cell, the bed temperature can be maintained between 600-700 °C[12].

c) Outside Circulated Fluidized Bed (OCFBC)

OCFBC is similar with ICFBC but with additional a heat exchange chamber outside the main combustion chamber, thus the fine particles of bed and waste materials are circulating through these 2 chambers, as shown in Fig 3f. The bed temperature is maintained by ash circulation.

1.3 Corrosion Problems in The WtE Incinerators

As explained in the previous section, most developed countries now have stopped enlarging MSW capacity or building a new MSW plant since end of 20th century due to a new emission policy. With this condition, increasing the utilization of current plant, and improving the electric generation efficiency through increasing steam-operational temperature are two options which are most taken in WtE industry. Nowadays, current steam temperature of the fired boiler for grate stoker MSW, fluidized bed MSW, grate stoker biomass and CFB for biomass can reach 420 °C, 470 °C, 500 °C and 545 °C, as shown in Fig. 5.

In MSW, various type of waste can be found such as organic waste, paper, plastic, woods, glass, incombustible waste, metals, etc. Other than large amount of moisture and ash, these kind of wastes contain sulfur, chlorine, alkali metals (Na, K), alkali earth metal

(Ca, Mg), heavy metals and other[14,15]. Biomass fuels and solid fuels (RDF and RPF) which are usually used in the fluidized bed plant contain high amount of chlorine and sulfur with alkali metal and alkali earth metal as contaminations[8]. Compared with sulfur, the amount of chlorine in the waste is much higher [8,10,16–20]. Table 3 shows the amount chlorine in the solid waste.
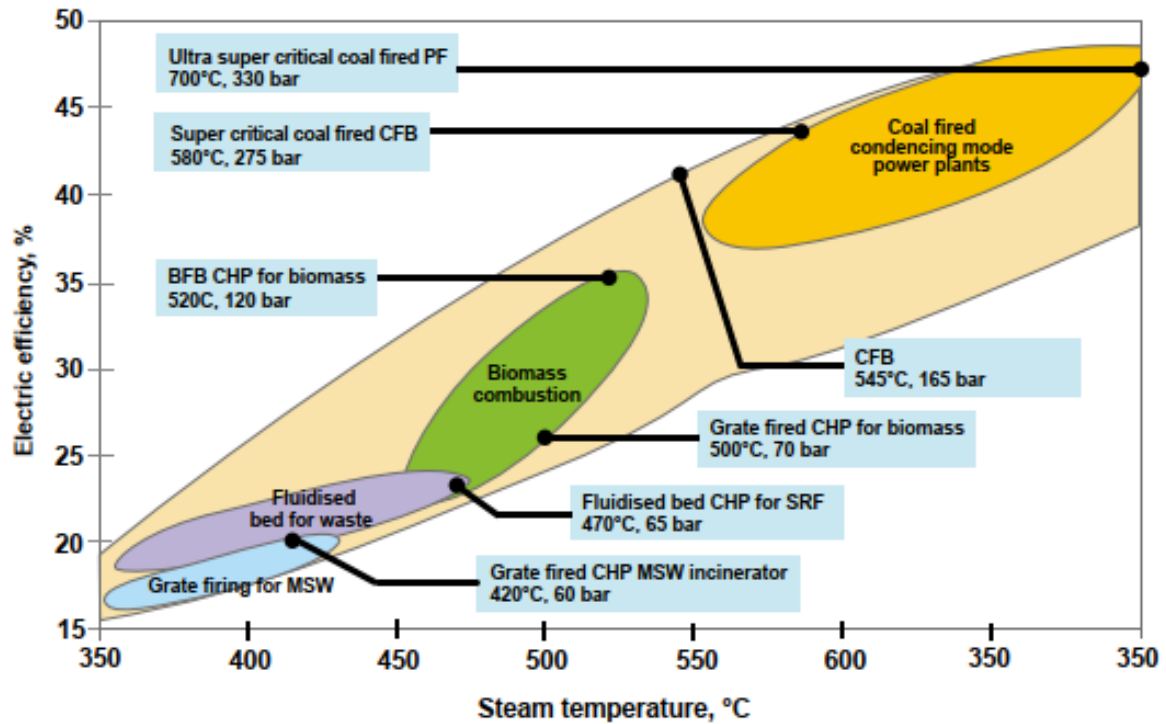
Fig. 5 Indicative range of electric efficiency vs steam temperature for different fired boiler application[13].

When waste from these types of sources is burned in the stoker incinerator under typical combustion condition (i.e. in the presence of H_2O, O_2, N_2), the completed burned waste become ash, meanwhile incomplete burned waste was discharged through space between the grate or collected from the end of grate. During the combustion, alkali metals (Na, K and Ca) were released during combustion and become gaseous alkali metals [21]. The ash which contains chlorine together with gaseous alkali metals flies in the flue gas from the incinerator and enter the waste heating boiler. Some of these reacted with sulfate and become gaseous alkali metal sulfate. The gas temperature decreases, and the alkali salt-sulfate vapor condense onto flying ash which then deposits onto the heating surface of boiler and superheater tubes[22]. In such high temperature, this create chance for the chlorine and sulfate corrosion products to be formed. Whereas, in the ICFBC plant, the bed material, the burned chlorine containing waste and the gaseous alkali salt vapor circulate continuously

inside the combustion chamber and the heat recovery cell. In this heat recovery cell, while circulating and gas temperature decrease, the bed material with condensed chlorine containing waste with alkali salt vapor will hit eventually the installed heat exchange tubes resulting in chlorine corrosion on the exchange tube surface. The sulfur dioxide gas formed during combustion in the fluidized bed is much smaller than that of in the stoker [21,23]. Similar with the boiler tube in the stoker, the ash deposit will start the corrosion process on heating the tube surface. With this condition, at such high temperature and long operation time, the corrosion become accelerated and the tube materials will be degraded rapidly [24–26]. If steam operation temperature in the boiler tube is increased to improve the electric generation efficiency, then the chlorine corrosion become more damaging for the tube material and cause bigger problem in the waste-to-energy power plant industry.

Table 3 The amount chlorine in the solid waste[20]

Type	Sources	Examples	Chlorine content (wt.%, dry basis)
Inorganic Cl sources	Forestry residue (FR)	Willow wood, hybrid poplar, sawdust, woody products (e.g., paper and cardboard)	0.01–0.10
	Agriculture residue (AR)	Rice straw, wheat straw, corn stover	0.10–0.72
	Food waste (FW)		0.03–1.38
Organic Cl sources	Plastics	Polyvinyl chloride (PVC)	46.00–56.70
		Daily plastic products (packaging, non-packaging)	0.25–6.28
		Medical waste	1.10–2.10
	Other products	Textiles, rubber, leather, electronic waste	0.40–2.70
Mixed Cl sources	Municipal solid waste (MSW)	A mixture of plastics, FW, textiles, papers…	0.50–1.00
	Refuse derived fuel (RDF)/solid recovered fuels (SRF)		0.15-1.58
	Sewage sludge		0.03–0.27

1.4 High Temperature Corrosion in Chlorine Containing Atmospheres

1.4.1 Thermodynamics and Mechanisms of High Temperature Corrosion in Chlorine Containing Atmospheres

When chlorine is able to penetrate into metal substrate and react with a metal element, this will lead to the formation of a metal chloride. Because chlorides are less stable than oxide and have low melting point and high vapor pressure as shown in Table 4 and Fig. 6, the metal chloride particularly at high temperature is easily sublimated into a volatile compound. The metal chloride reaction can be written as follow:

$$xM(s) + \frac{y}{2}Cl_2(g) = M_xCl_y(s) = M_xCl_y(g) \qquad (1)$$
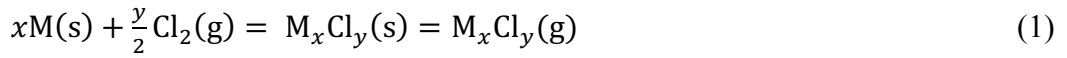
The free energy of the reaction ΔG can be written as:

$$\Delta G = \Delta G° + RT \ln K \qquad (2)$$

Table 4 Physical properties of some metal chlorides and oxichlorides (T_S = Melting point; T_K = Boiling point, T_4 = Temp. where chloride vapor pressure > 10^{-4} bar (dec. = decomposes, subl. = sublimation) [19]

Chloride	T_s (°C)	T_K (°C)	T_4 (°C)
$CrCl_2$	824		813.9
$CrCl_3$	ca. 1150	subl. 1300	531.7
CrO_2Cl_2	-96.5	117	
$FeCl_2$	670 – 674	subl.	527
$FeCl_3$	306	dec. 315	165.3
$MoCl_3$	dec.		137.2
$MoCl_4$	dec.		137.2
$MoCl_5$	194	268	63.8
MoO_2Cl_2	subl.		53.2
$NiCl_2$	1001	subl. 973	593

The thermodynamic stability of each phase from the eq. 1 can be determined by calculation of the reaction constant K with following equation:

$$K_p = \frac{P_{M_xCl_y}}{(P_{Cl_2})^{\frac{y}{2}}(a_M)^x} \qquad (3)$$

Where $P_{M_xCl_y}$ and P_{Cl_2} are the partial pressure of the metal chloride and chlorine, respectively, and a_M is the metal activity (equal 1 for a pure metal).
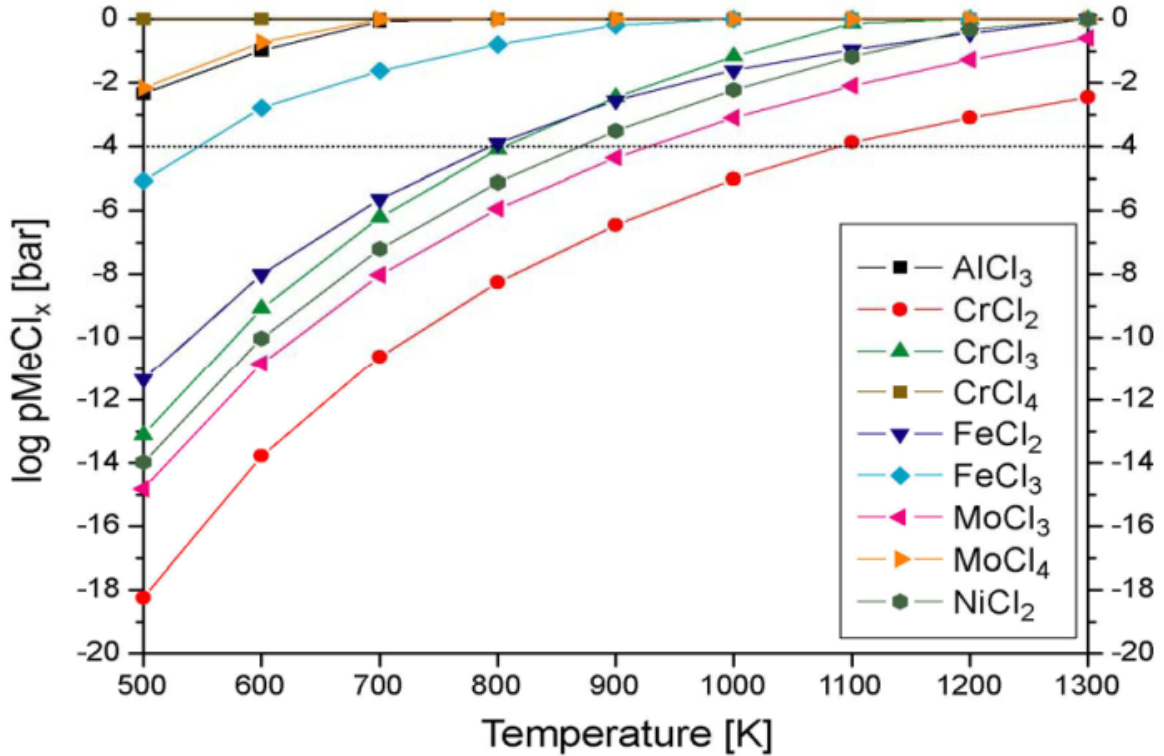
Fig. 6 Vapor pressure $P_{M_xCl_y}$ of several metal chlorides above the solid metal chloride phase as a function of temperature together with the ''limiting line'' of $P_{M_xCl_y} = 10^{-4}$ bar

In the incinerator power plant, particularly in fluidized bed plant where the atmosphere in the combustion chamber contain high oxygen, called as "oxidizing-chloridizing" atmosphere. The mechanism of corrosion in the oxidizing-chloridizing atmosphere is also often explained via the "chlorine cycle" or "active oxidation" mechanism, where chlorine (Cl_2) is able to penetrate the oxide layer ($M_aO_b(s)$) through pores and/or cracks and reaches the metal substrate where the Cl_2 reacts with the metal to form a volatile metal chloride using the reaction (1), as shown in Fig. 7 [24,29]. Owing to the high vapor pressure of metal chlorides, metal chlorides ($M_xCl_y(g)$) are readily evaporated and oxidized at the surface of oxide scale where the partial pressure of oxygen is high, using reaction (4). Chlorine is produced by this reaction and used for further chlorination. This "active oxidation" process is very rapid [30,31]. Several studies have also reported that alkali ions can induce breaking down the protective oxide scale [32–36].

$$aM_xCl_y(g) + \frac{bx}{2}O_2(g) = xM_aO_b(s) + \frac{ay}{2}Cl_2(g) \qquad (4)$$
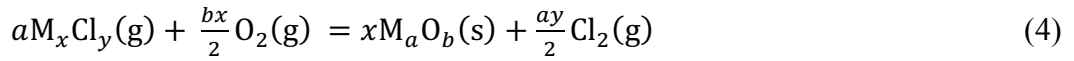
where the constant K_e of the reaction:

$$k_e = \frac{(P_{Cl_2})^{\frac{a}{2}}}{(P_{M_xCl_y})^a(P_{O_2})^{\frac{bx}{2}}} \qquad (5)$$
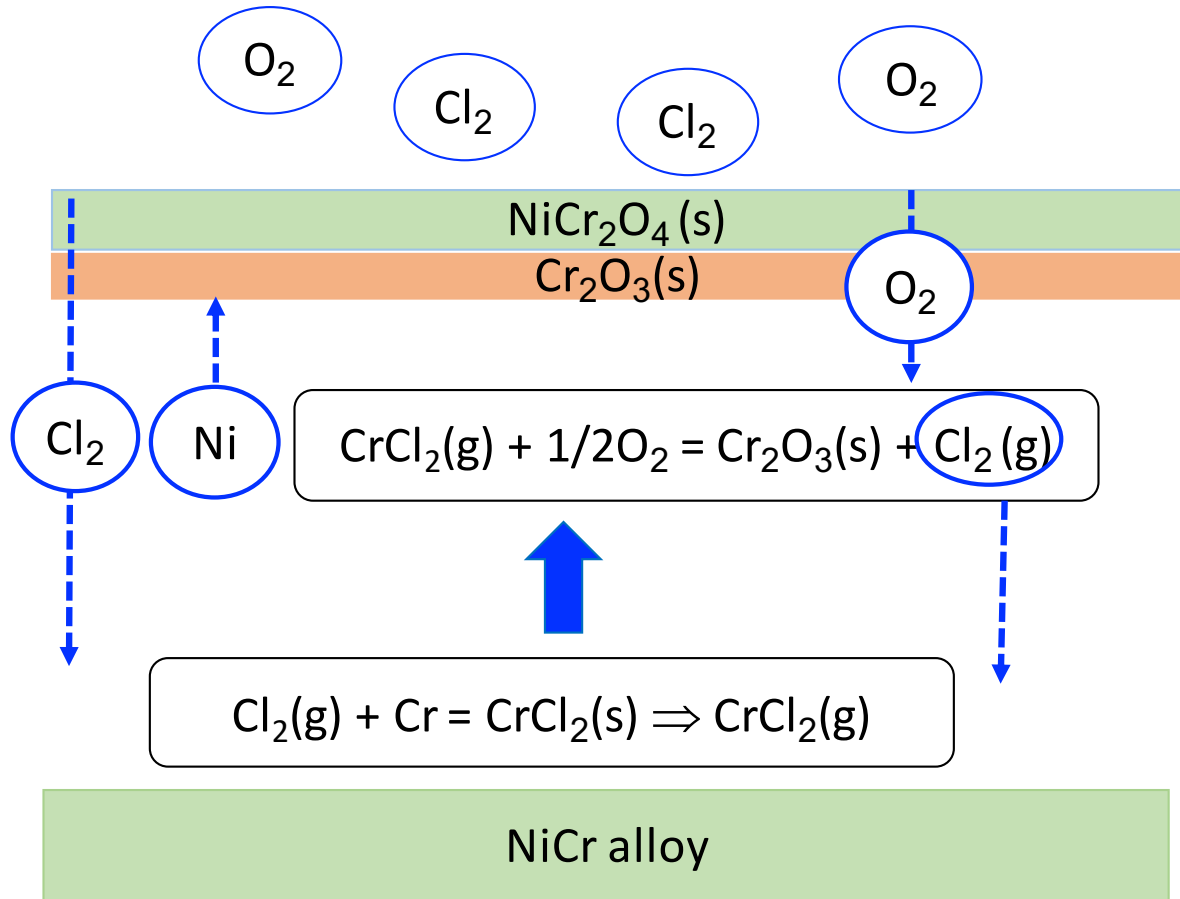
Fig. 7 Schematic of "active oxidation" mechanism in oxidizing-chloridizing atmosphere

For such mixed oxidation-chlorination, a paralinear kinetics called Tedmon equation[37–39] which combines a parabolic rate equation of oxide scale growth and a linear rate equation for scale consumption through chlorination, as shown in eq. 6

$$\frac{dx}{dt} = \frac{k_p}{x} - k_e \qquad (6)$$

where x is the mass change of the sample, t the time, k_p parabolic rate constant of the oxide scale growth and k_e the linear rate constant of evaporation of metal chlorides.

Based on this eq. (6), the mass change can be determined as total mass of oxygen in the oxide scale and metal loss due to evaporation of metal chlorides. However, because the kinetics of growth of oxide scale are usually much slower compared with kinetics of evaporation of metal chlorides. The contribution of oxidation may often be neglected.

The mass transfer coefficient $h_{\text{M}_x\text{Cl}_y}$ of the metal chloride in gas phase has predicted (in cm/s). The rate of evaporation rate of metal chloride is affected with the gas flow rate during the corrosion test.

$$h_{\text{M}_x\text{Cl}_y} = 0.664 \; \frac{D_{\text{M}_x\text{Cl}_y}^{\frac{2}{3}}}{\vartheta^{\frac{1}{6}}} \left(\frac{v}{L}\right) \tag{7}$$

where, $D_{\text{M}_x\text{Cl}_y}$ is diffusion coefficient of metal chloride in the gas phase (cm^2/s), L length of the sample (cm) and ϑ gas kinematic viscosity, v the gas velocity.

1.4.2 Previous Studies of Alloying Effects in The Chlorine Containing Atmosphere

1.4.2.1 Nickel

Ni-based alloys and coatings are widely used in the waste-to-energy industry due to their good mechanical properties and high temperature corrosion resistance particularly in oxidizing-chlorine containing environment. Based on the diagram in Fig. 8, the volatile metal chloride product from the chlorine reaction with Ni at 570°C, is only NiCl$_2$. Because the characteristics of NiCl$_2$ which has higher melting point and lower vapor pressure than those of the iron chloride (FeCl$_2$/FeCl$_3$), Ni-based alloy is more superior than that of Fe-based alloy in this environment.

Based on the table 4, NiCl$_2$ has a critical vapor pressure of 10^{-4} bar at 593°C. The value of this critical pressure corresponds to a metal consumption rate of 1 mm·y^{-1} [27]. Below this pressure, the volatile corrosion products are still being formed but to a lesser extent. Thus, pure Ni should able to resist low chlorine corrosion attack below 593°C.
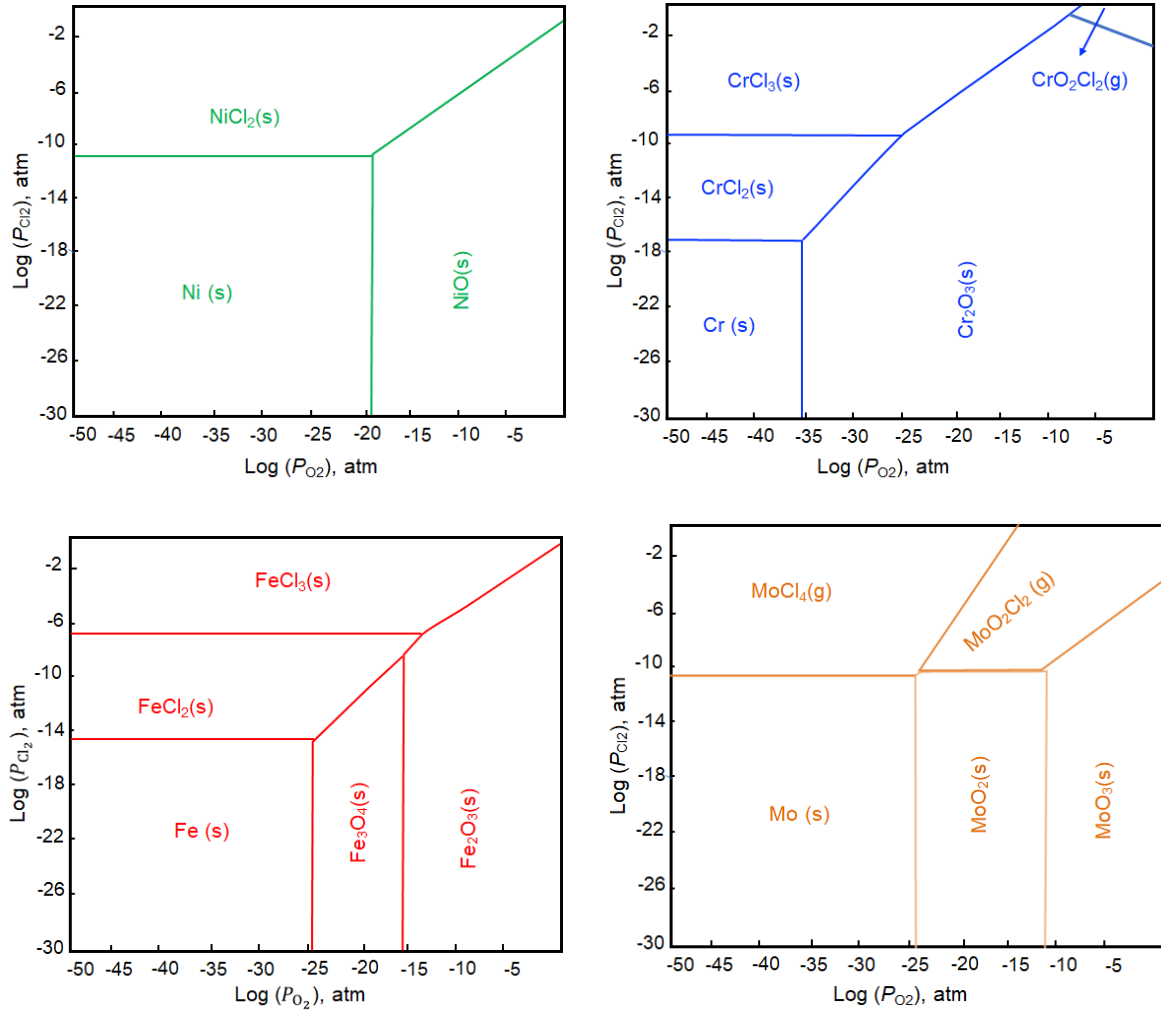
Fig. 8 Quasi-stability diagrams for oxidizing-chlorine environments at 570°C for the alloying elements: (a) Ni, (b) Fe, (c) Cr, (d) Al, and (e) Mo.

1.4.2.2 Chromium

In the oxidizing-chlorine containing environment, Cr is the most common element used against chlorine corrosion attack due to the formation of a protective scale of Cr_2O_3. This is the most advantages for using Cr compared with Fe and Ni which could not produce a protective oxide scale. Therefore, Cr usually become an alloying element together with Ni and or Fe. In oxygen containing atmosphere, NiCr alloys with more than 8 wt.% of Cr usually are able to form Cr_2O_3 and or $NiCr_2O_4$ spinel which has much better corrosion resistance than those of unalloyed Ni [36,40,41]. Meanwhile, FeCr alloy with 20 wt.% Cr is also able to form Cr_2O_3 and has good corrosion resistance at 900 K[42].

Based on Fig. 8, a reaction between Cr and chlorine will form metal chlorides i.e. $CrCl_2$, $CrCl_3$, and a metal oxychloride CrO_2Cl_2. With a very low melting point and higher chlorine and oxygen pressure (shown in Fig. 8), the $CrO_2Cl_2(g)$ become a very aggressive gas and the damage caused by $CrO_2Cl_2(g)$ has been reported[40,43,44]. Although the direct reaction between Cr, oxygen and chlorine is unlikely occurred, but the $CrO_2Cl_2(g)$ is thermodynamically favored[27]. $CrCl_3$ has slightly lower temperature to reach critical vapor pressure of 10^{-4} bar, at 531°C, and higher vapor pressure than $NiCl_2$. Thus, $CrCl_3$ will be easily formed and evaporated when expose Cr-based alloys in the oxidzing-chlorine contaning atmosphere at 570°C, compared to Ni.

1.4.2.3 Iron

Although Fe-based alloy has less corrosion resistance compared to Ni and Cr, but Fe has better mechanical strength and cheaper price than both alloys. Thus, Fe is commonly used as an alloying element. Due to lower temperature of all Fe chlorides, $FeCl_2$ and $FeCl_3$ (as shown in Fig. 8), to reach the critical vapor pressure of 10^{-4} bar, and their higher vapor pressure, the Fe seems to have lower corrosion resistance than Ni and Mo in oxidizing-chlorine containing atmosphere.

Numerous studies have reported the effect of Fe on corrosion behavior in atmospheres containing oxygen and chlorine[28,34,42,45–49]. In atmospheres of air or Ar-20%O_2 containing 1-2% Cl_2, formation of a porous iron oxide scale and inner chromia scale were frequently observed on alloys containing Fe, Ni and Cr (Ni, Cr $\geq$ 20 wt.%) upon exposure to temperatures of 650-1000 °C. Chlorine can easily penetrate into this porous iron oxide scale, and reacts with the metallic material to form volatile metal chlorides, which accelerates the corrosion rate of the alloys[28,45–47]. However, in the presence of alkali metal chlorides (e.g. KCl), the addition of 4-7 wt.% Fe to Ni-based alloys containing 20-27 wt.% Cr was reported to improve the corrosion resistance during exposure to an O_2+H_2O environment at 600 °C, despite the formation of an outer porous iron oxide scale on the alloys. Furthermore, in static air, Ni-based alloys with 4 wt.% Fe were reported to have better corrosion resistance than Fe-based alloys with Ni and Cr contents of 28-30 wt.%[48,49]. However, the mechanism of the effect of Fe alloying on the corrosion behavior has not yet been completely understood.

1.4.2.4 Molybdenum

Mo alloying is widely accepted to enhance the high-temperature corrosion resistance of Ni-based alloys and coatings [50–52], especially in reducing chlorine-containing environments [27,28,53,54]. However, in oxidizing chlorine-containing environments, a high Mo content (>20 wt. %) was reported to decrease the corrosion resistance due to the formation of MoO_2Cl_2 [28]. In an oxidizing chlorine-containing atmosphere, some studies using air/O_2 containing chlorine have demonstrated that Mo alloying accelerated corrosion [28,53], whereas other studies using O_2 and HCl gas mixtures in both the presence and absence of KCl deposits indicated that Mo alloying enhanced the corrosion resistance of the alloy [36,55]. All the Mo chlorides and oxychlorides have much lower melting point and much higher vapor pressure compared with Ni, Cr and Fe. However, similar to Fe, the mechanism of the effect of Mo alloying on the corrosion behavior has also not yet been completely understood.

1.5 The Scope and Aim of This Study

This study is a part of consortium project to develop a coating material for the heat exchange tube in the ICFBC plant which has a steam temperature about 570 °C (see Fig. 5). Inside the heat exchange cell, the bed materials with condensed salts containing waste circulate continuously in the oxidizing-chlorine containing atmosphere with salt vapor mixture from gaseous alkali metal. While circulating, the bed materials also simultaneously hit the surface of heat exchange tube resulting in the chlorine corrosion and erosion on the tube surface. This condition become major problem in the WtE industry, and based on the literature study, the mechanism of chlorine has not yet clearly understood.

In order to prolong the lifetime of heat exchange tube for the ICFB application, the coating is the most common option to be chosen, and NiCr based alloy is widely chosen due to its ability to form a protective Cr-oxide scale which is proven in this oxidizing chlorine containing atmosphere. It is well known that after formation of a protective Cr_2O_3 scale, there will be a Cr-depleted zone beneath the scale. Thus, it is mandatory to have a sufficient Cr content to maintain the Cr_2O_3 scale formation. Therefore, a high Cr content with 20 wt.% is chosen for the NiCr-based alloy.

With these reasons, the scope of this dissertation study is to evaluate the corrosion behavior of Ni20Cr based alloy in atmospheres containing air and salt-vapor at 570 °C. In particular, effects of elements such as Mo and Fe which are well known with their good high temperature corrosion resistance were studied.

The aims of this study are:

1) To assess the corrosion kinetics of the alloys in the chlorine containing atmosphere.

2) To understand the mechanism of corrosion in atmospheres containing chlorine.

3) To evaluate the effect of alloying elements, such as Mo and Fe, on corrosion behavior of Ni20Cr-xMoyFe alloys

1.6   Outline of the thesis

The content of this thesis is divided into seven chapters. The first chapter describes briefly about current status and trend of Waste-to-Energy Industry (WtE), different types of incineration technologies applied in the WtE industry, corrosion problems happened in the WtE incinerators, literature studies of high temperature corrosion in the chlorine containing atmosphere from its thermodynamics, mechanisms and alloying effects on the corrosion behaviors. Chapter 2 explains details experimental methods used in this study: the sample preparations, parameters and conditions of the corrosion tests, analysis and calculation methods of the corrosion performance after corrosion tests, and the introductions of different type of analysis techniques for surface morphologies and cross-sections which were applied during this study. In chapter 3, the effects of Fe and Mo addition on the corrosion behavior of Ni20Cr-based alloys were assessed in the air with $NaCl$-KCl-$CaCl_2$ vapor. Chapter 4 explains the experimental results on effects of Mo in the air with $NaCl$-KCl-$CaCl_2$ vapor respectively in the kinetics and mechanisms of corrosion, and the alloying effects. In order to confirm the alloying effects of Mo on the corrosion behavior in the air with $NaCl$-KCl-$CaCl_2$ vapor, chapter 5 explains the experimental results on effects of Mo in the Ar with $NaCl$-KCl-$CaCl_2$ vapor respectively in the kinetics and mechanisms of corrosion, and the alloying effects. The experimental results on effects of Fe in the air with $NaCl$-KCl-$CaCl_2$ vapor respectively in the kinetics and mechanisms of corrosion, and the alloying effects were exhibited in chapter 6. The last chapter summarizes the results of this study which were explained in the previous chapters as a general conclusion.

CHAPTER 2
EXPERIMENTAL METHODS

2.1   Sample Preparations

Ni20Cr-xMoyFe alloy (in wt. %) with and without various Mo contents (1, 3 or 7 wt. %) and Fe contents (4, or 30 wt.%) were prepared by Ar arc-melting using high-purity metals (ca. 99.99 %). The alloy ingots were homogenized at 1200°C for 48 h under vacuum. Specimens with a thickness of approximately 1 mm were cut from the homogenized ingots, ground using SiC paper, and finished with 3 μm diamond paste. Prior to corrosion tests, the specimens were ultrasonically cleaned in acetone for 15 min.

2.2   Corrosion Test

The corrosion tests were performed using a two-heat-zones furnace, as illustrated in Fig. 1. The corrosion tests were conducted at 570°C for up to 100 h in: a) an oxidizing-chlorine containing atmosphere with air + salt-vapor mixture); b) a low oxidizing-chlorine containing atmosphere with argon + salt-vapor mixture). An alkali-salt mixture composed of 40% NaCl + 40% KCl + 20% $CaCl_2$ (mol %) was used as the source of the salt-vapor. During the tests, the salt mixture was placed upstream of the specimens with the respect of the gas flow with a linear velocity of 0.33 cm/sec at 600°C. After the given corrosion time (25, 50, or 100 h), the corrosion mass change was measured at room temperature. A fresh salt mixture was used for each corrosion cycle.
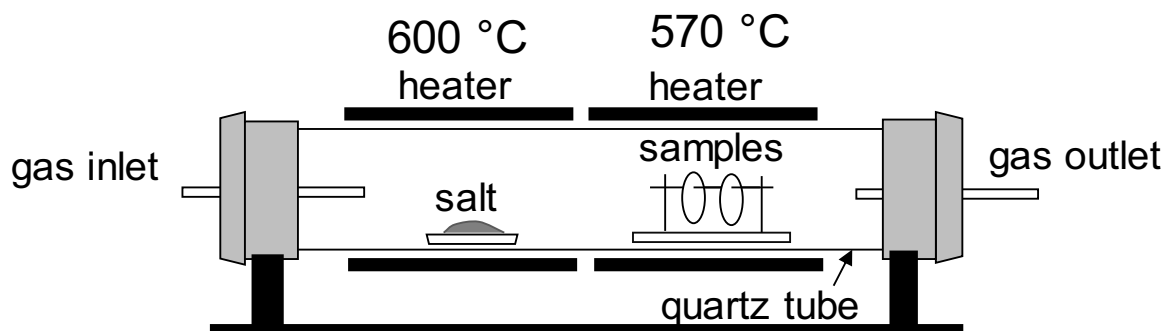
Fig. 9 Schematic depiction of the two-heat-zone furnace used for the corrosion tests in an air + salt-vapor environment.

2.3   Analysis of Corrosion Performance

For subsequent investigation of the corrosion performance, all reaction products formed on the corroded samples were removed by chemical treatments based on ISO 17248:2015(E) (see Table 5.). This chemical treatment procedure was performed to measure the total consumed mass or mass loss due to corrosion.

Table 5 Chemical treatment procedure based on ISO 17248:2015(E)

Chemical agents	Total time	Temperature
Step1: 90 g of sodium hydroxide (NaOH) 15 g of potassium permanganate (KMnO₄) Distilled water to make 500 ml	30 min	Boiling
Step 2: 50 gr ammonium citrate ((NH₄)₂C₆H₆O₇) Distilled water to make 500 ml	30 min	Boiling

The mass of each specimen was measured prior to the corrosion test (W_1), after the corrosion test (W_2), and after the chemical treatment of the corroded specimen (W_3). The corrosion mass gain(ΔW_g) after the corrosion test, can be calculated from the change in mass between W_2 and W_1 per unit area of the sample surface (A). ΔW_g is the sum of the mass gain due to the oxygen in the formed oxide ($W_O^{\text{in oxide}}$), the mass gain due to the chlorine in the formed solid metal chlorides ($W_{Cl}^{\text{in MCl2(s)}}$), and the mass loss due to the metal in the evaporated metal chlorides ($W_M^{\text{in MCl2(g)}}$):

$$\Delta W_g = (W_2 - W_1)/A = W_O^{\text{in oxide}} + W_{Cl}^{\text{in MCl2(s)}} - W_M^{\text{in MCl2(g)}} \tag{8}$$

Where A is the area of sample surface. Then, W_2 can be expressed as:

$$W_2 = W_1 + (W_O^{\text{in oxide}} + W_{Cl}^{\text{in MCl2(s)}} - W_M^{\text{in MCl2(g)}})A \tag{9}$$

The total mass loss (ΔW_l) due to corrosion followed by chemical treatment can be calculated from the change in mass between W_1 and W_3 per unit area of the sample surface (A). ΔW_l is the sum of the mass loss due to the removed metal in the oxide ($W_O^{\text{in oxide}}$), the

mass loss due to the removed metal in the solid metal chlorides ($W_{\text{M}}^{\text{in MCl2(s)}}$), and the mass loss due to the metal in the evaporated metal chlorides ($W_{\text{M}}^{\text{in MCl2(g)}}$):

$$\Delta W_l = (W_3 - W_1)/A = -W_{\text{M}}^{\text{in oxide}} - W_{\text{M}}^{\text{in MCl2(s)}} - W_{\text{M}}^{\text{in MCl2(g)}} \tag{10}$$

Then, W_3 can be expressed as:

$$W_3 = W_1 - (W_{\text{M}}^{\text{in oxide}} + W_{\text{M}}^{\text{in MCl2(s)}} + W_{\text{M}}^{\text{in MCl2(g)}})A \tag{11}$$

From reactions (9) and (11), the mass difference between after the corrosion test and after the chemical treatment can be written as:

$$W_2 - W_3 = (W_{\text{O}}^{\text{in oxide}} + W_{\text{M}}^{\text{in oxide}} + W_{\text{Cl}}^{\text{in MCl2(s)}} + W_{\text{M}}^{\text{in MCl2(s)}})A \tag{12}$$

This equation describes the total mass of oxide and solid metal chloride remaining in the sample.

Assuming that the mass of solid metal chlorides per unit area of the sample surface ($W_{\text{MCl2(s)}}$) formed in the external corrosion scale underwent complete oxidation, $W_{\text{Cl}}^{\text{in MCl2(s)}}$ and $W_{\text{M}}^{\text{in MCl2(s)}}$ can be neglected. Then, using equation (12), we can obtain the total mass of formed oxide per unit area of the sample surface ($W_{\text{MO(s)}}$). $W_{\text{M}}^{\text{in oxide}}$ can be calculated using the empirical formula and $W_{\text{MO(s)}}$. Next, by substituting the value of $W_{\text{M}}^{\text{in oxide}}$ into equation (11), $W_{\text{M}}^{\text{in MCl2(g)}}$ can be obtained.

In this study, we evaluated ΔW_{g}, ΔW_{l}, and $W_{\text{M}}^{\text{in MCl2(g)}}$.

2.4   Analysis Techniques for Surface Morphologies and Cross-Sections

2.4.1   X-ray Diffraction (XRD)

Phase analysis of the corrosion products were performed by X-ray diffraction (XRD; Rigaku SmartLab) in the Bragg-Brentano geometry using Cu Kα1 radiation ($\lambda = 0.15405$ nm) in the range of 20-90° with a step size of 0.02 and 4 s per step. The QualX2 software[56] with the POW_COD database was used to identify the structural phases from XRD patterns.

2.4.2 Focused Ion Beam (FIB) Milling

In order to avoid the loss of metal chlorides that would occur during sample preparation using water, focused ion beam milling (JEOL JIB-4601F) was used to prepare cross-sections of all samples. Prior to milling, C or W was deposited on the sample surface.

2.4.3 Field-Emission Scanning Electron Microscopy-Energy-Dispersive X-Ray Spectroscopy (FESEM-EDS)

The cross-sections obtained after the corrosion tests were examined using field-emission scanning electron microscopy and the distribution of each element was analyzed by energy-dispersive X-ray spectroscopy (FESEM-EDS; JEOL, JSM-7001FA).

CHAPTER 3
EFFECT OF MOLYBDENUM AND IRON COMBINATIONS ON CORROSION BEHAVIOR IN AIR WITH NaCl-KCl-CaCl₂ VAPOR

3.1   Introduction

NiCr-based alloys and coatings are widely used for materials which applied in high temperature application as well as alloy or coating materials due to their high temperature corrosion-oxidation resistance and good mechanical properties. Some of commercial alloys such as 625, HR160, C-276, HC-22, JHN24 and Sanicro 28 are widely used in waste incinerator, and those alloys contain different amount of Fe and Mo [8,28,49,59,60].

In the oxidizing environment with O_2 present, the mechanism of high temperature corrosion of alloys by alkali salt is often explained by "chlorine cycle mechanism" where chlorine is able to penetrate the oxide layer through pores and cracks, and reaches the metal surface leading to a formation of metal chlorides [24,29]. Because the metal chlorides have high vapor pressure the metal chloride become easily evaporated to the atmosphere. Since the partial pressure of oxygen in the atmosphere is usually high, the evaporated metal chlorides oxidize and release chlorine. This active oxidation is very rapid [30,31]. There are some reports that alkali ion has an ability to induce corrosion by breaking down the protectiveness of oxide scale [32–35,57,58].

There are contradictive reports that Fe and Mo addition in NiCr-based alloys is beneficial or detrimental in such aggressive corrosion environments. Thus, the effect of Fe and Mo addition on the corrosion behavior of Ni20Cr-based alloys has not been clearly understood.

Therefore, in this study, the corrosion behavior of Ni-based alloys in air + salt-vapor environment at 570 °C was studied using Ni20Cr alloys with combinations of 1-7 wt. % of Mo, and 4 or 30 wt.% of Fe addition in order to understand the combination effect of Mo and Fe on corrosion of alloys in salt vapor containing atmosphere.

3.2   Results and Discussion

3.2.1   Corrosion Kinetics

Figure 10 shows the corrosion mass gain (ΔW_g) of the Ni20Cr-xMo alloys with different Fe addition as a function of corrosion time at 570 °C. The corrosion mass gain of all alloys with different Mo content tended to decrease with Fe addition and further decreased with increasing Fe content, which indicates that Fe addition into the Ni20Cr-Mo based alloy can improve the corrosion resistance.
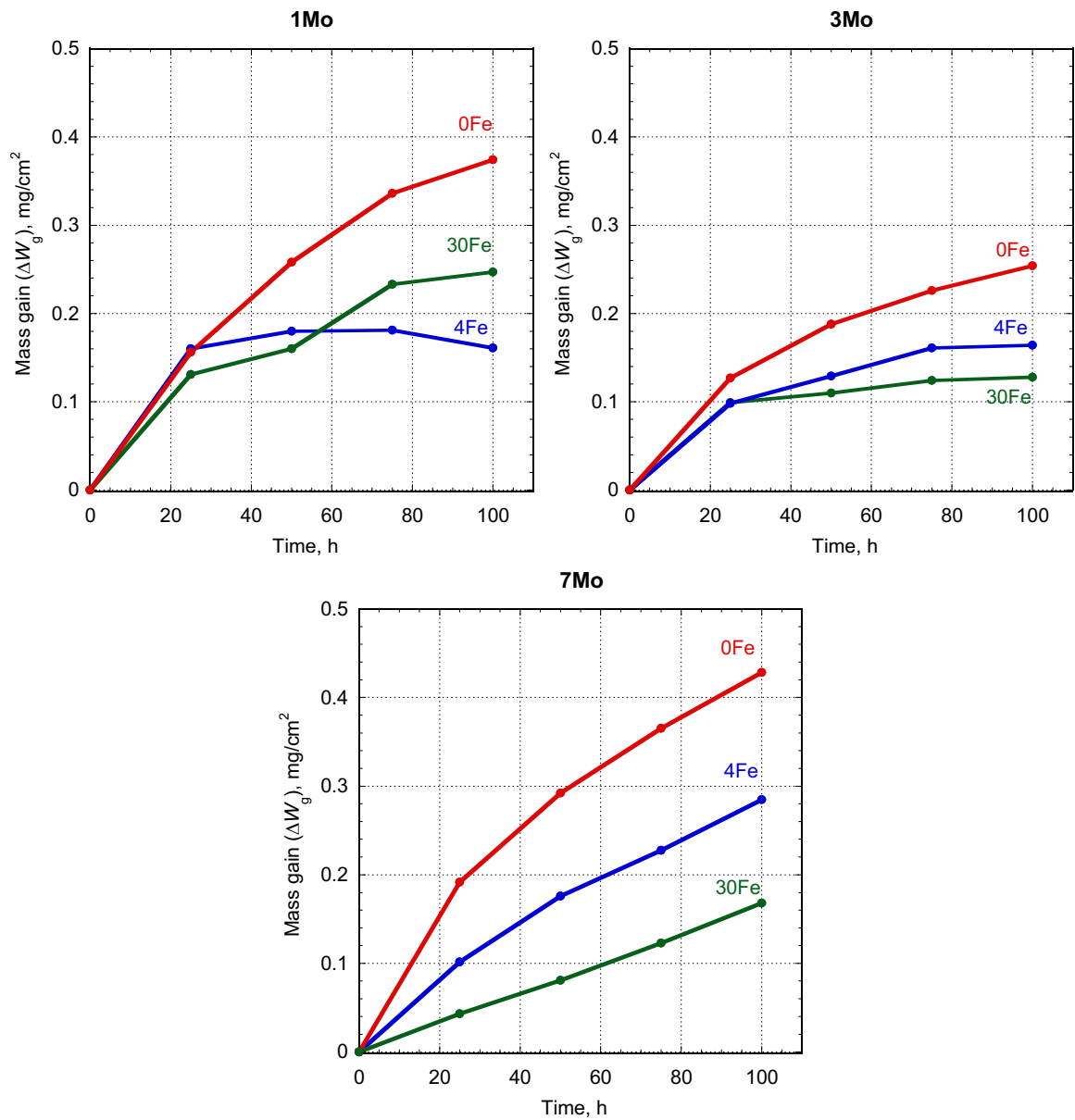
Fig. 10 Corrosion mass gain (ΔW_g) for the Ni20Cr-xMo alloys with different Fe addition as a function of corrosion time at 570°C in the oxidizing-chlorine containing atmosphere.
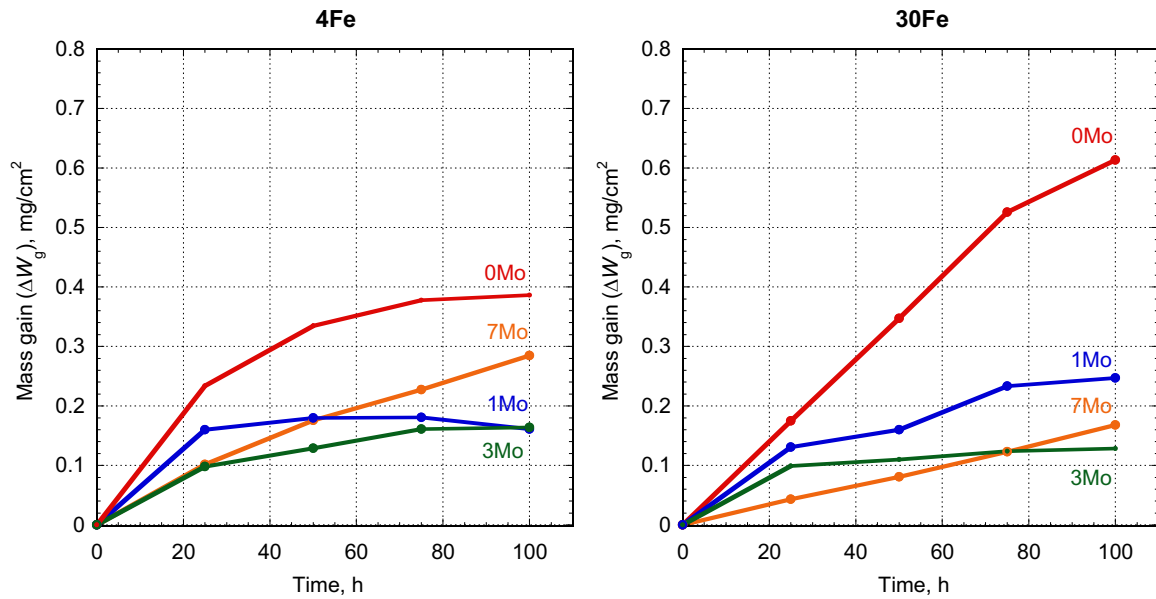
Fig. 11 Corrosion mass gain (ΔW_g) for the Ni20Cr-yFe alloys with different Mo addition as a function of corrosion time at 570°C in the oxidizing-chlorine containing atmosphere.

The corrosion mass gain of alloys with 3 wt.% of Mo was smaller than those of alloys with 1 wt.% Mo. However, further Mo addition to 7 wt.% Mo tended to increase the corrosion mass gain. This tendency was clearer for the alloys with low Fe content, suggesting that the effect of Mo on the corrosion mass gain depended on the Fe content.

The Mo effect on corrosion can be more clearly seen in Fig. 11. Mo addition into the alloy containing Fe led to improve the corrosion resistance of the alloys. The most optimum of combination with Mo addition for both alloys containing Fe content was 3 wt.% Mo. More or less Mo addition into the alloys containing Fe content increased the corrosion mass gain. 4Fe-1Mo alloy showed the corrosion mass loss, suggesting that the spallation of the corrosion products or evaporation of metal chlorides.

Only the corrosion mass gain profile of the alloy containing 30 wt.% of Fe and 7 wt.% of Mo displayed a linear-like behavior, whereas mass gain profiles of all the other alloys displayed parabolic-like behavior.

The mass loss kinetics (ΔW_l) for the Ni20Cr-xMoyFe alloys was shown in the Fig. 12. The profiles displayed the similar trend with the profiles of corrosion mass gain (Fig. 10), Fe-free Ni20Cr-xMo alloys have corrosion mass loss higher than the alloys with Fe addition. The corrosion mass loss decreased with increasing Fe content in the Ni20Cr-xMo

alloys. The lowest corrosion mass loss was attained on the alloy containing 30 wt.% of Fe and 3 wt.% of Mo.
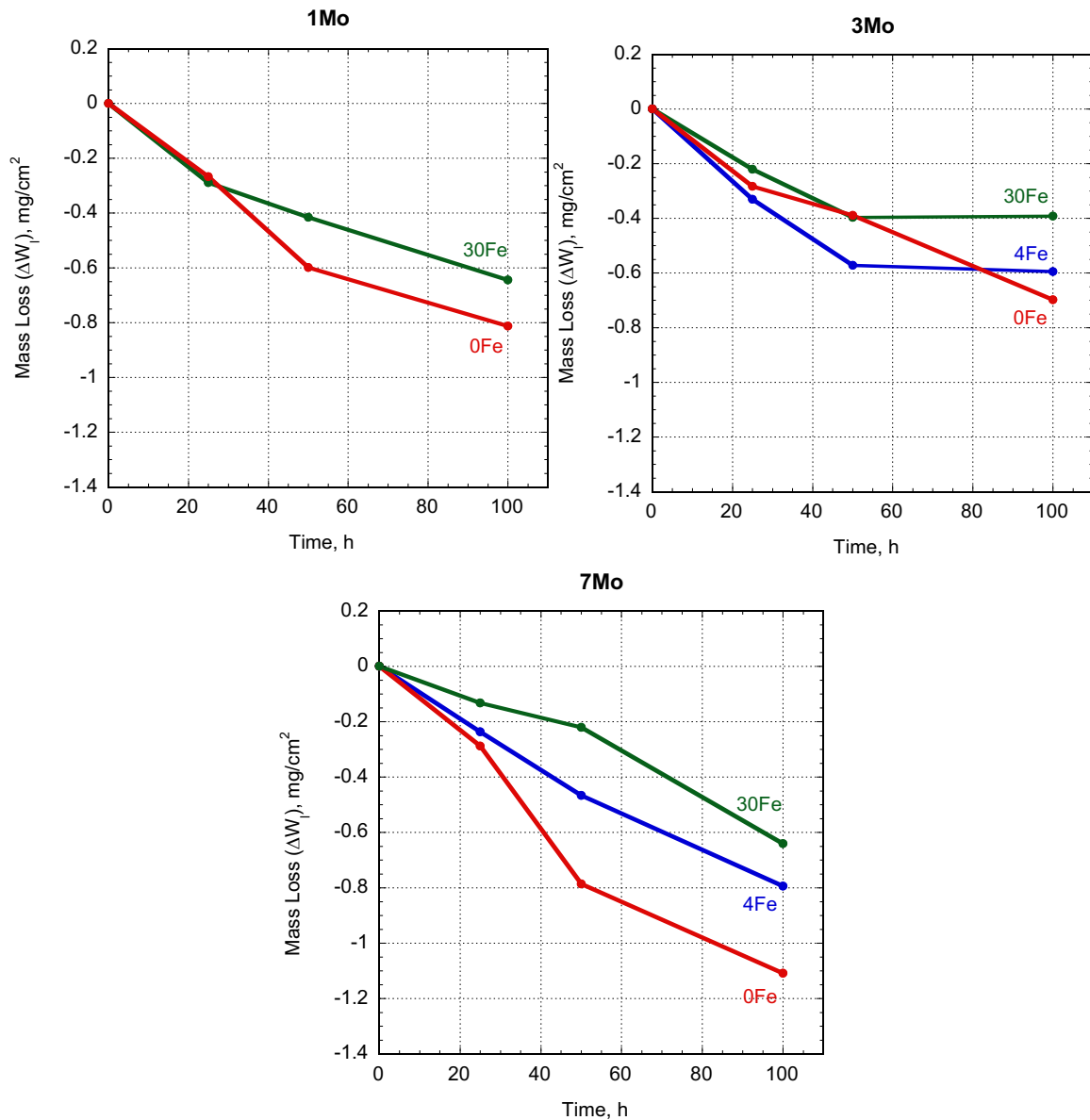
Fig. 12 Mass loss (ΔW_l) for the Ni20Cr-xMoyFe alloys as a function of corrosion time at 570°C in the oxidizing-chlorine containing atmosphere.

Figure 13 displayed the profiles of calculated metal loss due to evaporation of metal chlorides ($W_M^{in\ MCl2(g)}$) for the Ni20Cr-xMoyFe alloys after corrosion test. The evaporation of metal chlorides increased with corrosion time. The evaporation of metal chlorides of all the Ni20Cr-xMo alloys without Fe addition tended to increase with higher Mo contents. This indicate that higher Mo addition in the Ni20Cr-based alloys is not beneficial due to

increasing the evaporation of metal chlorides during the corrosion test. However, Fe addition to a Mo containing Ni20Cr alloys decreased the evaporation of metal chlorides. Higher Fe content in the alloy further decreased the evaporation metal chlorides.

Fig. 13 Calculated metal loss due to evaporation of metal chlorides ($W_M^{in\ MCl2(g)}$) for the Ni20Cr-xMoyFe alloys during the corrosion tests at 570°C in the oxidizing-chlorine containing atmosphere.

Based on the overall kinetic corrosion profiles, Mo and Fe additions were found to give better corrosion resistance to the Ni20Cr-based alloys. However, there are optimal Fe and Mo contents, which is 30 wt.% of Fe and 3 wt.% Mo to minimize the corrosion mass gain as well as evaporation of metal chlorides.

3.2.2 Surface Morphology of Corroded Samples

Figures 14 and 15 represent the surface morphologies and elemental distribution maps of the corroded samples after a corrosion test for 100 h in the oxidizing-chlorine containing atmosphere. Although some bumps were observed on the sample surface, the surfaces of the all the alloys after corrosion test were very smooth, as shown in the Fig. 14, indicating that all the sample surfaces were covered by the oxide scale. These results have been confirmed by the EDS mapping of Ni20Cr-7Mo30Fe as shown in the Fig. 15. Some studies reported that the corrosion in the chlorine containing atmosphere with alkali metal deposits led to a formation of chromates on the sample surface [32–35,57,58]. However, no K, Na, Ca and Cl signals were detected from the surface of all the samples with Mo and Fe additions based on the EDS mapping results, which indicates that chromate was not formed on the sample surface of all the Fe and Mo containing alloys.
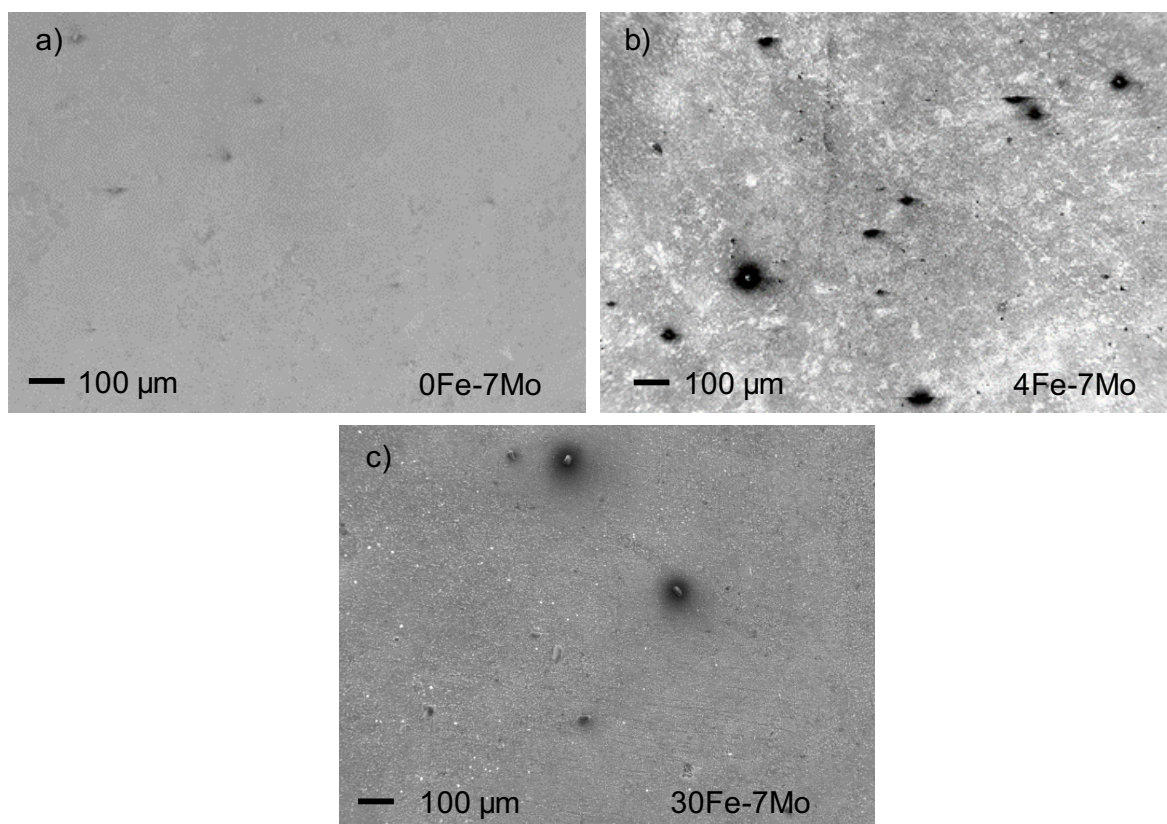
Fig. 14 Surface morphologies of the corroded samples after corrosion test for 100h in the oxidizing-chlorine containing atmosphere: (a) 0Fe-7Mo; (b) 4Fe-7Mo; and (c) 30Fe-7Mo.
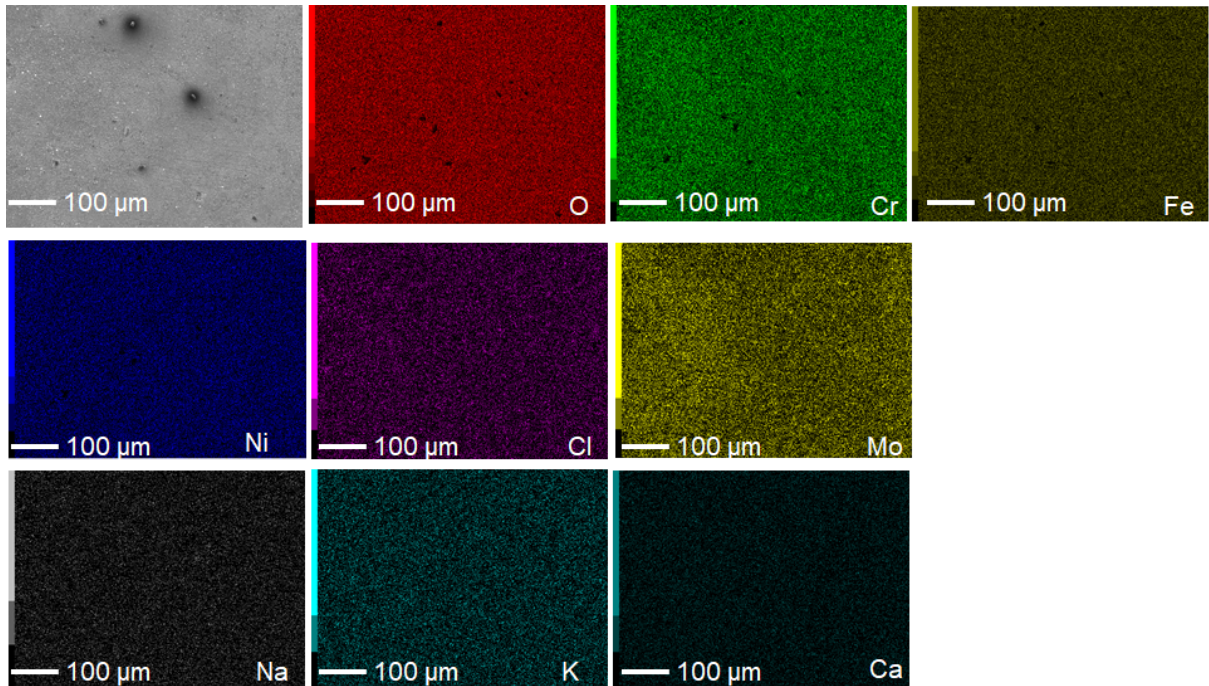
Fig. 15 Surface elemental distribution maps of corroded sample with 30-7Mo alloy after 100 h of corrosion in the oxidizing-chlorine containing atmosphere.

3.2.3   Cross-Sectional Observation of Corroded Samples

Cross-sections of the Ni20Cr-7MoyFe alloys after corrosion test were shown in the Fig. 16. All alloys formed a duplex oxide scale consisted of the outer dense and the inner very porous oxide layer. The thickness of oxide scales became thinner with increasing Fe content in the alloy. The outer oxide scale became thinner but rough with increasing Fe content. Some cracks were also observed in the middle part of the outer oxide scale formed on the Fe containing alloys.

From the EDS mapping of the cross-sections of Ni20Cr-7Mo with 4 and 30 wt.% of Fe alloys in the Figs. 17-18, the outer scale was consisted of Fe-Ni oxide scale. The Fe signal from the outer oxide layer formed on the alloy with 30Fe was stronger comparing to that on the alloy with 4Fe, suggesting that the Fe addition to the alloy changed the composition of the outer oxide layer from Ni-rich to Fe-rich, which might affect the corrosion performance of alloy. The porous inner oxide scale was mainly composed of Cr, Mo, O and Cl, suggesting the formation of not only oxides but also oxychlorides. Although it is difficult to observe clearly due to resolution of the image is not sufficient, at the interface between the outer and

40

inner scales, a thin continuous Cr_2O_3 scale was confirmed to form on 30Fe-7Mo alloy. Although the internal oxidation was frequently observed in the previous studies [28,47,49,61], no internal oxidation nor Cr-depletion zone was observed below the oxide scale. K and Na signals were detected on the surface of oxide scale, which is due the overlapping of characteristic X-ray signal. Thus, no alkali salt nor chromate were considered to be present on the oxide scale.
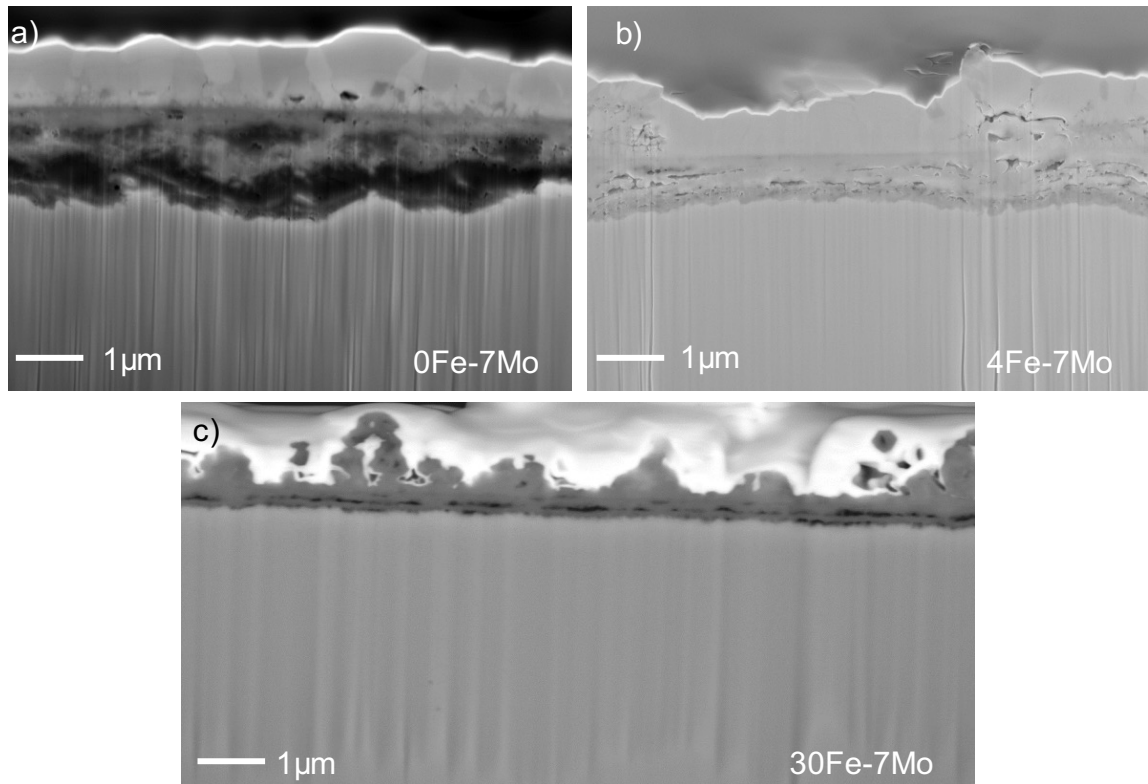
Fig. 16 Cross-sections of the Ni20Cr-xMoyFe alloys after corrosion test for 100 h in the oxidizing-chlorine containing atmosphere: a) 0Mo-7Mo; b) 4Fe-7Mo; and c) 30Fe-7Mo

Because the thickness of both the inner and the outer layers decreased (Fig. 16), it is reasonable to consider that improved corrosion performance by Fe addition is strongly related with the inner oxide layer, i.e., the protectiveness of the inner layer increased by addition of Fe. However, the inner layer was composed of mainly Cr, Mo, O, and Cl. Fe was not confirmed, thus, Fe addition was not directly affected to the protectiveness of the inner layer. Because the Fe-rich outer oxide layer was formed on the alloy with higher Fe content, this Fe-rich oxide scale might reduce the penetration of chlorine into the alloy surface, preventing the porous thick inner oxide layer formation.

Fig. 17 Cross‑sectional elemental distribution maps of the 4Fe-7Mo alloy after 100 h of corrosion in the oxidizing-chlorine containing atmosphere.
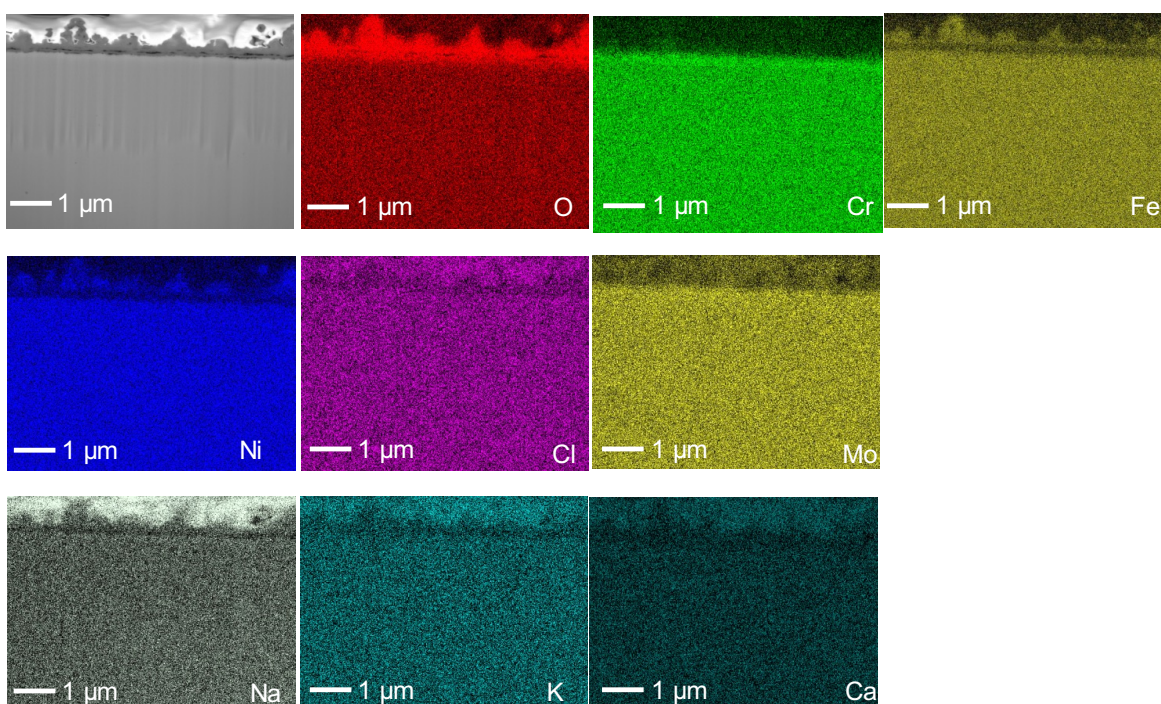
Fig. 18 Cross‑sectional elemental distribution maps of the 30Fe-7Mo alloy after 100 h of corrosion in the oxidizing-chlorine containing atmosphere.

However, further discussion of the effect of Fe and Mo on the corrosion behavior of alloys is not possible based on the result obtained in this chapter, since both elements were

considered to affect the corrosion behavior individually. Thus, following chapters, the effect of single addition of Fe or Mo on the corrosion behavior of Ni20Cr based alloys were conducted in order to understand the effects of each element, Mo or Fe into the Ni20Cr-based alloys on the corrosion behavior in the oxidizing-chlorine containing atmosphere.

3.3   Conclusion

The corrosion behavior of Ni20Cr alloys containing combinations of various Mo contents (1, 3, and 7 wt.%) and Fe contents (4 and 30 wt.%) was investigated at 570 °C in an air + NaCl-KCl-CaCl$_2$ salt vapor mixture. The obtained results can be summarized as follows:

1. Mo and Fe addition to the Ni20Cr-based alloys improved the corrosion resistance. The corrosion performance was found to be improved with increased both Mo and Fe contents. The optimum contents of Mo and Fe for good corrosion performance was found to be 3 wt. % of Mo and 30 wt.% of Fe.

2. The evaporation of metal chlorides during corrosion decreased with increasing Fe content and Mo content up to 3 wt.%. Further Mo addition at 7 wt.% increased the evaporation of chlorides.

3. The alloys formed an outer Ni-Fe oxide scale and an inner porous oxide scale. The outer oxide scale changed from Ni-rich to Fe-rich oxide scale with increased Fe content. The inner layer consisted of mainly Cr-Mo oxide and oxychlorides.

4. A thick porous inner oxide formation on the alloy with higher Mo and lower Fe contents might increase the corrosion rate. The porous inner oxide layer was considered to be formed due to the penetration of chlorine. Fe addition was inferred to decrease the penetration of chlorine into the alloy substrate by Fe-rich oxide scale formation.

CHAPTER 4
EFFECT OF MOLYBDENUM ON CORROSION BEHAVIOR IN AIR
WITH NaCl-KCl-CaCl₂ VAPOR

4.1   Introduction

Mo alloying in high temperature corrosion-resistant alloys and coatings is widely accepted to enhance the corrosion resistance [62,63]. Numerous reports have studies Mo alloying in chlorine atmosphere with high oxygen or low oxygen content [27,28,36,52–54,64], but the results were contradictive each other and the corrosion mechanism has not yet well understood. In the previous chapter, it was found that both Fe and Mo addition is beneficial for improving the corrosion performance of Ni20Cr-based alloys. However, the effect of each element on corrosion could not be assessed.

Therefore, in this study, the corrosion behavior of Ni-based alloys in air + salt-vapor environment at 570 °C was systematically studied using Ni20Cr alloys with/without 1~7Mo (in wt. %) in order to understand the effect of Mo on corrosion of alloys in salt vapor containing atmosphere.

4.2   Results

4.2.1   Corrosion Kinetics

Figure 19 shows the corrosion kinetics of the alloys during the corrosion tests in the oxidizing-chlorine containing atmosphere. The corrosion mass gain (ΔW_g) of the Mo-free alloy was higher than that of all of the Mo-containing alloys, indicating that Mo addition improved the corrosion resistance of the Ni20Cr alloys. The alloy containing 3 wt.% Mo exhibited the lowest corrosion mass gain, while further increasing the Mo content to 7 wt.% led to greater corrosion. The corrosion mass gain profiles of all of the alloys displayed parabolic-like behavior. As shown in Fig. 19b, the mass loss (ΔW_l) profiles exhibited a similar trend, indicating that the chemical treatment procedure was compatible with the corrosion test. The mass loss was considerably higher for the Mo-free alloy than for the Mo-containing alloys, and the alloy with 3 wt. % Mo displayed the lowest mass loss.
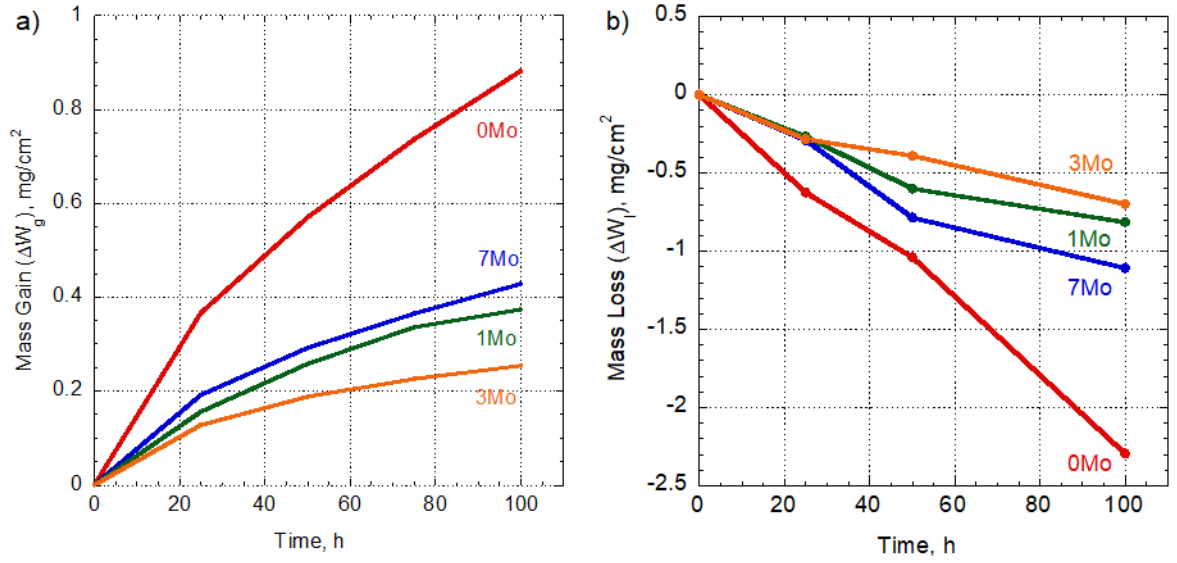
Fig. 19 (a) Corrosion mass gain (ΔW_g), and (b) mass loss analysis (ΔW_l) of the Ni20Cr-xMo alloys at 570°C as function of the corrosion time in the oxidizing-chlorine containing atmosphere.
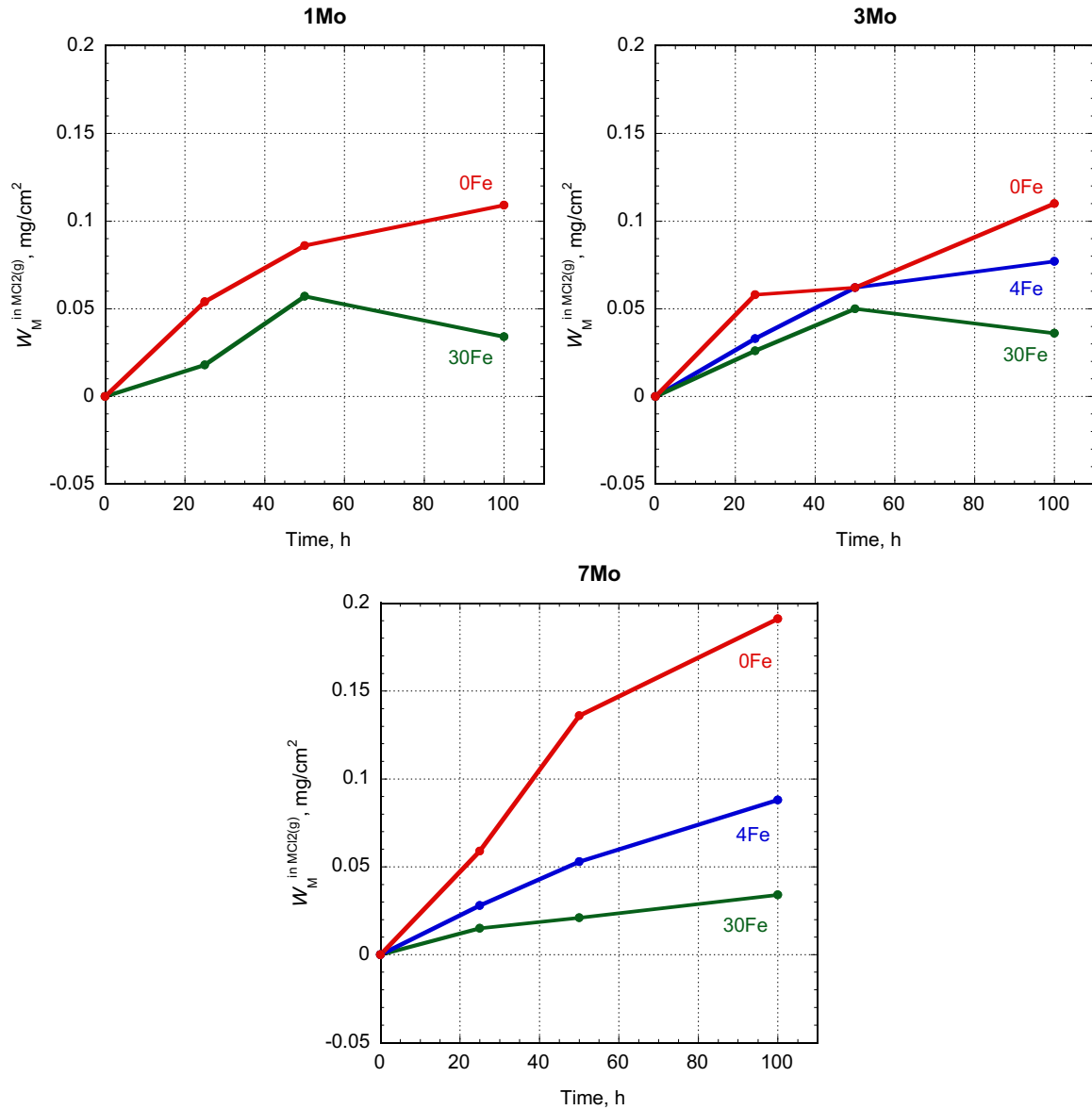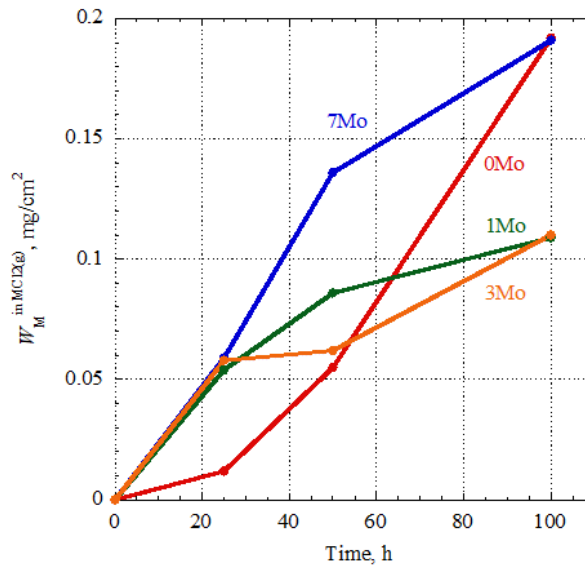

Fig. 20 Calculated metal mass loss due to evaporation of metal chlorides ($W_M^{\text{in MCl2(g)}}$) for the Ni20Cr-xMo alloys during the corrosion tests at 570°C for 100 h in the oxidizing-chlorine containing atmosphere.

The calculated metal mass loss due to evaporation of the metal chlorides ($W_M^{\text{in MCl2(g)}}$) is shown in Fig. 20. From the beginning of the corrosion test until 50 h, the evaporation of metal chlorides was considerably lower for the Mo-free alloy than for the Mo-containing alloys. However, by the next time point at 100 h, the evaporation of metal chlorides was remarkably lower for the alloys containing 1 and 3 wt.% Mo compared with

the Mo-free alloy and the alloy containing 7 wt.% Mo This indicated that the addition of up to 3 wt.% Mo decreased the evaporation of metal chlorides during the corrosion, whereas further Mo addition led to greater molybdenum chloride evaporation. Although the evaporation of metal chlorides was observed, the mass of evaporated material was much lower compared with the mass gain and mass loss. Thus, the corrosion performance of the alloys can be evaluated from the corrosion mass gain or the mass loss upon removal of the corrosion products.
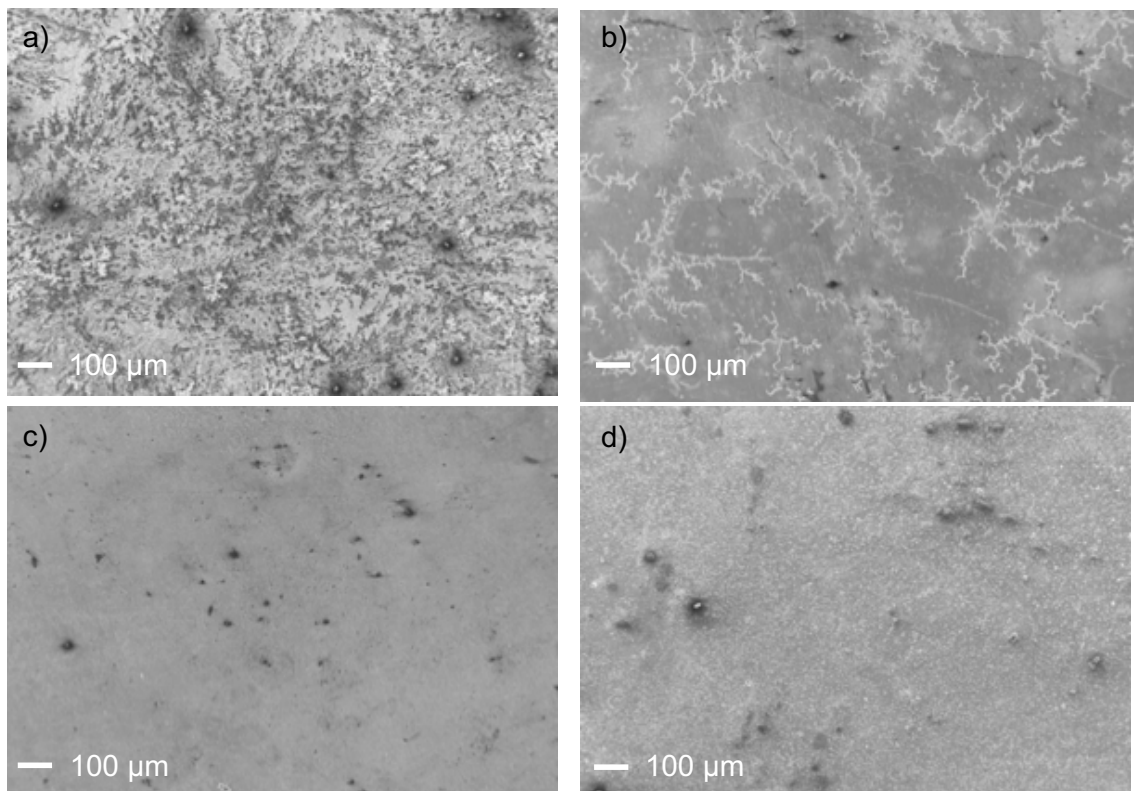
Fig. 21 Surface morphologies of the corroded samples after 100h of corrosion in the oxidizing-chlorine containing atmosphere.: a) Mo-free, (b) 1Mo, (c) 3Mo, and (d) 7Mo

4.2.2 Surface Morphology of Corroded Samples

The surface morphologies and elemental distributions of the corroded specimens after 100h of corrosion in the oxidizing-chlorine containing atmosphere were analyzed by using FESEM-EDS. The results are shown in the Figs. 21-23. The surfaces of all specimens were covered by oxide scale. Dendritic-structured products were observed on both the Mo-free and the alloy containing 1 wt.% Mo, and the area of these dendritic products was smaller in

the 1Mo alloy. In contrast, the surfaces of the alloys containing 3 and 7 wt.% Mo were very smooth, although some bumps were observed on the surface of the latter sample. Figures 22 and 23 present EDS mapping for the Mo-free alloy and alloy containing 3 wt.% Mo, respectively. The result revealed that the dendritic products were predominantly composed of NaCl and the gray areas and dark areas in the FESEM images corresponded to Ni-rich oxides and mixtures of Cr and K, respectively. Only low signal of Ca was detected on the alloy surfaces. The 3Mo alloy was covered by Cr and Ni oxides, and no sodium or potassium chlorides were detected from EDS analysis (Fig. 23).
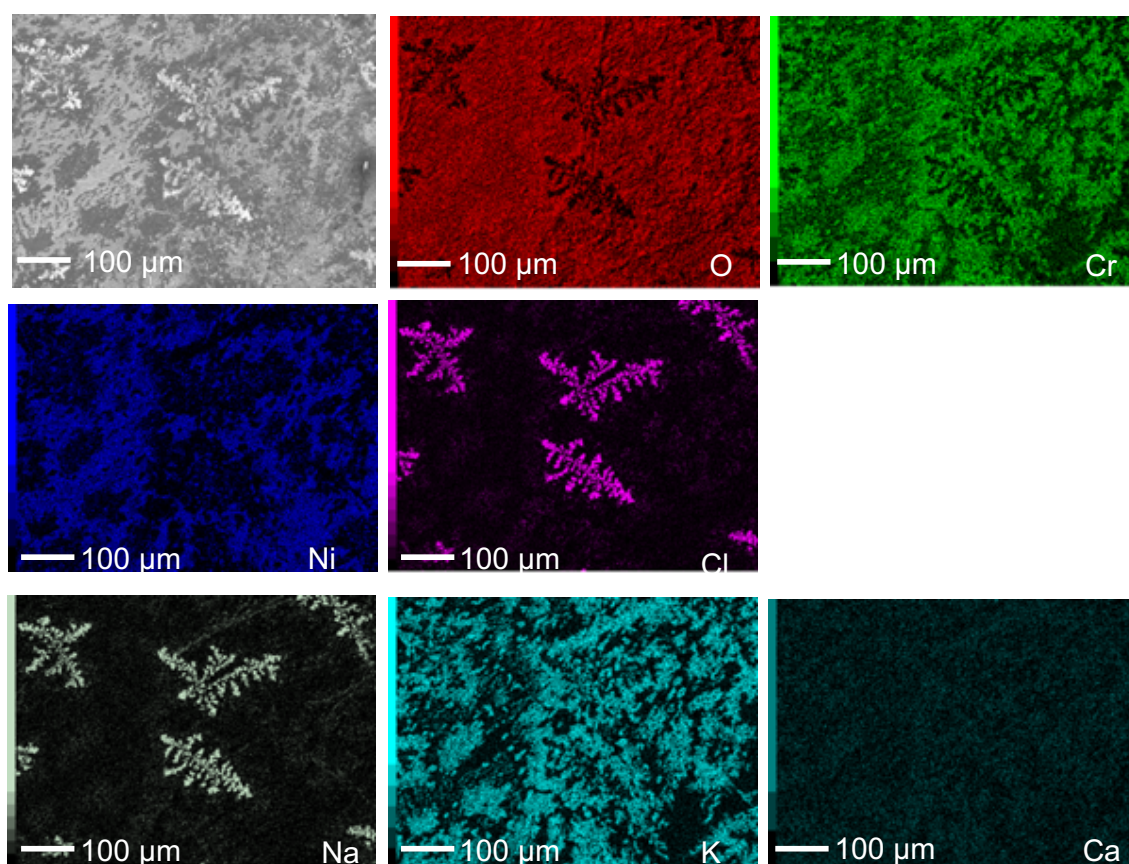
Fig. 22 Elemental distribution maps of the surface of the Mo-free alloy after 100 h of corrosion in the oxidizing-chlorine containing atmosphere.
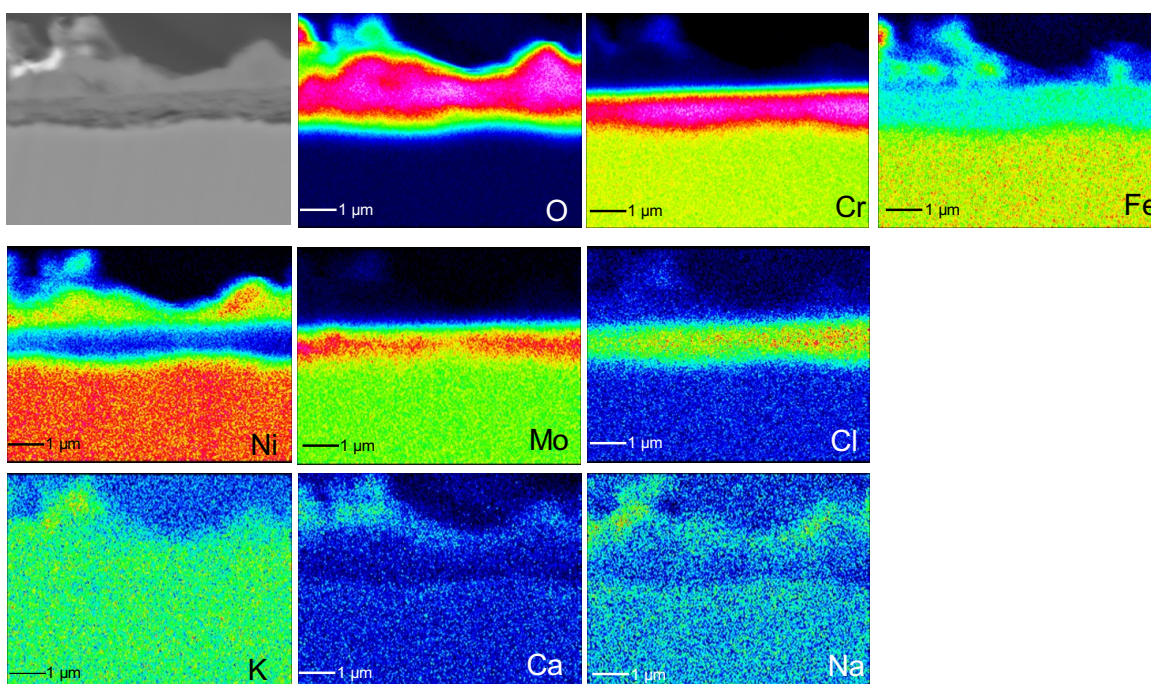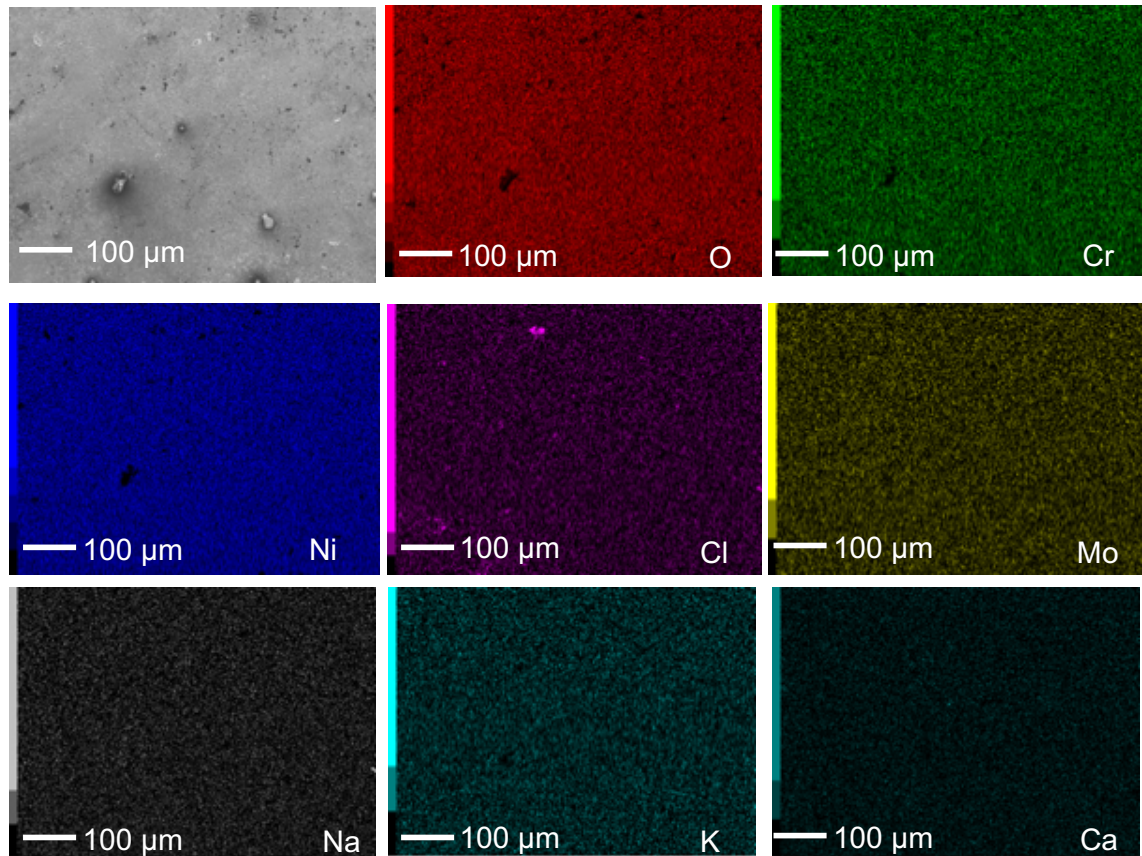
Fig. 23 Elemental distribution maps of the surface of 3Mo alloy after 100 h of corrosion in the oxidizing-chlorine containing atmosphere.

4.2.3 Cross-Sectional Observation of Corroded Samples

Figure 24 shows the cross-sections of the specimens after 100h of corrosion in the oxidizing-chlorine containing atmosphere. Comparison of the results revealed that the thickness of the oxide scale decreased in the following order: 0Mo, 1Mo, 7Mo and 3Mo. This is in accordance with the corrosion kinetics. The thick oxide scale formed on the Mo-free alloy was found to be rich in Cr and also contained Ni, and an internal precipitation zone, which consisted of subsurface Cr oxide penetration and internal Cr-chloride precipitates, had developed below the oxide scale as shown in Fig. 25. Beneath the internal precipitation zone, a thick and well-developed Cr-depleted zone was also observed. Above the outer NiCr oxide scale, potassium chromate formation was also confirmed.
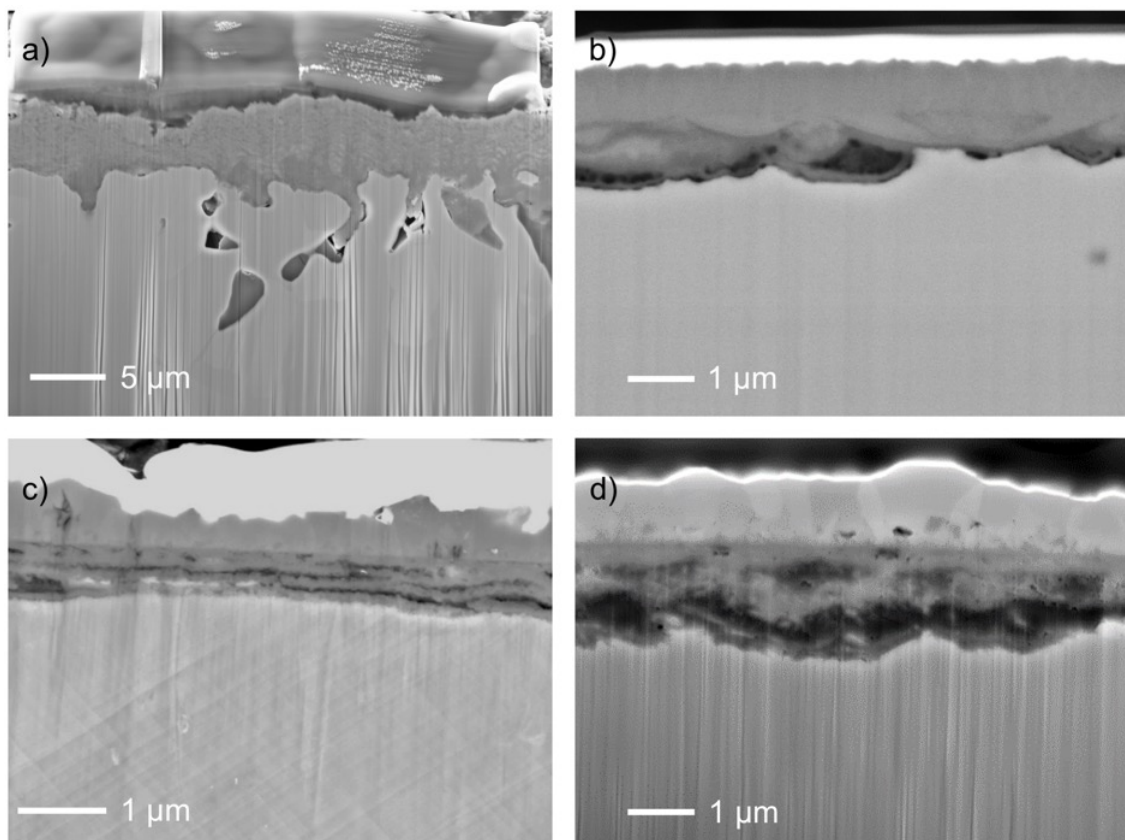
Fig. 24 Cross-sections of the alloy samples after 100 h of corrosion in the oxidizing-chlorine containing atmosphere: (a) Mo-free, (b) 1Mo, (c) 3Mo, and (d) 7Mo.
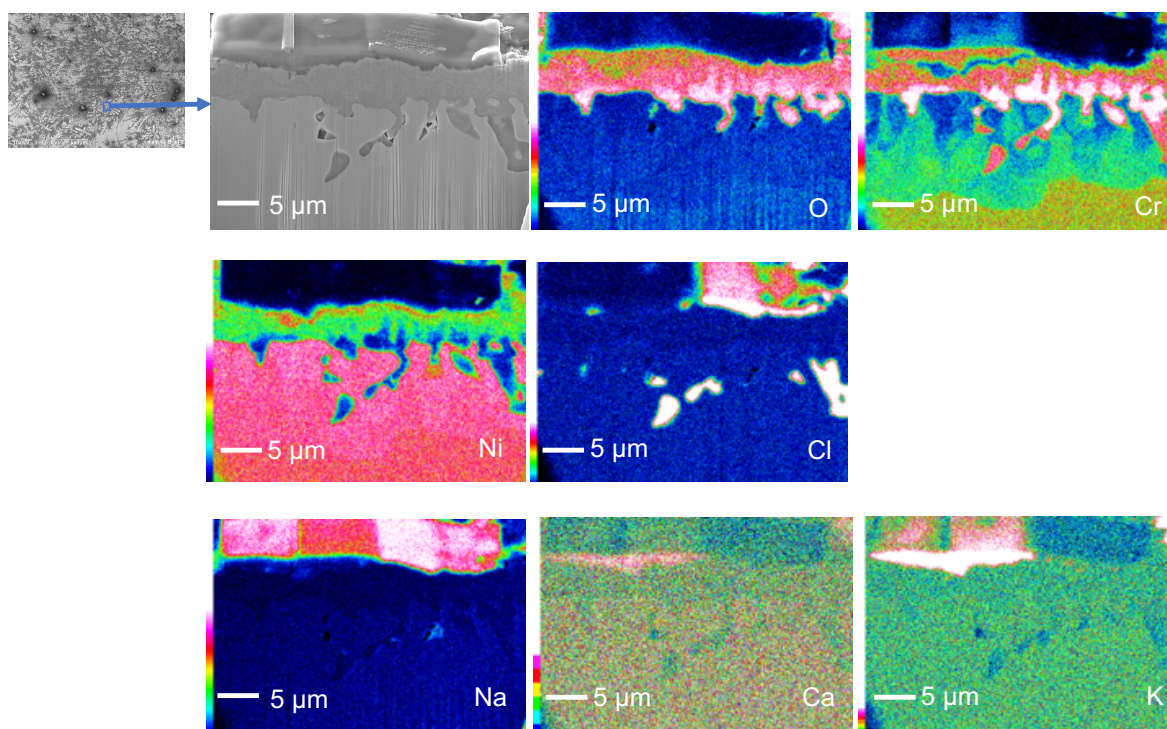
Fig. 25 Cross-sectional elemental distribution maps of the Mo-free alloy after 100 h of corrosion in the oxidizing-chlorine containing atmosphere.

49

The corroded scale of the alloy containing 1 wt.% Mo consisted of a duplex structure, with continuous NiO as an outer oxide scale, and below this NiO, an inner oxide scale was formed locally. Large pores were observed within the inner oxide scale. Neither internal oxidation nor chlorination was observed for this alloy. High signals on the Na mapping image was due to the overlapping X-ray signals with W.

The scales formed on the alloys containing 3 and 7 wt.% Mo had a similar structure, which consisted of a duplex layer composed of an outer NiO scale and an inner Cr-rich oxide layer (Figs. 26 and 27). Mo and Cl were detected in the inner layer along with the Cr-oxide. This inner layer was very porous. A lot of gaps were observed within the layer. As expected from the surface images shown in Figs. 26 and 27, potassium-chromate formation was not confirmed for these alloys, which may suggest that Mo addition promoted NiO formation, thereby preventing contact between the KCl and Cr_2O_3 scale. Nether internal Cr-chloride precipitates nor a Cr-depleted zone was observed in the Mo-containing alloys, suggesting that the presence of Mo suppressed the penetration of chlorine.
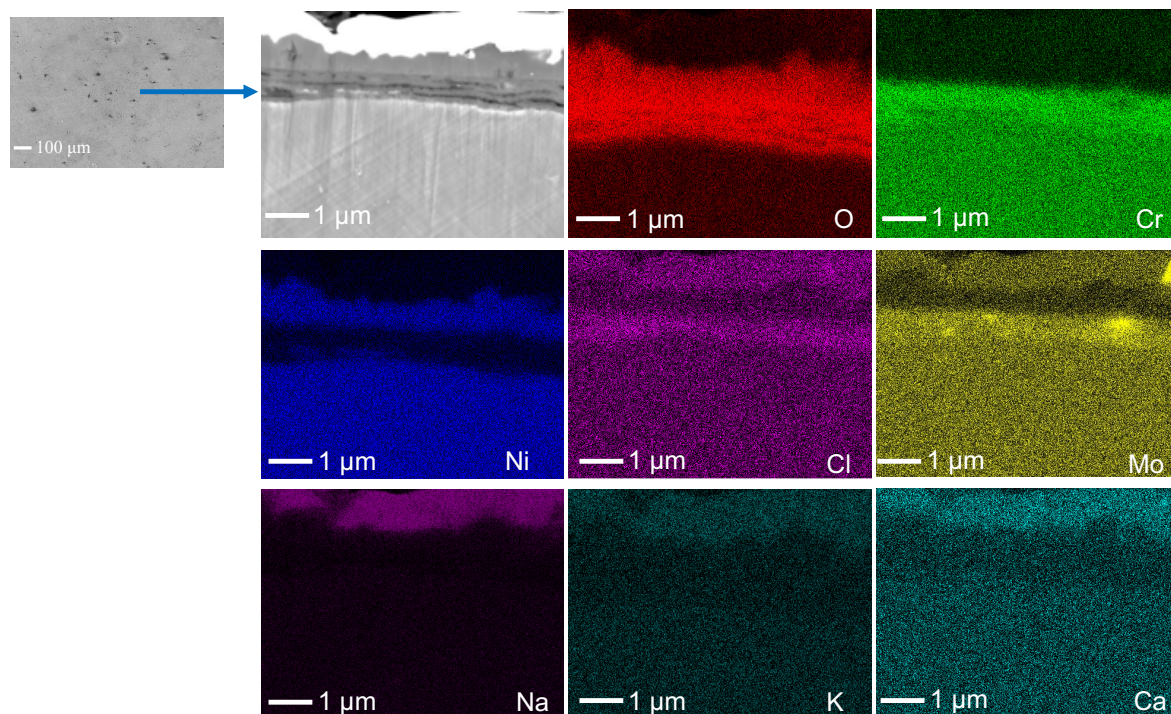
Fig. 26 Cross-sectional elemental distribution maps of the 3Mo alloy after 100 h of corrosion in the oxidizing-chlorine containing atmosphere.
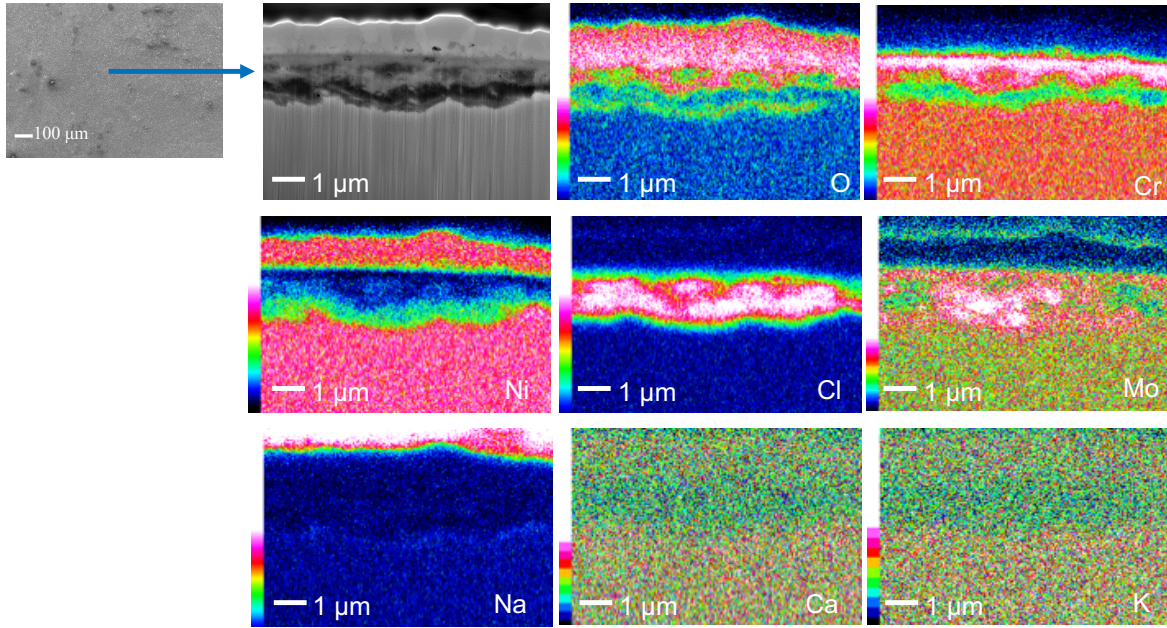
Fig. 27 Cross-sectional elemental distribution maps of the 7Mo alloy after 100 h of corrosion in the oxidizing-chlorine containing atmosphere.

4.3   Discussion

Based on the overall results presented above, the Mo-containing Ni20Cr alloys exhibited better corrosion resistance in the air + salt vapor atmosphere than that of the binary Ni20Cr alloy. This proves that the Mo addition is beneficial for improving the corrosion performance of Ni20Cr-based alloys in oxidizing chlorine-containing atmospheres.

Many studies of high temperature corrosion in oxidizing chlorine-containing atmospheres have been conducted [28,31,34,53,55,58]. However, the samples used in previous studies were typically corroded via salt deposition or under atmospheres composed of air/O_2 mixed with Cl_2/HCl. In contrast, in this study, the chlorine was supplied from a salt mixture as gas vapor with air. Consequently, the results of this study may not be comparable with those of previous studies. Some studies involving oxidizing chlorine-containing atmospheres have reported that Mo alloying can enhance the corrosion resistance of the alloys in an atmosphere composed of O_2 and HCl gas with and without KCl deposits [55,58]. However, other studies have reported that Mo alloying led to accelerated corrosion in chlorine-containing air/O_2 atmospheres [28,53].
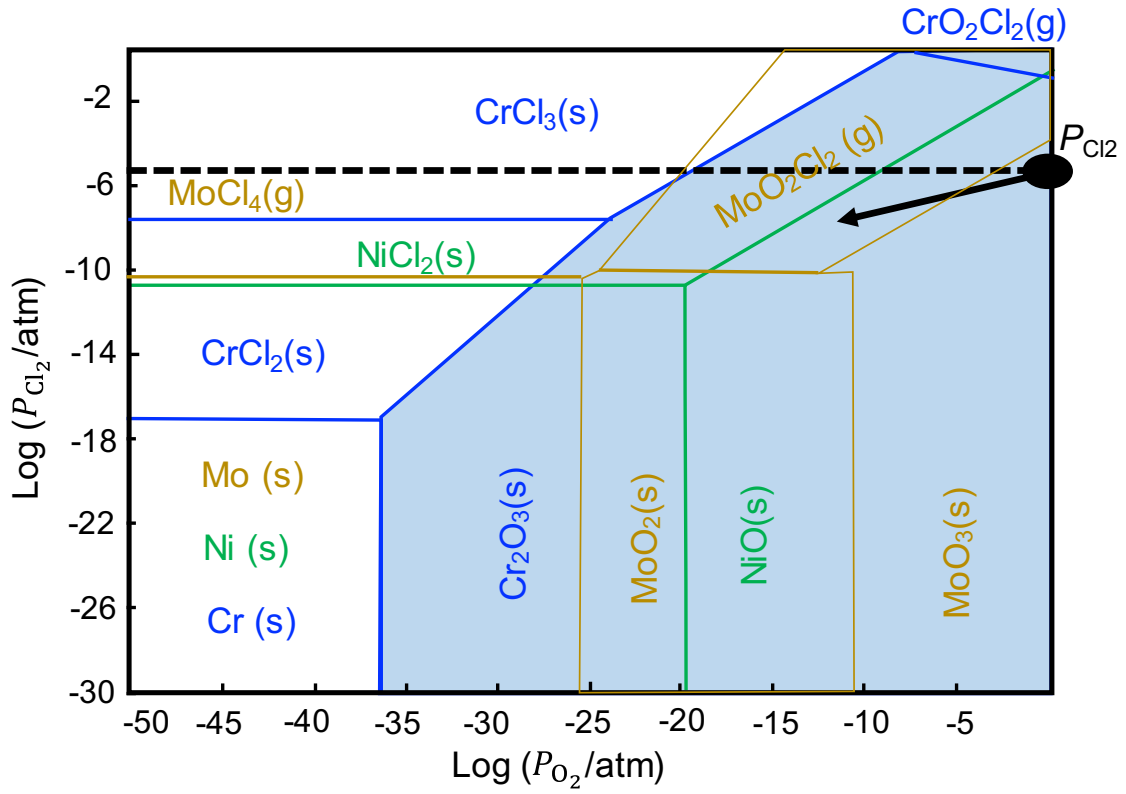
Fig. 28 "Quasi"-stability diagram for the Ni20Cr-7Mo-O-Cl system at 570ºC with a_{Ni}= 0.5615, a_{Cr}= 0.1332, a_{Mo}=0.0237, in the oxidizing-chlorine containing atmosphere (P_{O_2} = 0.2 atm, P_{Cl_2} = 3.7 × 10^{-6} atm, and $P_{MCl_2(g)}$ = 9.87 × 10^{-5} atm).

The chlorine potential (P_{Cl_2}) used in the present study was calculated to be 3.7 × 10^{-6} atm by using the FactSage software [65]. Figure 28 presents a "quasi"-stability diagram for oxides and chlorides on Ni20Cr alloys with and without Mo. In this diagram, the regions of the gas phases of the metal chlorides and oxychlorides were calculated using a gas potential of more than 9.87 × 10^{-5} atm, which was reported to be the critical pressure to affect the corrosion behavior [27]. Thus, the horizontal and diagonal lines on the diagram are not intended to separate the thermodynamically stable areas between the corrosion/oxidation products and metals-in other words, the volatile species are still formed as corrosion products, which does not affect the corrosion rate. Based on the calculations and the "quasi"-stability diagram, the chlorine potential in the atmosphere used in this study was not sufficient for the chlorination of metals; therefore, oxides should be formed initially.
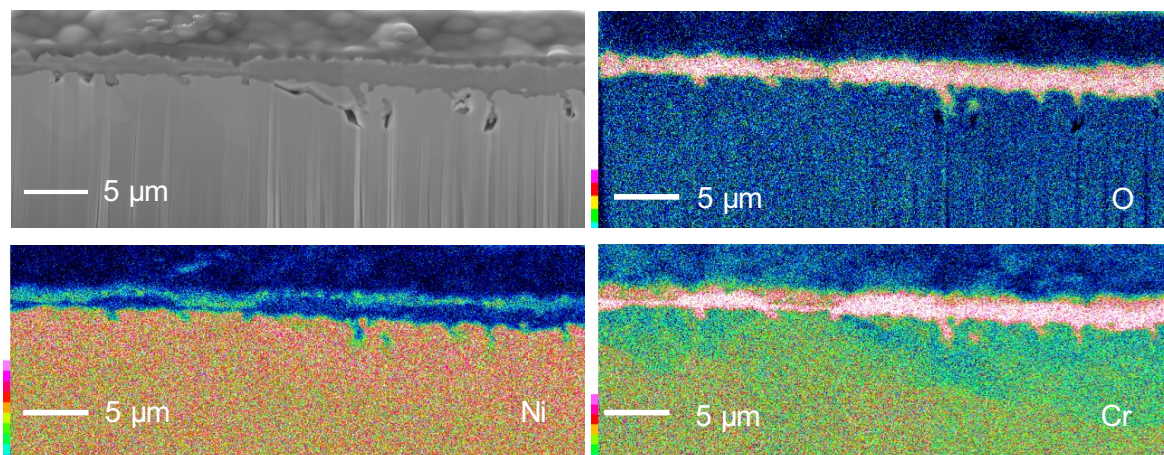
Fig. 29 Cross-sectional elemental distribution maps of the Mo-free alloy after 100h of oxidation at 570°C in air.

The cross-sectional elemental distribution maps of a sample of Ni20Cr alloy oxidized for 100 h in air at 570°C are presented in Fig. 29. An external Cr_2O_3 scale accompanied by some inward growing Cr_2O_3 protrusions formed on this alloy during oxidation, and the structure of this oxide scale was very similar to the corrosion scales formed in the chlorine-containing atmosphere. Thus, during the corrosion of the binary Ni20Cr alloy, a protective Cr_2O_3 scale is expected to form in the initial oxidation period. After the corrosion test, dendritic deposits of NaCl were observed on the sample surface, whereas KCl and $CaCl_2$ were not detected as shown in Fig. 22. The K signal was detected along with the Cr signal, indicating that KCl formed a chromate according to the reaction (13). The formation of potassium-chromate was confirmed by Fig. 25 and the XRD patterns shown in Fig. 30. This reaction also produces chlorine, thereby increasing the local chlorine potential at the surface of the Cr_2O_3 scale. Moreover, chromate formation has been reported to induce the breakdown of a protective chromium oxide [35,57]. Although, chromate formation via a solid–solid reaction is not thermodynamically feasible [58], it is expected to be possible with salt vapor.

Based on formulas (13) and (14), sodium-chromate formation is also thermodynamically feasible. However, this product was not detected in the present study, which may be attributable to the lower vapor pressure of NaCl compared with KCl [66].

$$4KCl(g) + Cr_2O_3(s) + 5/2O_2(g) \rightarrow 2K_2CrO_4(s) + 2Cl_2(g);$$
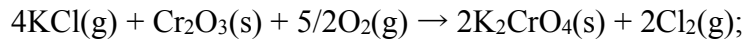
$$\Delta G \ (13) = -71.771 \ kJmol^{-1} \ (at \ 570°C) \tag{13}$$

$$4NaCl(g) + Cr_2O_3(s) + 5/2O_2(g) \rightarrow 2Na_2CrO_4(s) + 2Cl_2(g);$$
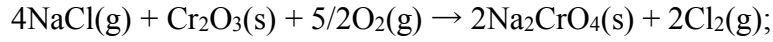
$$\Delta G \ (14) = -70.193 \ kJmol^{-1} \ (at \ 570°C) \tag{14}$$
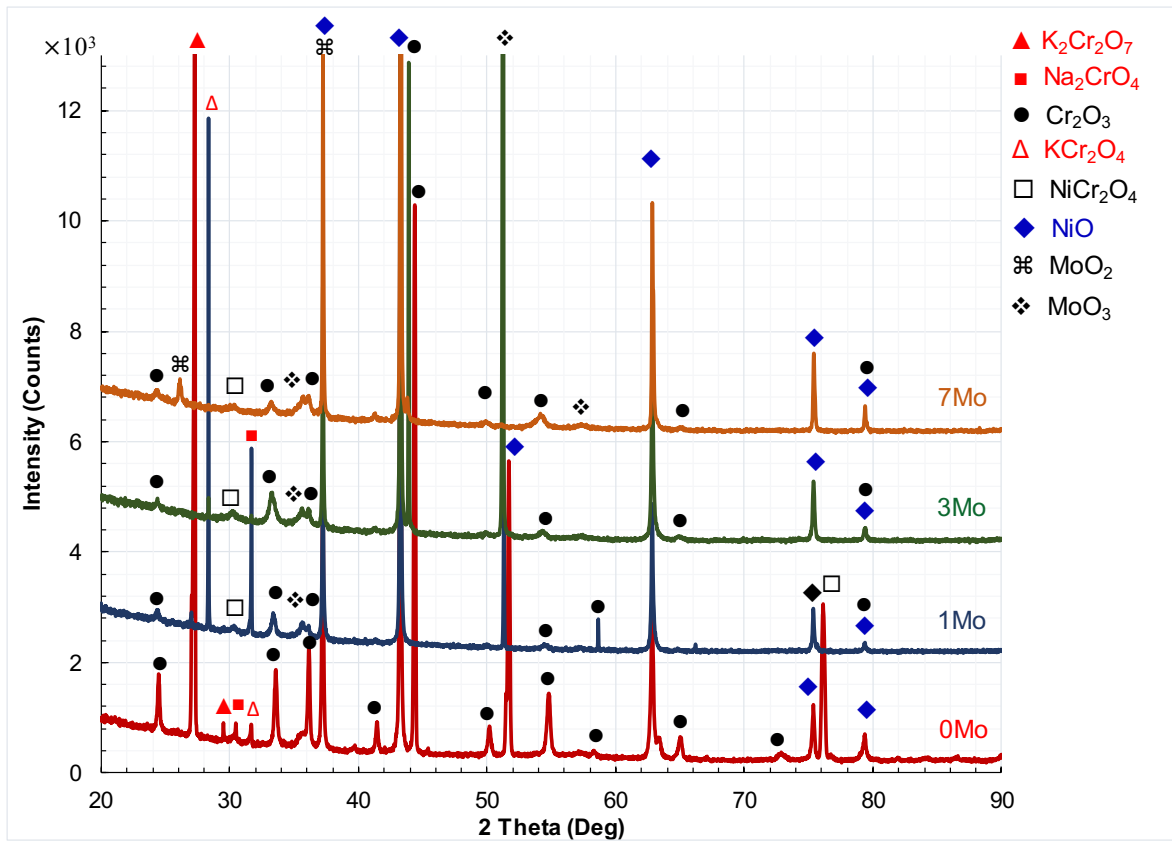
Fig. 30 XRD profiles of the Ni20Cr-xMo alloys after 100 h of corrosion in the oxidizing-chlorine containing atmosphere.

Based on the results obtained, a model for the corrosion of Ni20Cr is proposed as shown in Fig. 31. According to this model, KCl vapor reacts with a Cr_2O_3 scale to form a chromate (Fig. 31a). The generated Cl_2 by this reaction migrates through cracks and/or pores in the oxide scale and penetrates into the alloy substrate, resulting in the formation of internal Cr-chloride, which consumes the Cr in the subsurface region to form a thick Cr-depleted zone (Fig. 31b). The protective Cr_2O_3 scale is therefore converted to a less-protective oxide scale due to break down by chromate formation and significant Cr-depletion in the subsurface of the alloy. Thus, the alloy can undergo more rapid oxidation to form a thick

54

oxide scale, consisting predominantly of a Ni-spinel phase (NiCr$_2$O$_4$), which grows rapidly (Fig. 31c). This confirms that the chromates are able to accelerate the oxidation.
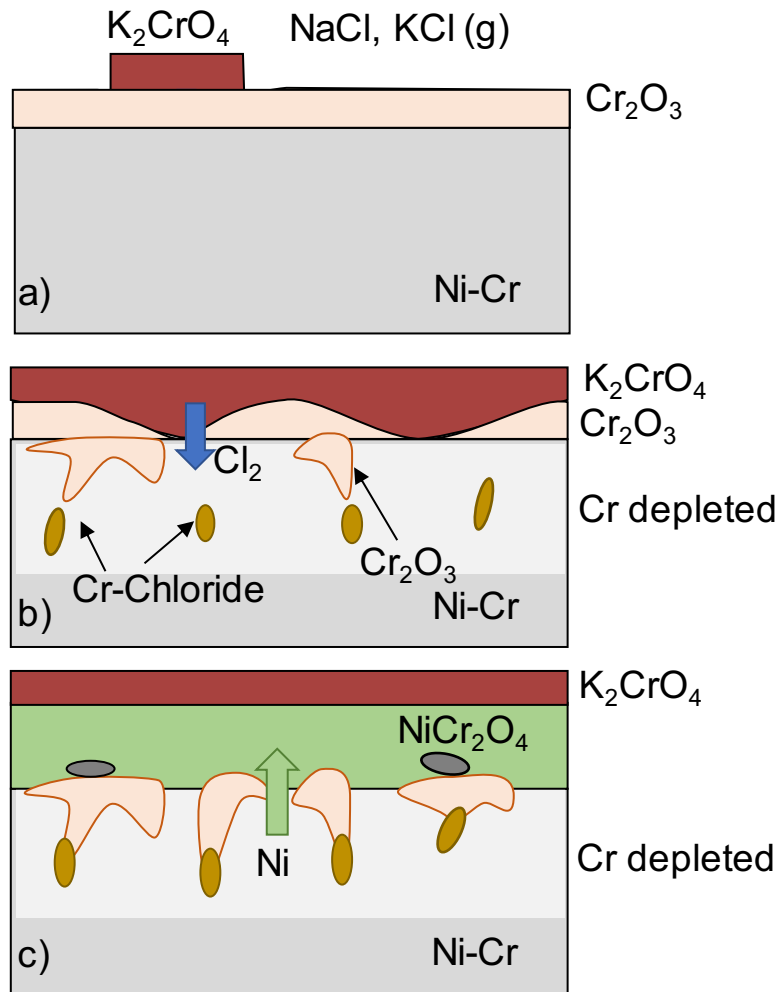
Fig. 31 Proposed model for the corrosion of Mo-free Ni20Cr alloy in the air + salt vapor atmosphere.

Corrosion for the Ni20Cr alloys containing 3 and 7 wt.% Mo led to an oxide scale with a different structure compared with the Mo-free alloy. These Mo-containing alloys formed a NiO oxide scale rather than the Cr$_2$O$_3$ scale that was formed on the Mo-free alloy. No chromates were observed on the surface of oxide scale after corrosion (Figs. 23 and 27), indicating that the Mo addition prevented the formation of chromates during corrosion process. Figure 32 shows the cross-sectional elemental distribution maps of the oxide scale formed on the 7Mo alloy after 100h of oxidation at 570°C in air. This oxide scale has a duplex structure comprising an outer NiO layer and an inner Cr-rich oxide layer. Mo was also detected in the inner Cr-rich oxide layer. Because the resolution of the EDS mapping

was not sufficient to identify, there is a possibility that Mo is present as an oxide below the NiO scale. The oxide scale formed in air has a structure similar to that of the oxide scales formed on the Mo-containing alloys during the corrosion tests, and from this structure, it is apparent that Mo addition promoted the formation of the NiO scale.
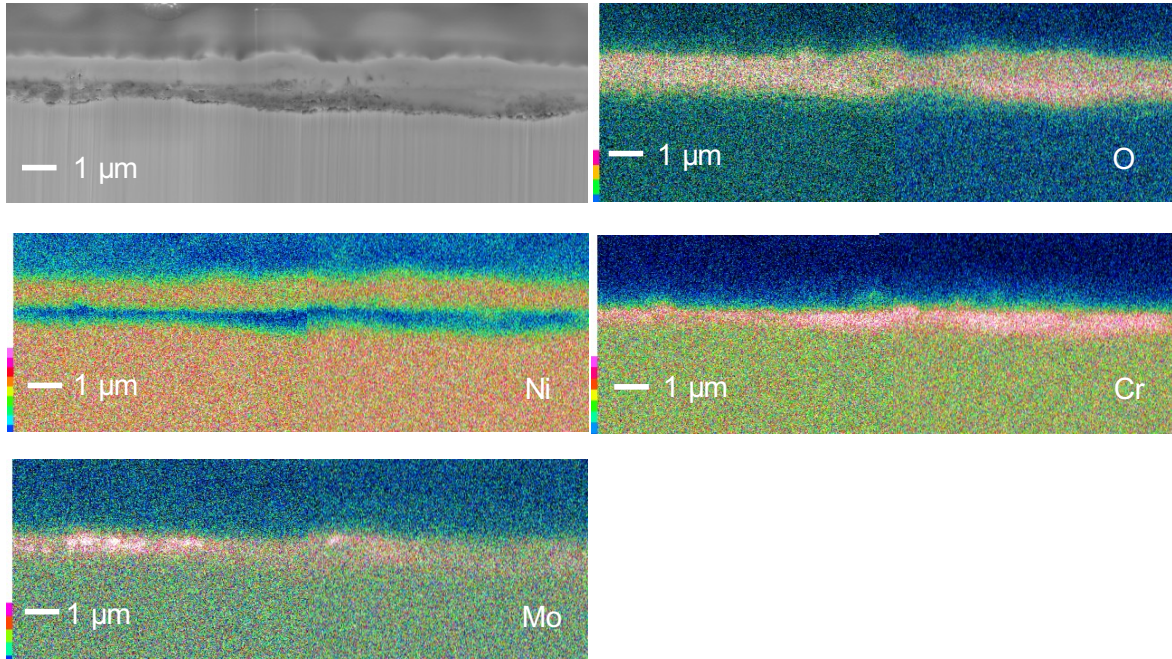
Fig. 32 Cross-sectional elemental distribution maps of the 7Mo alloy after 100h of oxidation at 570°C in air.

The reaction between NaCl and NiO is not thermodynamically feasible based on the reactions (15) [67,68], while the thermodynamic data of the reaction of KCl and NiO could not be found in the literatures. Thus, the P_{Cl_2} at the scale surface during corrosion did not increase sufficiently to cause the internal chlorination of Cr. Without internal chromium chloride formation, no Cr-depleted zone was formed. The inner Cr-rich oxide scale may act as a protective layer against corrosion. Consequently, the Mo-containing alloys exhibited better corrosion performance than that of the Mo-free alloy.

$$2NaCl(g) + NiO(s) + 1/2O_2(g) \rightarrow 2Na_2NiO_2 (s) + Cl_2(g); \hspace{2cm} (15)$$

$$\Delta G = 297.794 \text{ kJ (at } 570ºC)$$

$$KCl(g) + NiO(s) + 1/2O_2(g) \rightarrow KNiO_2 (s) + Cl_2(g); \hspace{2cm} (16)$$
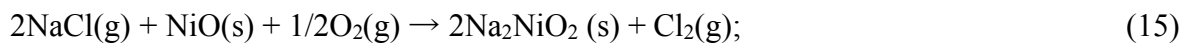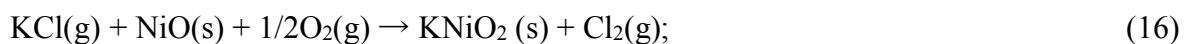
Although the P_{Cl_2} was considered to be relatively low in the absence of chromate formation, a Cl signal was still detected along with Cr and Mo in the inner oxide layer (Fig. 27). The "quasi"-stability diagram of this system (Fig. 28) suggests that $MoO_2Cl_2(g)$ could be formed below the NiO scale, once the oxygen potential at the scale/alloy interface had decreased due to the oxide scale formation. The high volatility of MoO_2Cl_2 could explain the formation of numerous pores and cavities in the inner oxide scale during corrosion (Figs. 26 and 27). At higher Mo contents, the formation of MoO_2Cl_2 increased, leading to a higher evaporation rate of metal chlorides (Fig. 20).

NaCl, KCl (g)

Ni-oxide
Cr_2O_3
Porous $Cr_2O_3+MoO_2$
Ni

a)   Ni-Cr-Mo

NaCl, KCl (g)

Cl_2 Ni-oxide
Cr_2O_3
MoO_2Cl_2 Porous $Cr_2O_3+MoO_2$
Ni

b)   Ni-Cr-Mo
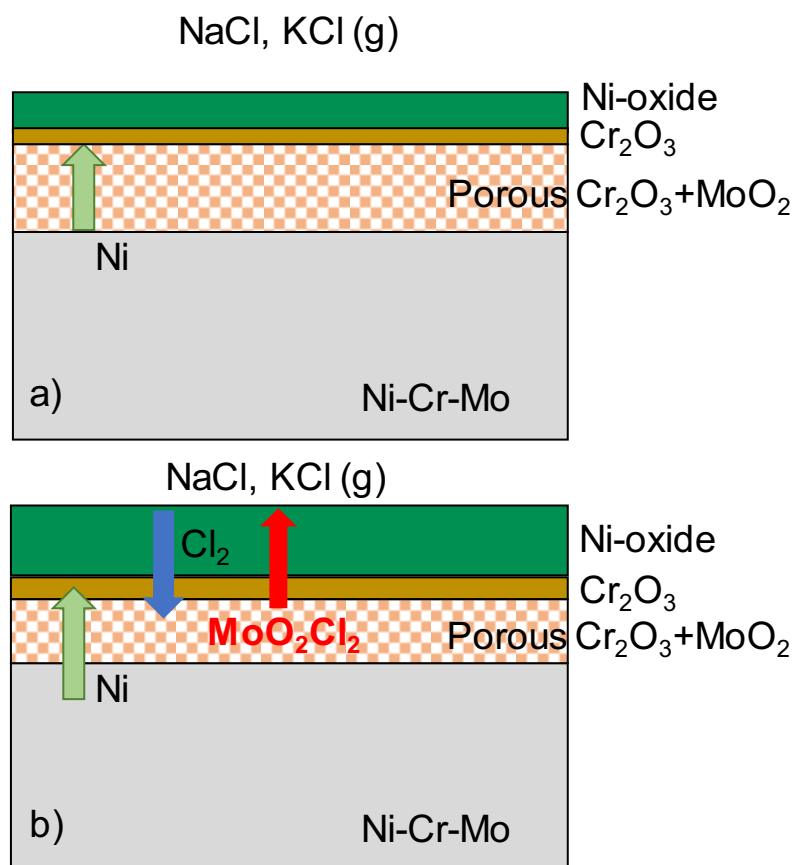
Fig. 33 Proposed model for the corrosion of Mo-containing Ni20Cr alloy in the air + salt vapor atmosphere.

A model for the corrosion of Mo containing Ni20Cr alloys is presented in Fig. 33. In the initial stage of corrosion, the alloy may form a Cr-rich oxide scale, but this scale is less-protective owing to the presence of Mo-oxide and allows the formation of an outer NiO layer, which prevents chromate formation, as depicted in Fig.33a. Thus, the chlorine potential at the surface does not increase. However, due to the formation of a NiO and/or Cr-rich oxide scale, the oxygen potential at the interface between oxide scale and alloy

substrate decreases, which promotes the Mo-oxy-chloride formation (MoO_2Cl_2). The MoO_2Cl_2, then evaporates, forming pores in the inner oxide scale (Fig. 33b) and further decreasing the protective ability of the inner Cr-rich oxide layer. Therefore, there exists an optimal Mo concentration for increasing the corrosion resistance of Ni20Cr alloy.

4.4   Conclusion

The corrosion behavior of Ni20Cr alloys containing various Mo contents (1, 3, and 7 wt.%) was investigated at 570 °C in an air + NaCl-KCl-CaCl$_2$ salt vapor mixture. The obtained results can be summarized as follows:

1. The binary Ni20Cr alloy was corroded with highest corrosion rate. Corrosion was initiated by the formation of chromate leading to the generation of chlorine. The resulting higher chlorine potential promoted the internal precipitation of chromium chloride and a Cr-depleted zone, which resulted in a less protective $NiCr_2O_4$ formation.

2. Mo addition to Ni20Cr alloy has given better the corrosion resistance in the oxidizing chlorine-containing environment. The optimal Mo content for this alloy was found to be 3 wt. %, and lower or higher Mo contents resulted in increased corrosion mass gain and metal chloride evaporation. Mo addition promoted the formation of NiO scale, which prevented the production of chromate.

3. Preventing chromate formation by NiO scale formation is one of the key points for increasing the corrosion resistance of Cr_2O_3-forming alloys in salt vapor-containing environments.

CHAPTER 5
EFFECT OF MOLYBDENUM ON CORROSION BEHAVIOR IN ARGON WITH NaCl-KCl-CaCl$_2$ VAPOR

5.1 Introduction

In the previous chapter, the corrosion behavior of NiCr-based alloys with and without Mo addition in air containing KCl-NaCl-CaCl$_2$ salt-vapor was investigated. The alloy without Mo formed chromates by the reaction between the salt-vapor and a Cr$_2$O$_3$ scale, which was formed in the early period of oxidation. The formation of chromates was considered to result in breakdown of the protective oxide scale and generate the Cl$_2$ on the surface of the oxide scale, which accelerated the corrosion. Mo addition to NiCr-based alloys was found to be beneficial because it promoted a NiO formation and a NiO scale could suppressed the chromate formation, which greatly improved the corrosion resistance.[69]

As discussed in the previous chapter, the chromate formation requires oxygen (eq 13), thus if the alloys are corroded in the atmospheres with lower oxygen potential, the corrosion of alloys must be reduced based on the mechanism proposed in the previous chapter. In order to confirm this mechanism, in this chapter the corrosion behavior of Ni-based alloys in Argon with salt-vapor environment at 570 °C was studied using Ni20Cr alloys with and without 1~7Mo (in wt. %).

5.2 Results

5.2.1 Corrosion Kinetics

The corrosion mass gain kinetics of the alloys during corrosion time was shown in the Fig. 34a. The corrosion mass gain (ΔW_g) of the Mo-free alloy was considerably lower than that of the Mo containing alloys. In addition, the corrosion mass gain of the Mo-free alloys was much lower than that in air + salt vapor, and the mass gain of the alloys with Mo was greater than that in air + salt vapor, indicating that Mo addition decreased the corrosion resistance of the Ni20Cr alloy in the low oxidizing-chlorine containing atmosphere. This result was contradictory compared with the results in the oxidizing-chlorine containing atmosphere

(see 4.1.1. section). With more addition of Mo up to 3 wt.% of Mo, the corrosion rate of the Ni20Cr alloy became higher. 7 wt.% of Mo addition had the same mass gain as ΔW_g as the 3 wt.% Mo addition. The kinetics profiles of all the alloys except the 1 Mo alloy displayed linear-like rate growth behavior indicating that reaction kinetic of all the alloys was dominated by gas-mass transfer. The kinetic profile of 1 wt.% Mo alloy displayed a parabolic-like behavior.
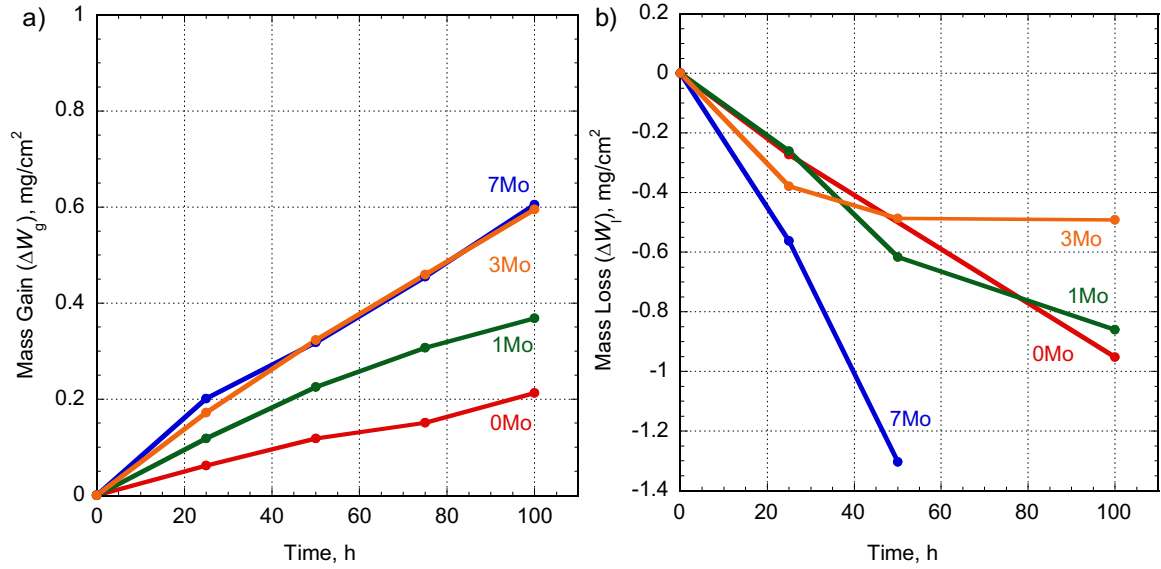
Fig. 34 (a) Corrosion mass gain (ΔW_g), and (b) Mass loss (ΔW_l) for the Ni20Cr-xMo alloys as a function of corrosion time at 570°C in the low oxidizing-chlorine containing atmosphere.
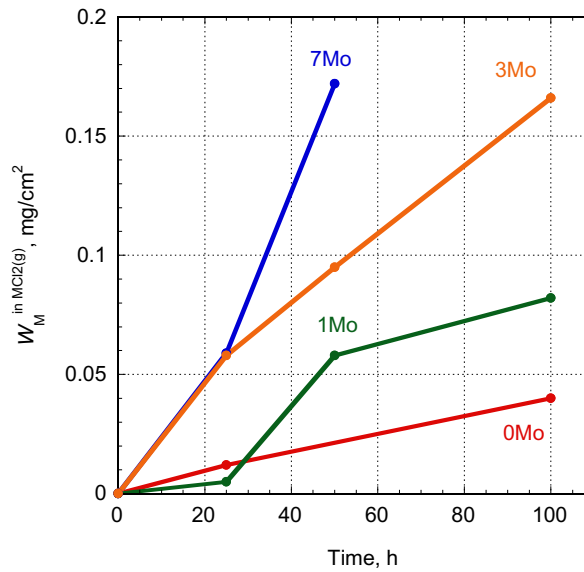
Fig. 35 Calculated metal loss due to evaporation of metal chlorides ($W_M^{in\ MCl2(g)}$) for the Ni20Cr-xMo alloys during the corrosion tests at 570°C in the low oxidizing-chlorine containing atmosphere.

Figure 34b shows the profile of total mass loss (ΔW_l) after the corrosion test in the low oxidizing-chlorine containing atmosphere. The mass loss profiles exhibited a trend similar to that of the mass gain profiles. The ΔW_l profile of Mo-free alloy displayed the lowest mass loss with tendency to decrease linearly over time. While, the Mo containing alloys had different behavior. The mass loss kinetics of Mo containing alloys was initially rapid, then decreased slowly for longer corrosion time.

The calculated metal loss due to evaporation of metal chlorides ($W_M^{\text{in MCl2(g)}}$) was shown in Fig. 35. The data of evaporation of metal chlorides of 7 wt.% Mo addition after 100 h of the corrosion was inconsistent with other mass loss results, thus results is not shown in Fig. 34b. The Mo-free alloy had linear evaporation rate of the metal chlorides and displayed the lowest amount of evaporation of the metal chlorides. Although the 1 Mo alloy showed low evaporation at the beginning of the corrosion test up to 25 h, higher Mo addition resulted in higher evaporation and the evaporation of metal chlorides was increased rapidly with longer corrosion time, indicating that Mo addition led the greater evaporation of metal chlorides. It might be due to the formation and evaporation of molybdenum chloride or oxychloride which have higher vapor pressure.

From the comparison between Figs. 34 and 35, the degree of $W_M^{\text{in MCl2(g)}}$ is still much lower than that of ΔW_l and ΔW_g, thus, the evaporation of chlorides can be consider to not strongly affect the corrosion mass gain/loss in the low oxidizing-chlorine containing atmosphere, similar with previous results in the oxidizing-chlorine containing atmosphere.

5.2.2   Surface Morphology of Corroded Samples

Figure 36-38 show the surface morphologies and elemental distribution maps of the corroded samples after a corrosion test for 100 h in the low oxidizing-chlorine containing atmosphere. The oxide scale completely covered all the sample surfaces
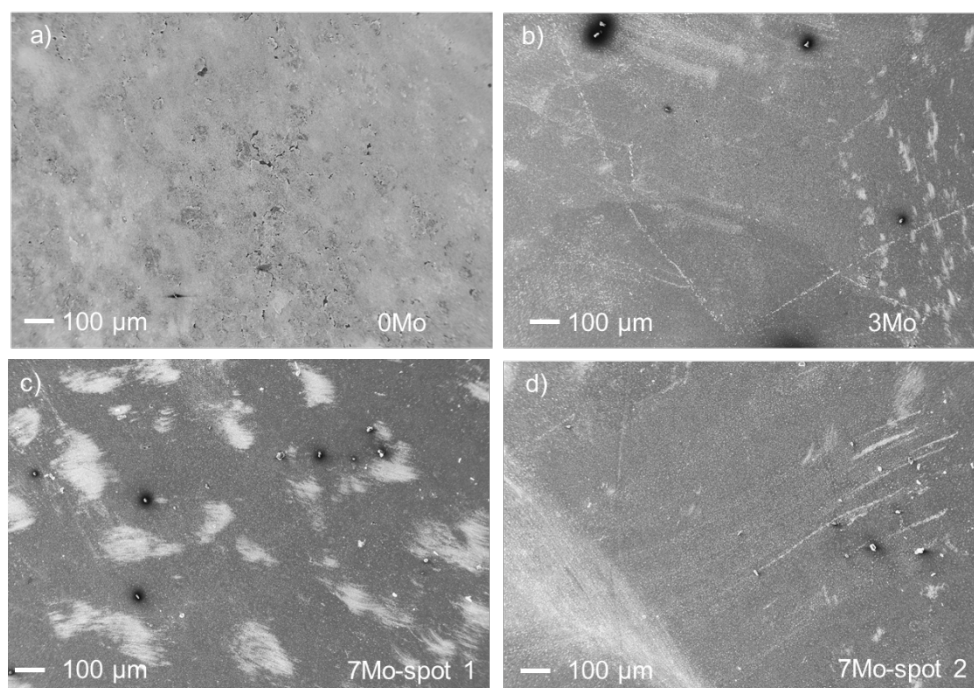
Fig. 36 Surface morphologies of the corroded samples after corrosion test for 100h in the oxidizing-chlorine containing atmosphere: (a) 0Fe; (b) 3Mo; (c) 7Mo; and d) a localized area on 7Mo.
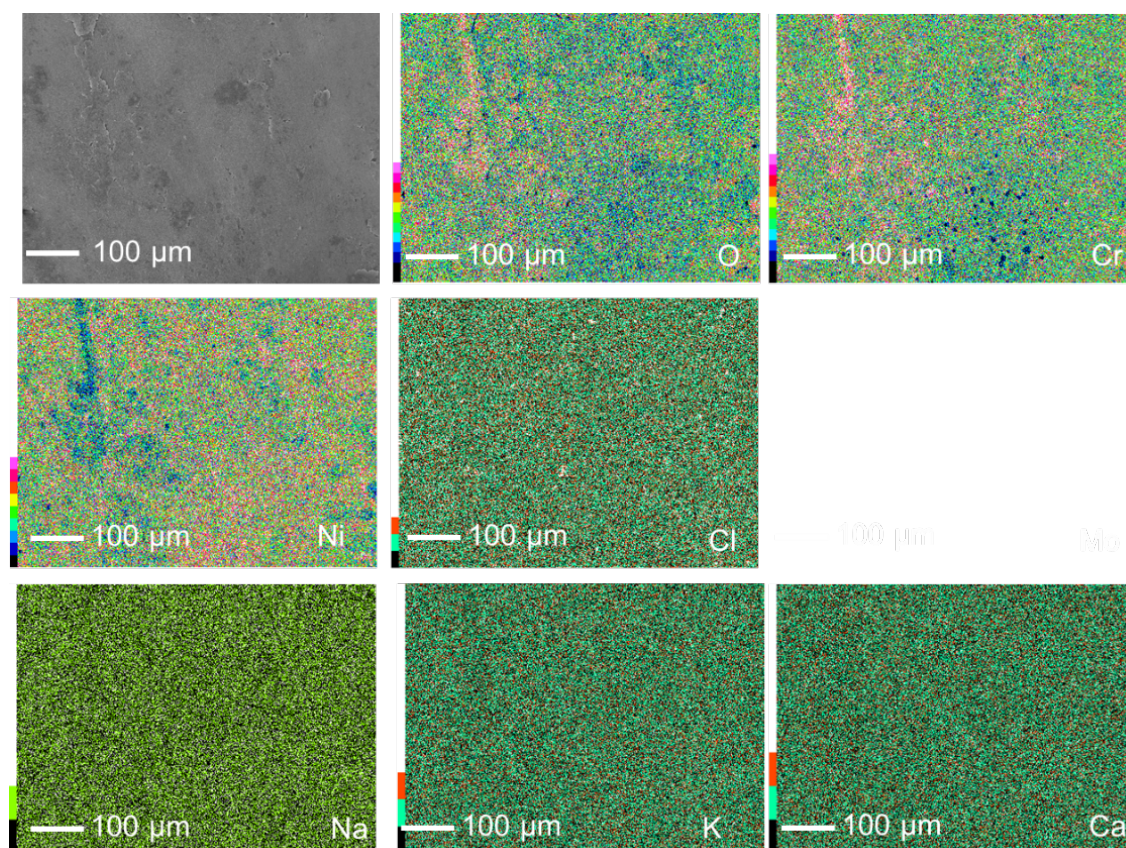
Fig. 37 Surface elemental distribution maps of the corroded sample with 0Mo after 100 h of corrosion in the low oxidizing-chlorine containing atmosphere.

On the surface of Mo-free alloy, the oxide scale was divided into two areas: light grey and dark grey area. These areas were predominantly composed of chromium oxide, and nickel oxide respectively, based on the EDS mapping on Fig. 37. Some area of spalled oxide scale which was identified as chromium oxide was also observed on the Mo-free alloy surface. The dendritic-structure products, and elements of alkali salts (Na, K, Ca, and Cl) signals which were observed after the corrosion in the oxidizing-chlorine containing atmosphere, was not found on the EDS mapping of the Mo-free alloy surface (Fig. 38).

Meanwhile, on the surfaces of 3 Mo and 7 Mo alloys as shown in Figs. 36 and 38, some of white spots were observed but could not be identified its element. Thus, the white spots were assumed as contaminants. No Na, K, Ca and Cl signals were also detected from the EDS mapping of the Mo containing alloys.
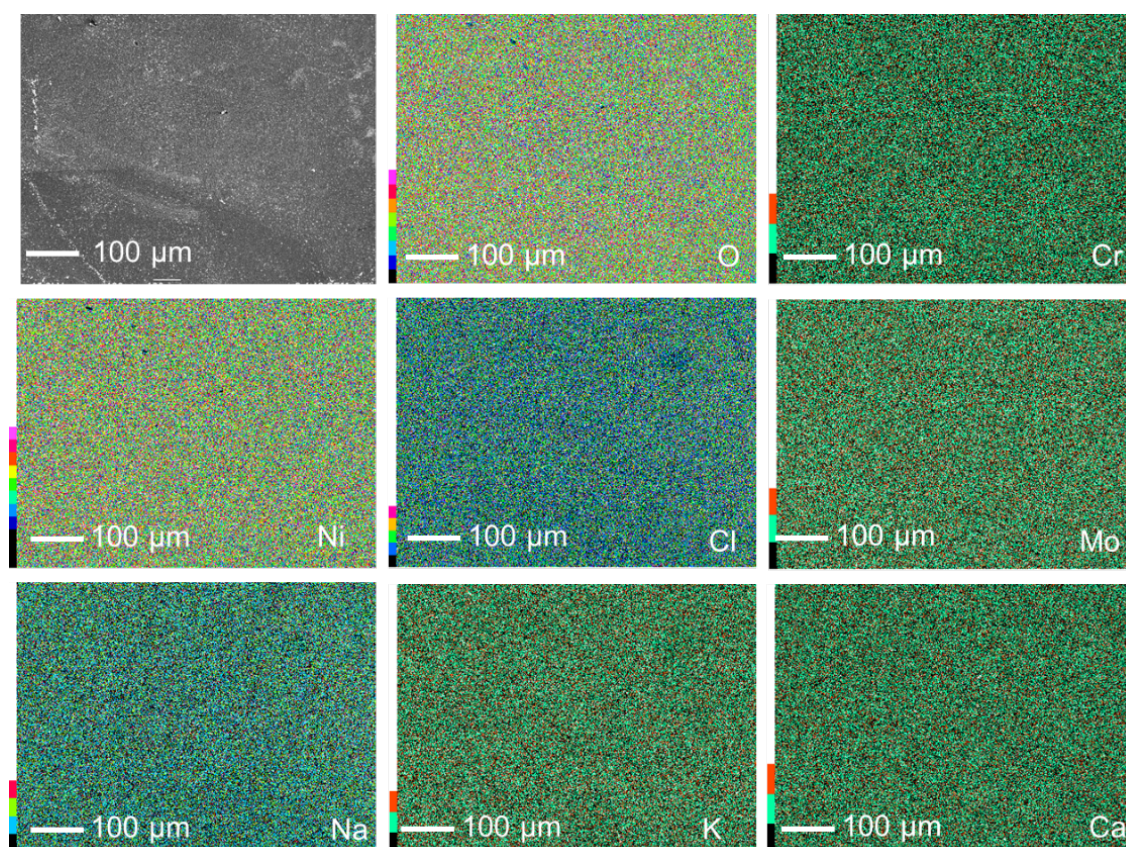
Fig. 38 Surface elemental distribution maps of corroded sample with 3Mo after 100 h of corrosion in the low oxidizing-chlorine containing atmosphere.
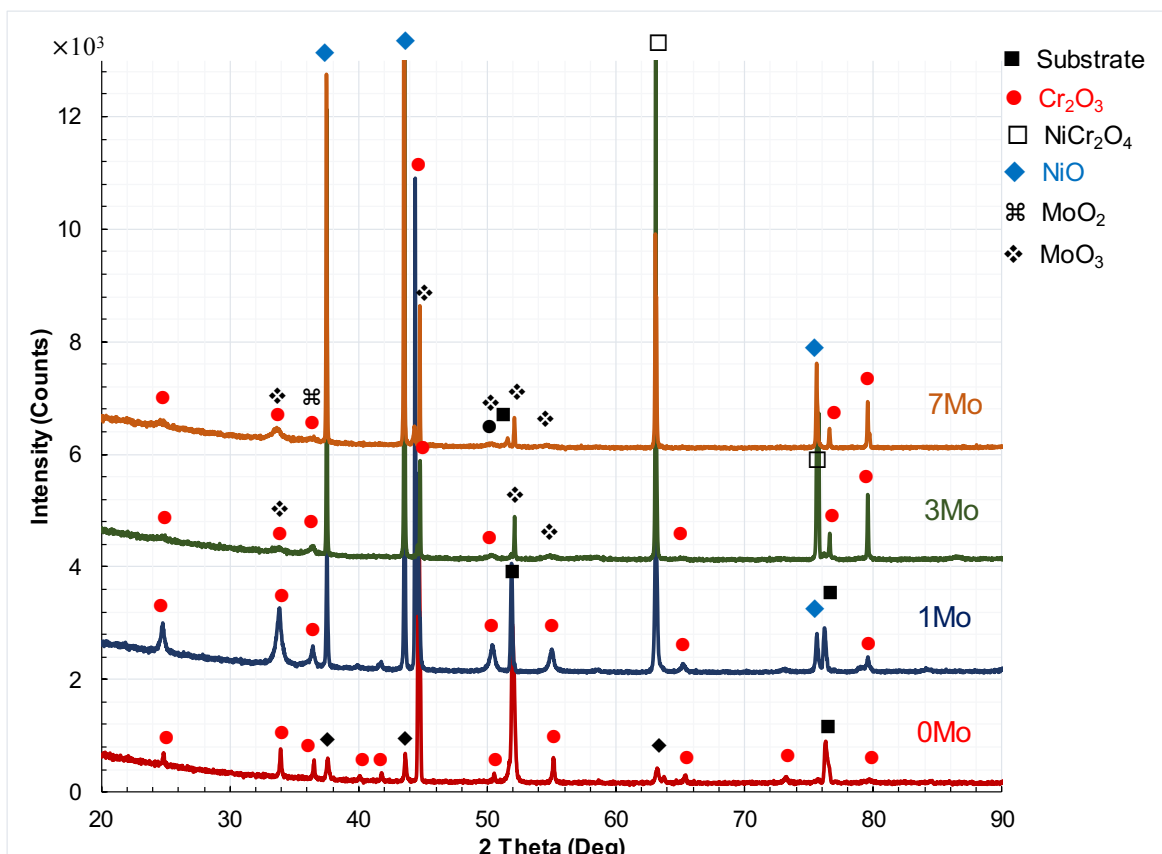
Fig. 39 XRD profiles of the Ni20Cr-xMo alloys after 100h of corrosion in the low oxidizing-chlorine containing atmosphere.

Figure 39 shows the XRD patterns of the alloys after corrosion test. The corrosion products identified were only oxides, no chromate and chlorides were detected from the surface of the alloys after corrosion test, indicating that the chlorination reaction was greatly reduced in the low oxidizing-chlorine containing atmosphere.

5.2.3 Cross-Sectional Observation of Corroded Samples

Figure 40 displayed cross-sections of all of the samples after corrosion test for 100 h in the low oxidizing-chlorine containing atmosphere. The oxide scale structure formed on all the alloys after the corrosion in the low oxidizing-chlorine containing atmosphere was quite different from those formed after corrosion in the oxidizing-chlorine containing atmosphere.

For the Mo-free alloy, a thin "nodule-like" oxide scale was formed on the alloy. Meanwhile a thick dense continuous oxide scale with internal "island-like" products were formed on the Mo containing alloys.
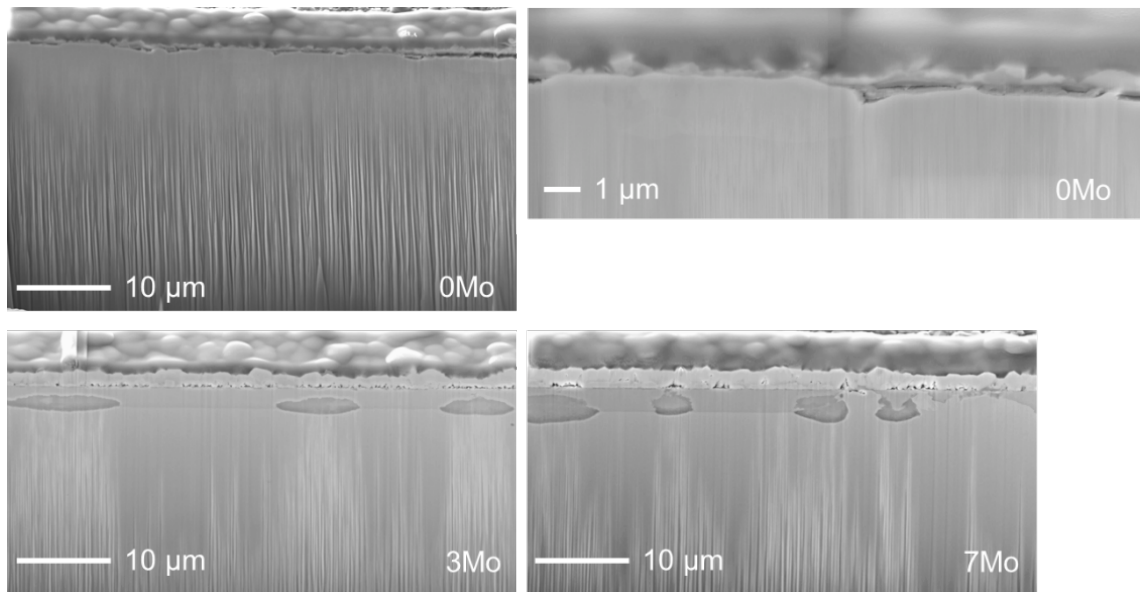
Fig. 40 Cross-sections of the Ni20Cr-xMo alloys after corrosion test for 100 h in the low oxidizing-chlorine containing atmosphere: a) 0Mo low magnification; b) 0Mo high magnification; c) 3Mo; and d) 7Mo
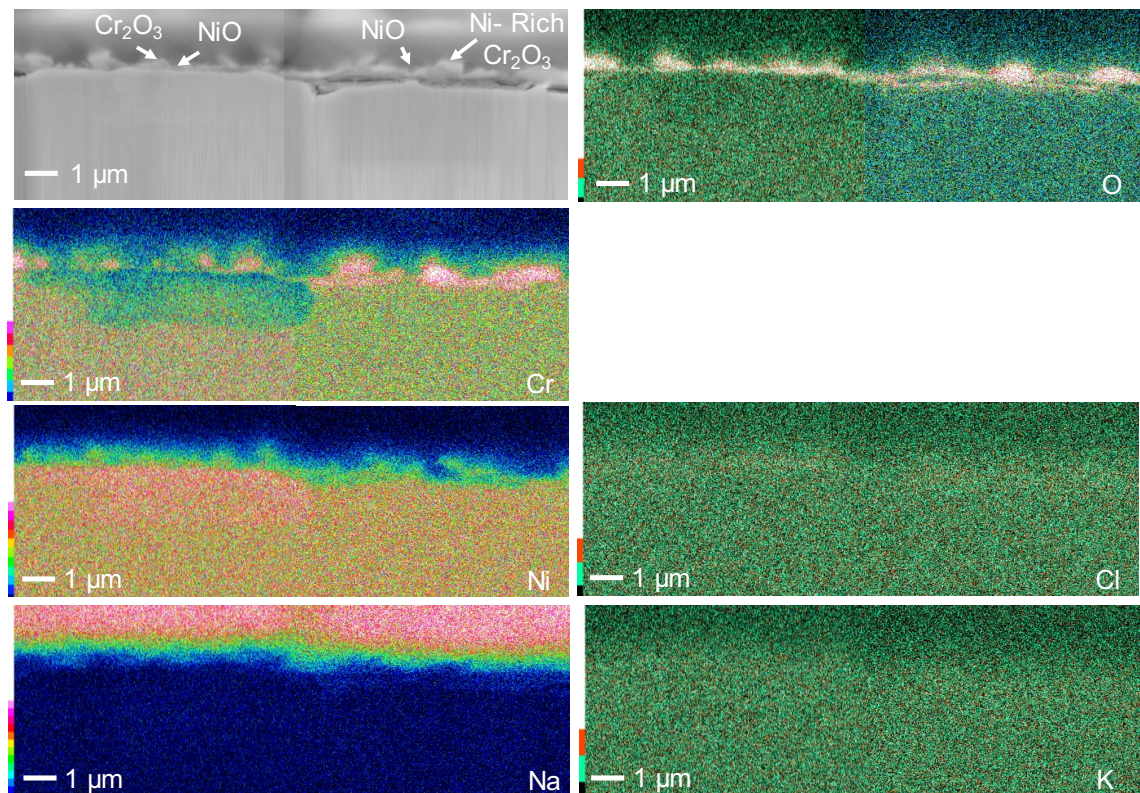
Fig. 41 Cross‑sectional elemental distribution maps of the 0Mo alloy after 100 h of corrosion in the low oxidizing-chlorine containing atmosphere.

Based on the EDS mapping in Fig. 41, the nodules were predominantly composed of Cr_2O_3, NiO and mixed of NiCr oxide. Some voids and gaps were observed below the oxide scale. From the XRD profile shown in Fig. 39, the NiCr oxide was identified as $NiCr_2O_4$. A Cr-depletion zone was formed in some localized areas. However, the area of Cr-depletion zone was significantly small comparing to the samples corroded in the oxidizing-chlorine containing atmosphere. X-ray- signals of Na, K, Ca and Cl were not detected on the EDS mapping of Mo-free alloy in the Fig. 41, indicating that the internal chlorination was not occurred in the low oxygen atmosphere.
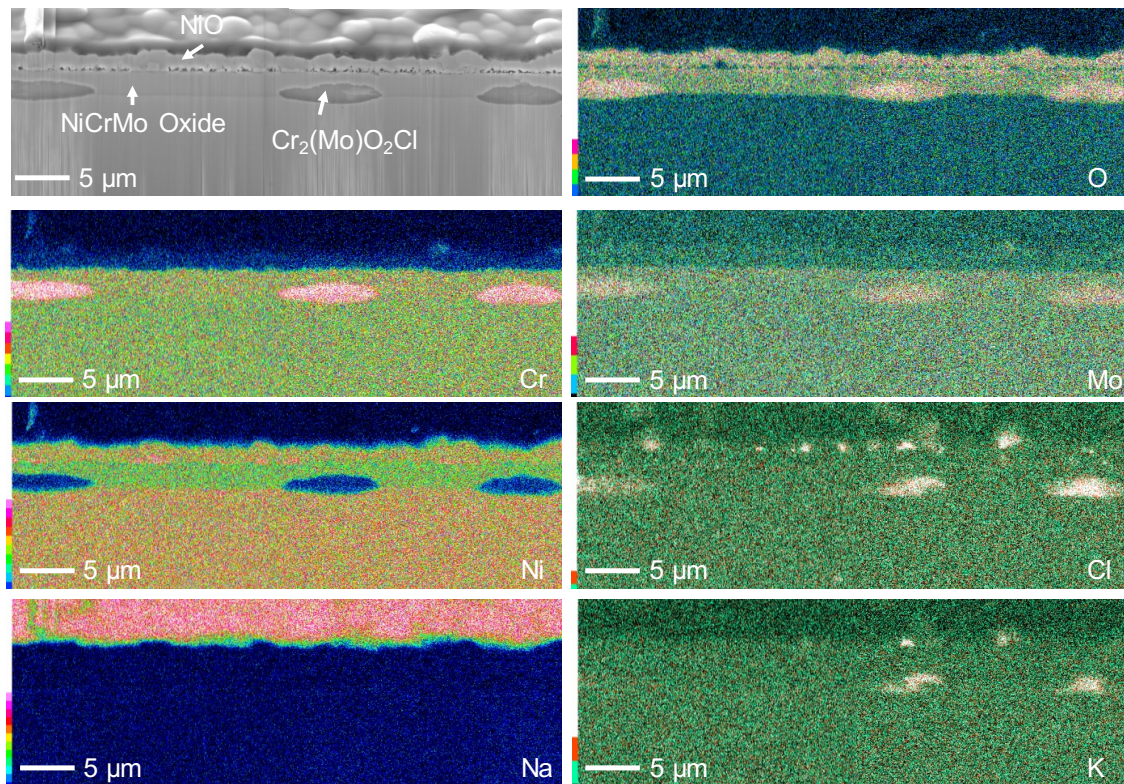
Fig. 42 Cross‑sectional elemental distribution maps of a localized area of the 3Mo alloy after 100 h of corrosion in the low oxidizing-chlorine containing atmosphere.

The oxide scale formed on the Mo consisted of duplex with continuous dense outer and inner layers. In the inner layer, "islands-like" corrosion products were observed. The EDS mapping shown in Figs. 42 and 43 exhibited the outer oxide scale which was composed of predominantly NiO. The outer scale formed on the 7Mo alloy was thicker compared with that on the 3Mo alloy. The inner layer can be $NiCr_2O_4$ based on the EDS and XRD analysis. The thickness of the inner layer formed on both Mo containing alloys was relatively same.

Mo was slightly enriched in the inner layer. The "islands-like" structure confirmed in the inner layer was composed with Cr, Mo, O and Cl, suggesting a formation of Mo-Cr oxychlorides. The potassium signals were also detected in the "island-like" corrosion products, suggesting that KCl could penetrate through the oxide scale. A Cr_2O_3 oxide layer was locally formed accompanied with a Cr-depleted zone on the 7Mo alloy, but was not on the 3Mo alloy
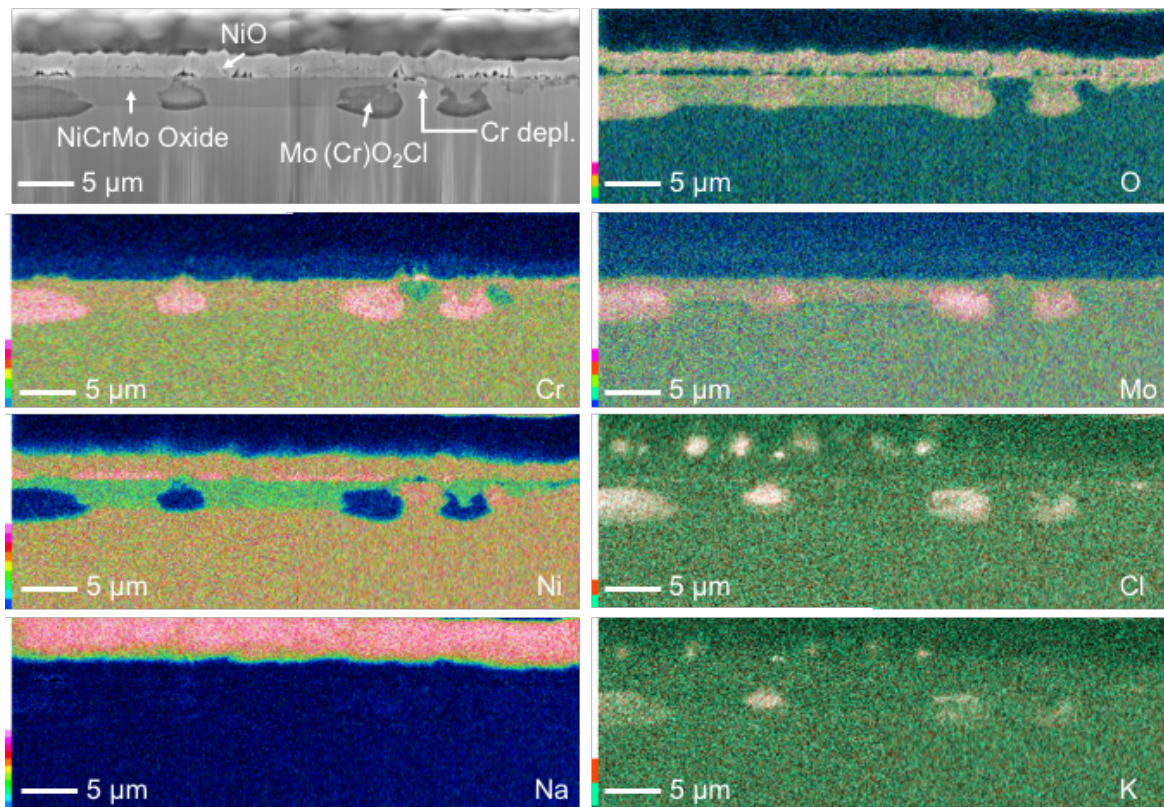
Fig. 43 Cross‑sectional elemental distribution maps of a localized area of the 7Mo alloy after 100 h of corrosion in the low oxidizing-chlorine containing atmosphere.

5.3 Discussion

In the low oxidizing-chlorine containing atmosphere with Ar, the corrosion performances of Ni20Cr-based alloys with and without Mo addition was found to be contradictive compared with the results in the oxidizing-chlorine atmosphere. The Mo-free alloy showed better corrosion resistance in this atmosphere than the Mo-containing alloys. This result strongly indicates that the oxygen in the atmosphere had really affected the corrosion behavior in the chlorine containing atmosphere, particularly for the Ni20Cr-based alloy. In fact, the

corrosion mass gain formed on the alloys after corrosion in the oxidizing-chlorine containing atmosphere as presented on the Fig. 19a (chapter 4.2) was considerably higher than that of in the low oxidizing-chlorine containing atmosphere (Fig. 34a).

The P_{Cl_2} in the low oxidizing-chlorine containing atmosphere which was calculated by FactSage [65], 1.66×10^{-11} atm, was found to be lower than in the oxidizing-chlorine containing atmosphere ($P_{Cl_2} = 3.7 \times 10^{-6}$ atm). Figure 44 shows the "quasi diagram" of Ni20Cr-7Mo-O-Cl system. This diagram was also calculated with the critical vapor pressure of gaseous metal chlorides 9.87×10^{-5} atm, as explained briefly in the previous chapter [27]. Based on Fig. 44, even though the chlorine potential is lower in the low oxidizing-chlorine containing atmosphere, the effect of this lower chlorine potential does not indicate any thermodynamically difference on the stability of corrosion products with the comparison to the higher chlorine potential, thus, this is not a reason for the lower corrosion mass gain for Mo-free alloy and higher corrosion mass gain for Mo-added alloys.
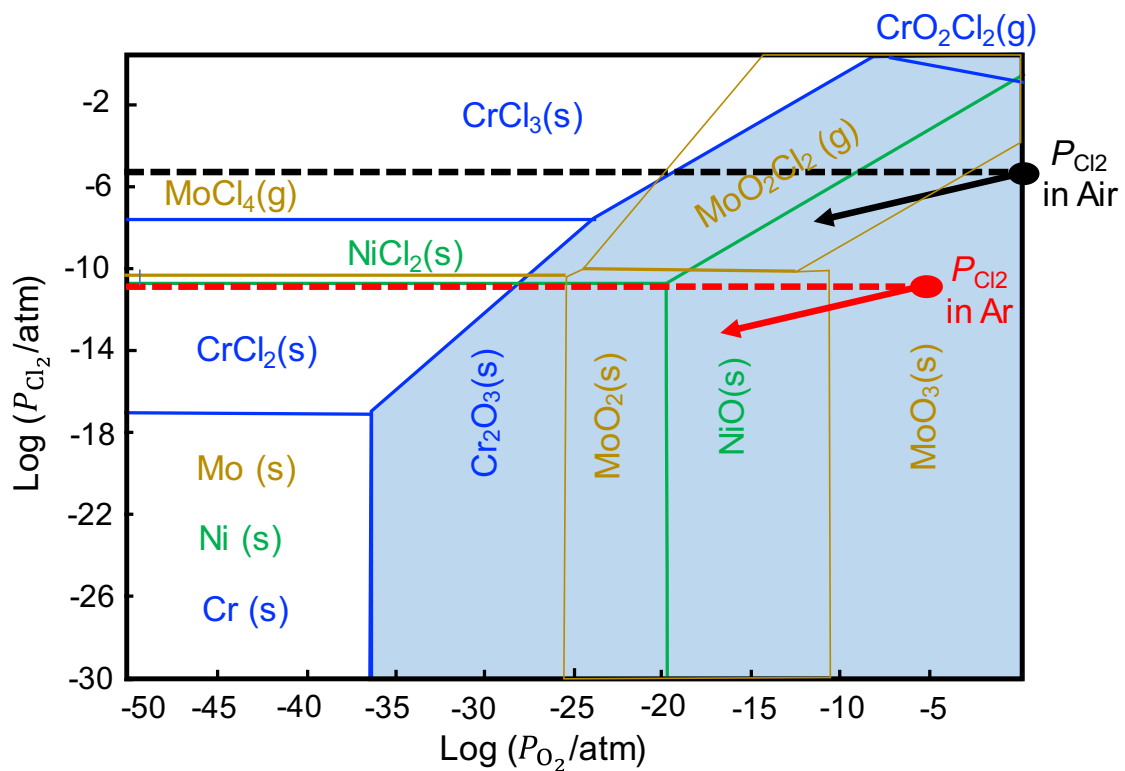
Fig. 44 "Quasi"-stability diagram for the Ni20Cr-7Mo-O-Cl system at 570ºC with $a_{Ni}= 0.5615$, $a_{Cr}= 0.1332$, $a_{Mo}=0.0237$, and $P_{MCl_2(g)} = 9.87 \times 10^{-5}$ atm: a) in Air ($P_{O_2} = 0.2$ atm, $P_{Cl_2} = 3.7 \times 10^{-6}$ atm); b) in Ar ($P_{O_2} = 9.99 \times 10^{-6}$ atm, $P_{Cl_2} = 1.66 \times 10^{-11}$ atm).

Under high oxygen potential 0.2 atm, in the oxidizing-chlorine containing atmosphere, the Mo-free alloy produced a thick oxide scale and a Cr internal oxidation/chlorination zone. The formation of internal chlorination zone was explained due to chromate formation in chapter 4 [69]. However, in the atmosphere with the low oxidizing-chlorine containing atmosphere, no chromates formation was observed from the EDS mapping analysis in the Figs. 36-38 and was the XRD profile in the Fig. 39. The Cr_2O_3 scale formation was observed on the alloy after 100 h of corrosion in Fig. 41, thus it might be possible to form chromates with sufficient oxygen potential, based on the reactions (13) and (14) in the chapter 4.

In the low oxidizing-chlorine containing atmosphere, the free energy change of chromates formation was evaluated using following reactions with $P_{Cl_2} = 1.66 \times 10^{-11}$ atm, $P_{O_2} = 9.99 \times 10^{-6}$ atm (impurity of Ar gas), and $P_{KCl} = = 3.38 \times 10^{-6}$ atm. It is apparent that the free energy change of the reaction has positive value, suggesting that the chromate formation cannot be possible in the low oxidizing-chlorine containing atmosphere.

$4KCl(g) + Cr_2O_3(s) + 5/2O_2(g) \rightarrow 2K_2CrO_4(s) + 2Cl_2(g);$

ΔG (18) = 330,406 kJmol^{-1} (at 570ºC) (18)

$4NaCl(g) + Cr_2O_3(s) + 5/2O_2(g) \rightarrow 2Na_2CrO_4(s) + 2Cl_2(g);$
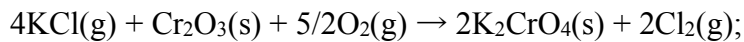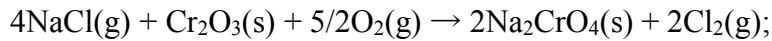
ΔG (19) = 344,284 kJmol^{-1} (at 570ºC) (19)

Thus, in the low oxidizing-chlorine containing atmosphere, a protective Cr_2O_3 scale could protect the alloy substrate. Moreover, since chorine was not generated due to the absence of the chromate formation, no significant corrosion occurred.

Meanwhile, the corrosion for the Mo containing alloys in the low oxidizing-chlorine atmosphere led formations of a continuously dense NiO as an outer oxide scale and dense inner oxide scale with "island-like" corrosion products composed of high Cr-Mo oxychlorides. This kind of structure was considerably different than that was formed after corrosion in the oxidizing-chlorine atmosphere, particularly in the inner part of oxide scale. Thus, a NiO formed on Mo containing alloys, which was beneficial for the oxidizing-chlorine atmosphere to prevent the chromates formation, allowed to penetrate chlorine and

KCl gas into the alloy surface. Then those gas species reacted with the Cr and Mo to form highly volatilized oxychloride.

The contradictive report for the effects of Mo alloying on the corrosion behavior in the reducing atmosphere as reported by other studies [27,54] can be interpreted due to different oxygen potential and deferent formation behavior of chromate.

5.4   Conclusion

The corrosion behavior of Ni20Cr alloys containing various Mo contents (1, 3, and 7 wt.%) was investigated at 570 °C in an Ar + NaCl-KCl-CaCl$_2$ salt vapor mixture. The obtained results can be summarized as follows:

1) The Ni20Cr-based alloy has better corrosion performance in this low oxidizing-chlorine containing atmosphere than that of the Mo containing alloys.

2) The corrosion results in the Ar with salt vapor atmosphere were contradictive to that of in the air with salt vapor atmosphere, showed that the oxygen heavily affected the corrosion behavior in the chlorine containing atmosphere.

3) The Mo-free alloys formed a thin continuous protective Cr$_2$O$_3$ scale which protected the alloy during corrosion. Meanwhile, Mo-containing alloys formed a dense NiO outer scale and a dense inner oxide layer with Cr-Mo oxychloride during the corrosion. A protective Cr$_2$O$_3$ scale can stop the penetration of chlorine and KCl gas if chromate was not formed. However, a NiO allowed the penetration of those corrosive gas species.

4) No chromate and internal Cr-precipitation zone were formed on the all of alloys. This confirmed the proposed corrosion mechanism for corrosion behavior of the Ni20Cr alloy in the oxidizing-chlorine containing atmosphere, as explained in the chapter 4.

CHAPTER 6
EFFECT OF IRON ON CORROSION BEHAVIOR IN AIR WITH NaCl-KCl-CaCl₂ VAPOR

6.1   Introduction

The previous chapter revealed that the corrosion of NiCr-based alloys in the atmosphere containing KCl-NaCl-CaCl$_2$ salt-vapor was strongly affected by the chromates which was formed by the reaction between the salt-vapor and Cr$_2$O$_3$ scale. The chromates accelerated the corrosion as a result of concomitant generation of chlorine. But, a formation of a Ni-oxide scale which was formed on NiCr-based alloys with Mo addition was able to reduce the chromate formation and increase the corrosion resistance by reducing the Cl$_2$ potential [69]. Thus, it can be expected that Fe-oxides which is also less protective as Ni-oxide is able to suppress the formation of chromates.

Therefore, in this chapter, the effect of Fe addition on the corrosion behavior of Ni20Cr-xFe alloys in atmospheres containing air and salt-vapor at 570 °C was studied. Fe additions of 4 and 30 wt.% were chosen to represent the effect of low and high Fe contents on corrosion behavior.

6.2   Results

6.2.1   Corrosion Kinetics

Figure 45a shows the corrosion mass gain kinetics of the alloys in the oxidizing-chlorine containing atmosphere. The kinetics displayed parabolic-like behavior. The corrosion mass gain (ΔW_g) of the Fe containing alloys was considerably lower than that of the Fe-free alloy, indicating that Fe addition improved the corrosion resistance of the Ni20Cr alloy. The maximum benefit was observed for 4 wt.% of Fe addition, and further increasing Fe contents to 30 wt.% decreased the corrosion resistance. Figure 45b shows the profile of total mass loss (ΔW_l) after the corrosion test. The mass loss profiles exhibited a trend similar to that of the mass gain profiles. The Fe-free alloy displayed the greatest mass loss, which tended to

decrease linearly over time, whereas the alloy with 4 wt.% Fe exhibited the lowest mass loss. The mass loss kinetics of Fe-containing alloys exhibited parabolic-like behavior.
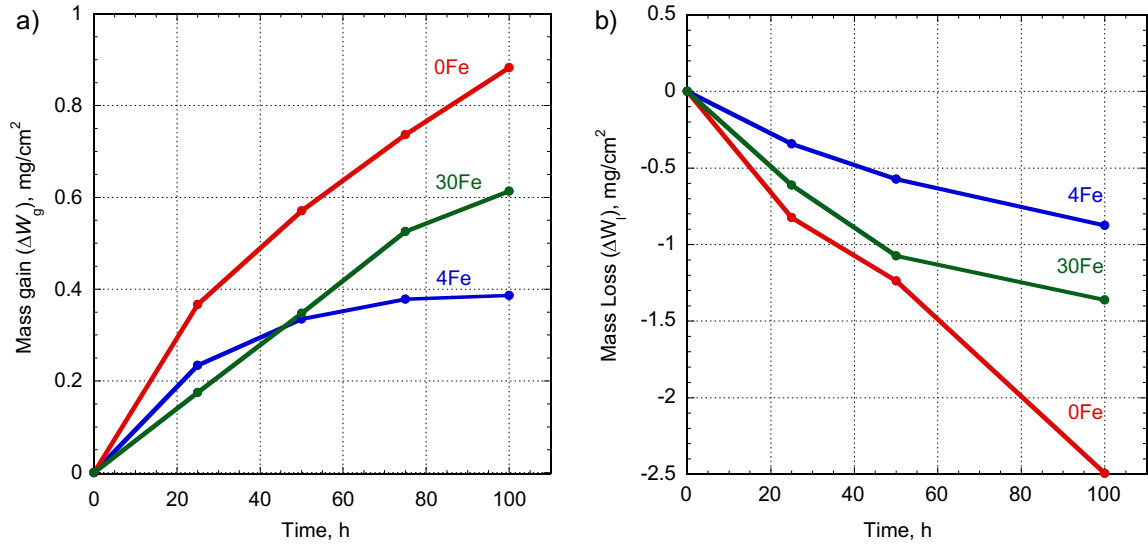
Fig. 45 (a) Corrosion mass gain (ΔW_g), and (b) Mass loss (ΔW_l) for the Ni20Cr-xFe alloys as a function of corrosion time at 570°C in the oxidizing-chlorine containing atmosphere.

Figure 46 shows the calculated metal loss due to evaporation of metal chlorides ($W_M^{\text{in MCl}_2(g)}$), which increased exponentially with increasing corrosion time for all three alloys. Among the three alloys, the highest amount of metal chloride evaporation was observed for the Fe-free alloy from the start of the corrosion test. The mass of evaporation of the metal chlorides decreased with increasing Fe contents. Although, the order of $W_M^{\text{in MCl2}(g)}$ is much smaller than that of ΔW_l and ΔW_g, the evaporation of the chlorides does not strongly affect the corrosion kinetics, higher evaporation of metal chlorides may be one of the reasons for the linear mass loss kinetics observed for the Fe-free alloy. The mass of evaporation of the metal chlorides decreased with increasing Fe contents. The plots shown in Figs. 45 and 46 suggested that Fe addition was beneficial for reducing the evaporation of metal chlorides.
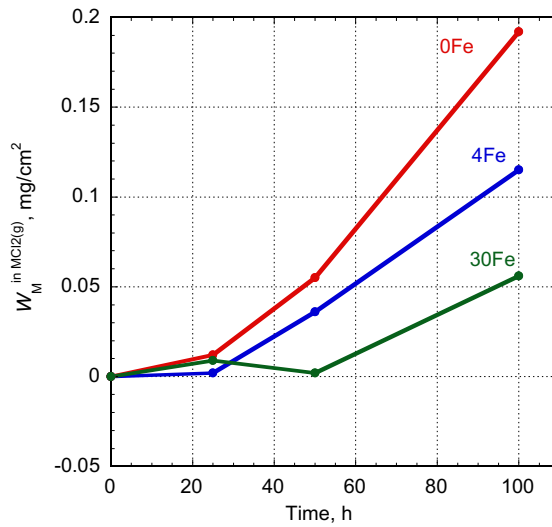
Fig. 46 Calculated metal loss due to evaporation of metal chlorides ($W_{\mathrm{M}}^{\mathrm{in\ MCl2(g)}}$) for the Ni20Cr-xFe alloys during the corrosion tests at 570°C in the oxidizing-chlorine containing atmosphere.

6.2.2   Surface Morphology of Corroded Samples

Figures 22 and 47-49 show the surface morphologies and elemental distribution maps of the corroded samples after a corrosion test for 100 h in the oxidizing-chlorine containing atmosphere. The surfaces of all samples were covered by oxide scale, and dendritic-structured products were confirmed on the surface of oxide scale. The size and distribution of these dendritic-structured products were independent of the Fe content of the alloy. Based on EDS mapping images, the dendritic products were predominantly composed of NaCl (Figs. 48 and 49).

The oxide scale could be divided into two areas with bright or dark contrast. The EDS mapping images in Figs. 48 and 49 revealed that the dark-contrast area was predominantly composed of K, Cr and O, whereas the bright-contrast area mainly contained Fe, Cr, and O. These results suggest that dark-and bright- contrast areas were potassium chromate and iron-chromium spinel, respectively. The dark-contrast area tended to decrease with increasing Fe contents in the alloy, which indicates that Fe addition reduced potassium chromate formation. The chromate formation has been also confirmed by the XRD profile (Fig. 50) through identification some peaks with chromate phases, e.g. K_2CrO_4, $K_2Cr_2O_7$, and Na_2CrO_4.
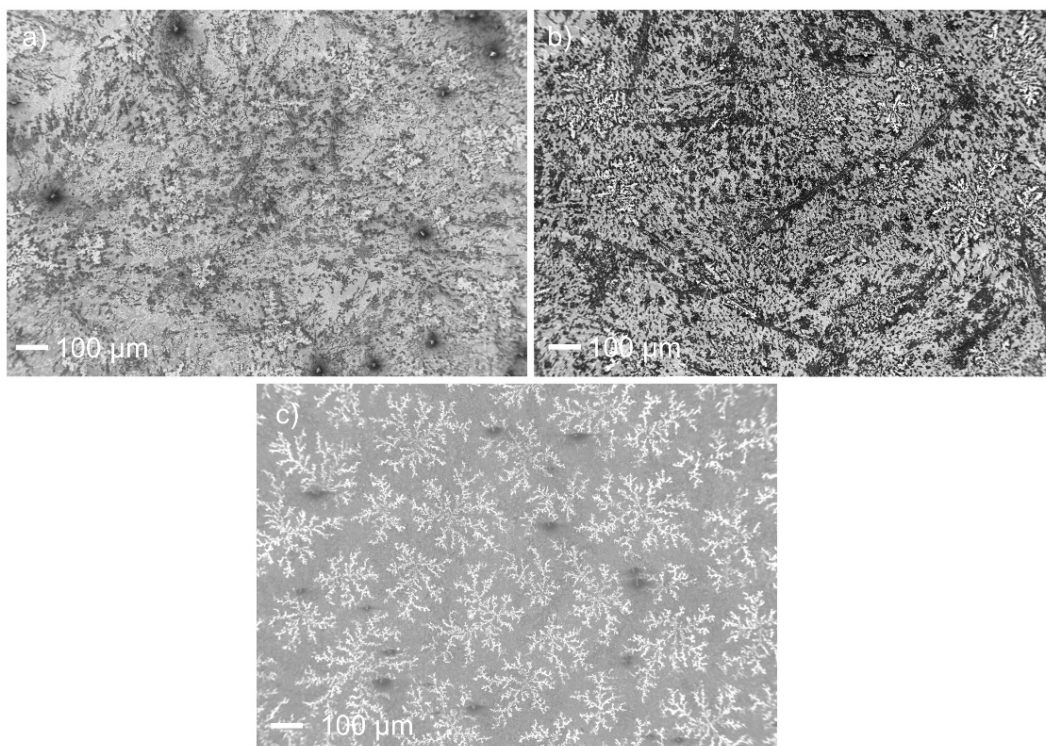
Fig. 47 Surface morphologies of the corroded samples after corrosion test for 100h in the oxidizing-chlorine containing atmosphere: (a) 0Fe; (b) 4Fe; and (c) 30Fe.
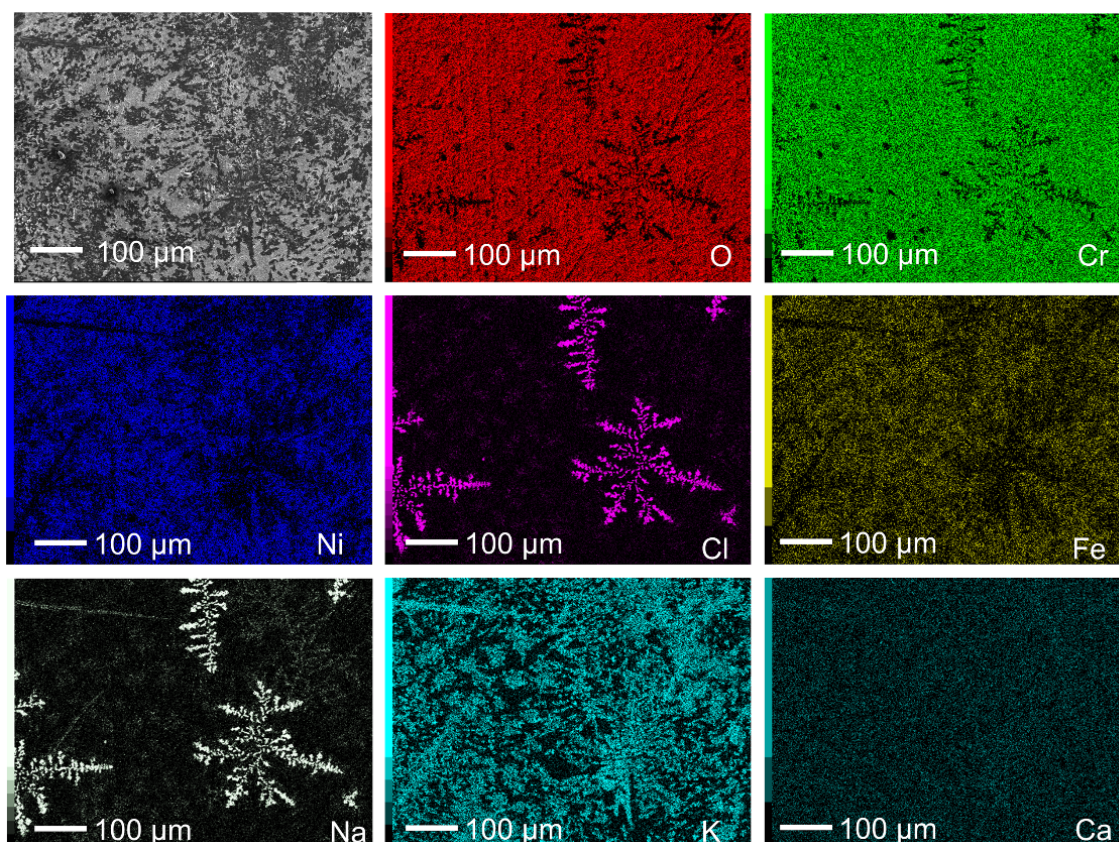
Fig. 48 Surface elemental distribution maps of the corroded sample with 4Fe after 100 h of corrosion in the oxidizing-chlorine containing atmosphere.

Fig. 49 Surface elemental distribution maps of corroded sample with 30Fe after 100 h of corrosion in the oxidizing-chlorine containing atmosphere.
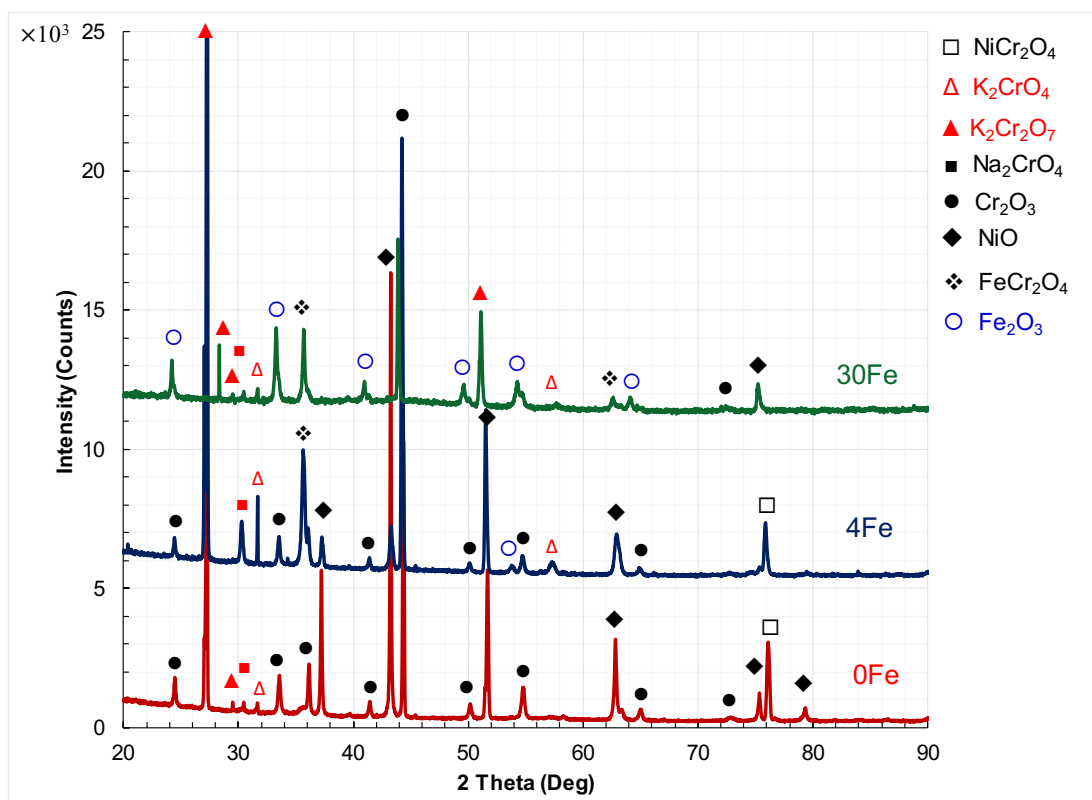
Fig. 50 XRD profiles of the Ni20Cr-xFe alloys after 100h of corrosion in the oxidizing-chlorine containing atmosphere.

6.2.3   Cross-Sectional Observation of Corroded Samples

Cross-sections of the samples after corrosion test for 25, 50 and 100 h in the oxidizing-chlorine containing atmosphere are shown in Fig. 51. All of the alloys exhibited a similar oxide scale structure, including an internal precipitation zone beneath the oxide scale. The oxide scales formed on the Fe-containing alloys were thinner than those of the Fe-free alloy, and their thickness decreased with increasing Fe contents until at least 50 h of corrosion. However, the oxide scale formed on 30 wt.% Fe alloy was thicker than that formed on the 4 wt.% Fe alloy after 100 h of corrosion.
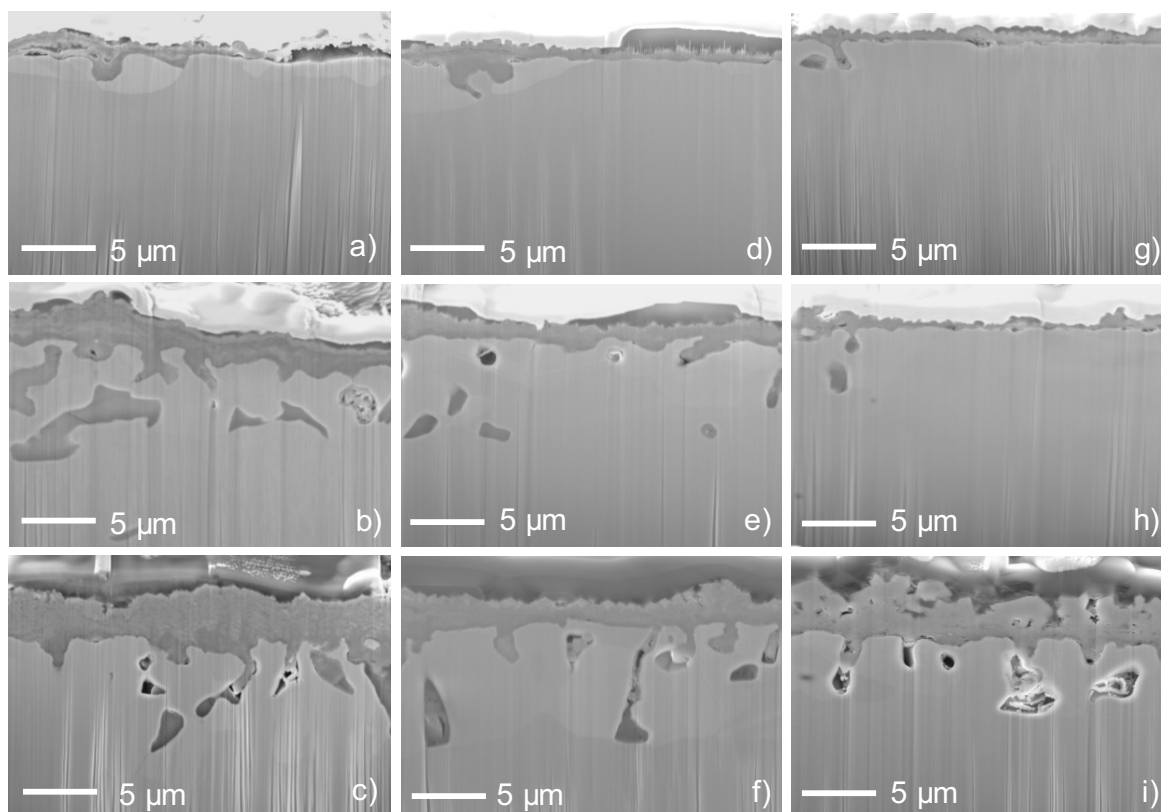
Fig. 51 Cross-sections of the Ni20Cr-xFe alloys after various of corrosion times in the oxidizing-chlorine containing atmosphere: a) 0Fe 25 h; b) 0Fe 50 h; c) 0Fe 100 h; d) 4Fe 25 h; e) 4Fe 50 h; f) 4Fe 100 h; g) 30Fe 25 h; h) 30Fe 50 h; and i) 30Fe 100 h.

As shown in Figs. 25, 52 and 53, EDS mapping revealed that a Ni-rich Cr-containing oxide scale was formed on the Fe-free alloy and a NiCr-Fe containing oxide scale was formed on the 4 w% Fe alloy, whereas, an Fe rich-Cr containing oxide was formed on the 30 wt.% Fe alloy. Fe addition suppressed the amount of Ni-containing within the oxide scale. Beneath these complex oxide scales, a Cr-rich oxide layer developed in all of the alloys. The Cr-rich oxide layer formed on the Fe-free alloy appeared discontinuous, whereas this layer was continuous for the alloys with higher Fe content. As expected from the surface analysis (Figs. 48 and 49) and the XRD profile (Fig. 50), the presence of potassium chromate was confirmed above the outer oxide layer formed on all of the alloys. The internal precipitation zone beneath the oxide scale on all of the alloys consisted of two parts, outer subsurface Cr-oxide penetration and inner internal Cr-chloride precipitates. A Cr-depletion zone was well developed in the alloys. Although, no Cl signal was detected beneath the oxide scale in Fig. 53 for the 30 wt.% Fe alloy, Cr-chloride precipitates were observed in other localized areas where the outer oxide scale grew thicker, as shown in Fig. 54. The observation of these two different areas in the 30 wt.% Fe alloy suggests that internal Cr-chloride formation increased the growth rate of the outer Fe-rich oxide scale. The thickness of these zones of internal oxidation/chlorination and Cr-depletion decreased with increasing Fe content.

Fig. 52 Cross‑sectional elemental distribution maps of the 4Fe alloy after 100 h of corrosion in the oxidizing-chlorine containing atmosphere.

Fig. 53 Cross‑sectional elemental distribution maps of the 30Fe alloy after 100 h of corrosion in the oxidizing-chlorine containing atmosphere.
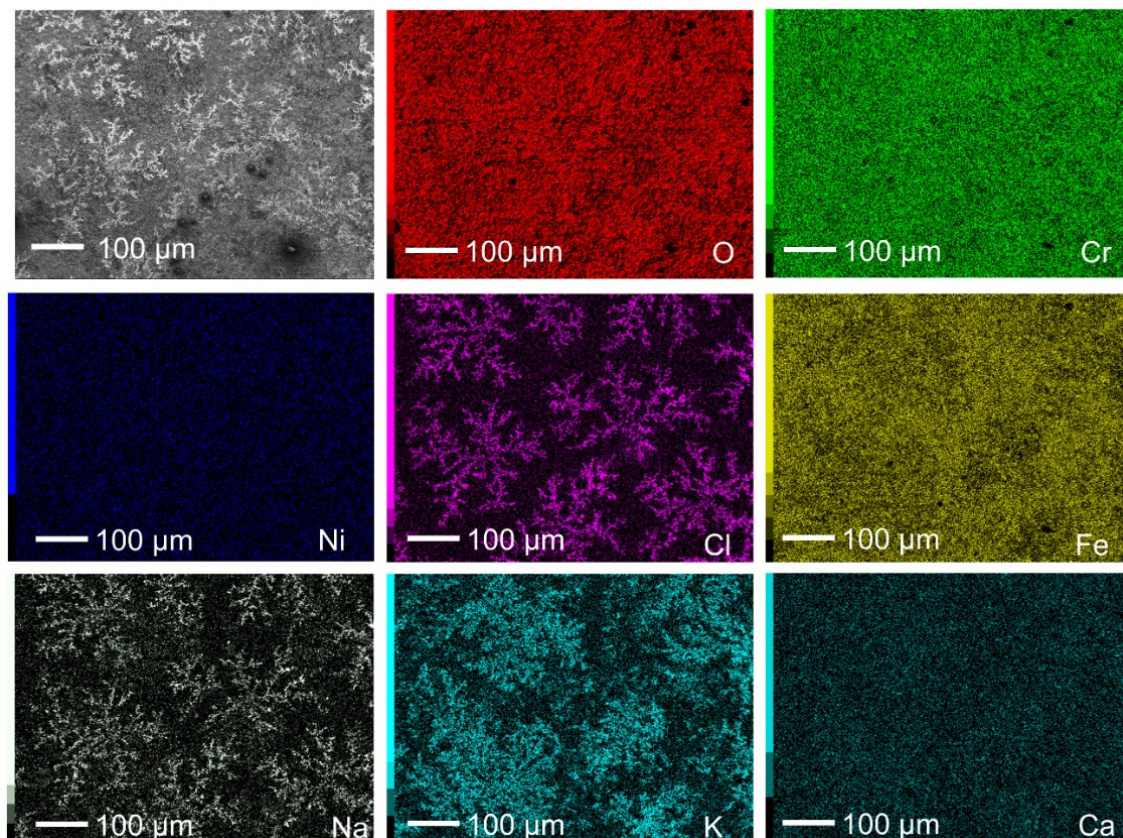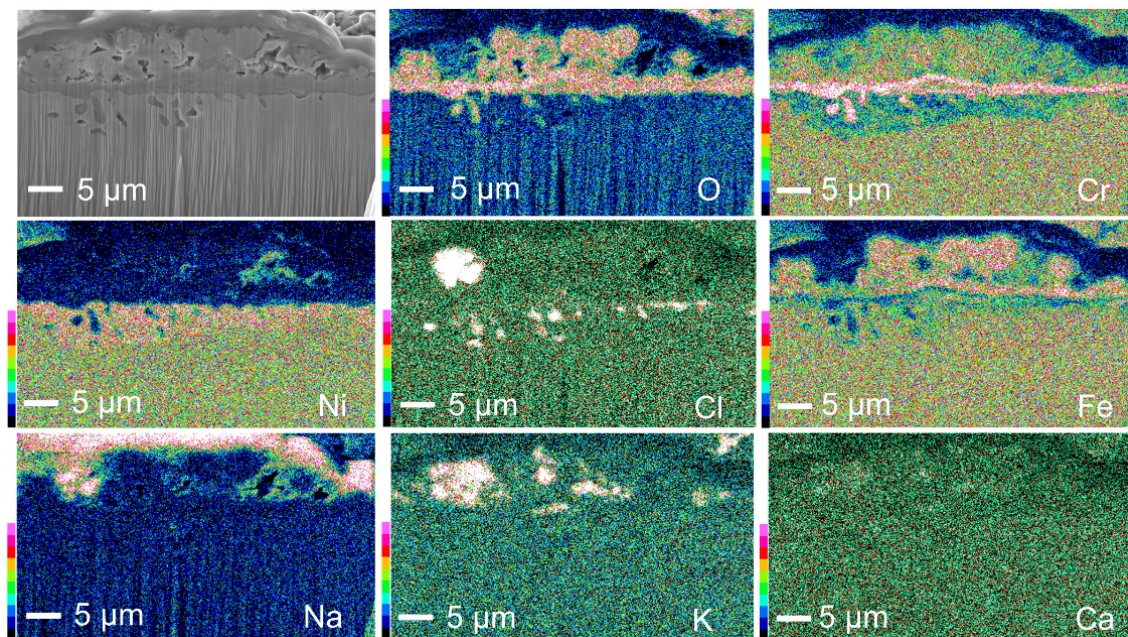

Fig. 54 Cross‑sectional elemental distribution maps of a localized area of the 30Fe alloy after 100 h of corrosion in the oxidizing-chlorine containing atmosphere.

Figure 55 presents the internal chlorination kinetics. The internal chlorination zone was defined as the region from the oxide/alloy interface to the tips of the internal chloride precipitates. The kinetics of internal oxidation/chlorination were initially slow up to approximately 25 h and then exhibited parabolic-like behavior for longer corrosion times. The growth rate of the internal oxidation/chlorination zone decreased with increasing Fe

content, which may indicate that the penetration of chlorine into the alloy substrate decreased with Fe addition.
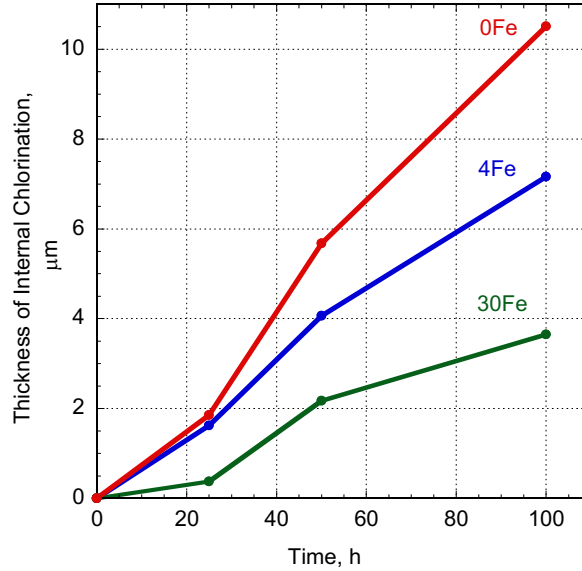
Fig. 55 Thickness of the internal chlorination zones of the Ni20Cr-xFe alloys during corrosion test at 570°C for 100 h in the oxidizing-chlorine containing atmosphere.

6.3 Discussion

The Fe-containing alloys were found to perform better corrosion resistance superior to that of the binary Ni20Cr alloy in an atmosphere containing air and salt-vapor at 570 °C, which demonstrates that Fe addition is beneficial for improving the corrosion resistance of Ni20Cr-based alloys in chlorine-containing oxidizing-chlorine containing atmospheres.

As we discussed in previous chapter 3, the calculated chlorine potential (P_{Cl_2}) during the corrosion tests, as estimated using FactSage software was 3.7×10^{-6} atm. the "quasi"-stability diagrams for oxides and chlorides on Ni20Cr alloys with and without Fe are presented in Fig. 56, using the calculated $P_{Cl_2} = 3.7 \times 10^{-6}$ atm in the atmosphere and the activities of each element in the alloys (Ni20Cr: a_{Ni}= 0.5718, a_{Cr}= 0.1406; Ni20Cr-30Fe: a_{Ni}= 0.2316, a_{Cr}= 0.3277, a_{Fe}=0.3055). As mentioned earlier, the regions of the gas phases of the metal chlorides and oxychlorides in these diagrams indicate only a gas potential of greater than 9.87×10^{-5} atm, which was proposed to be the critical pressure for affecting the corrosion behavior, corresponding to a metal consumption rate of 1 mm·y^{-1} [27]. The horizontal (or diagonal) lines for metal chlorides and oxychloride does not mean to separate

the stable areas between metal and volatilized products. Thus, it does not indicate that chlorination is not occurred below the horizontal lines, i.e., below these lines, the volatile corrosion products are still being formed but to a lesser extent.
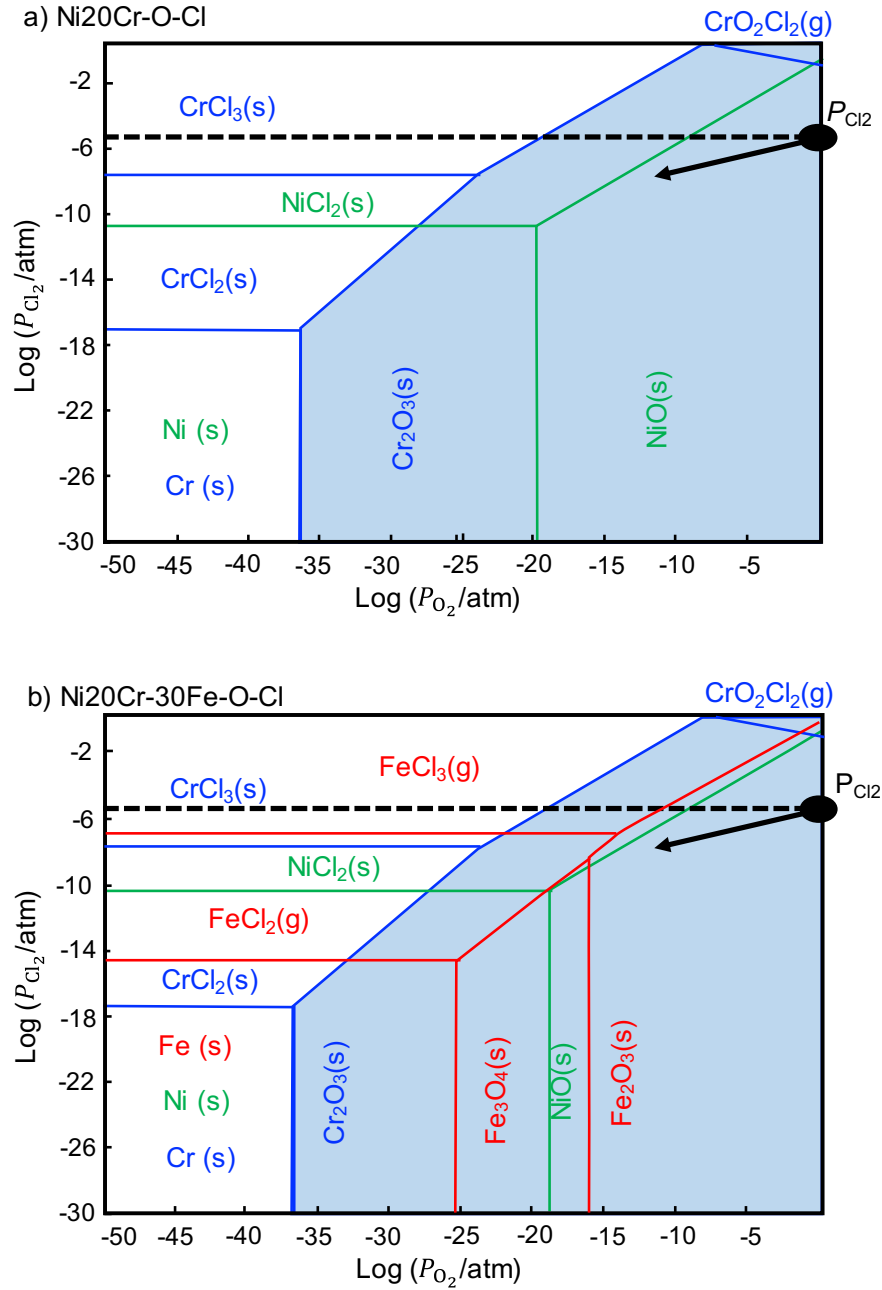
Fig. 56 Quasi-stability diagrams of Ni20Cr-xFe alloys at 570°C: a) 0Fe (a_{Ni}= 0.5718, a_{Cr}= 0.1406); b) 30Fe (a_{Ni}= 0.2316, a_{Cr}= 0.3277, a_{Fe}=0.3055) in the oxidizing-chlorine containing atmosphere (P_{O_2}= 0.2 atm, P_{Cl_2} = 3.7 x 10^{-6} atm, and $P_{MCl_2(g)}$ = 9.87 x 10^{-5} atm).

The P_{Cl_2} in the atmosphere used in this study was insufficient to form the chlorides, which have higher vapor pressures than the critical pressures; thus, it can be expected that

oxides should be formed initially, same as happened during previous corrosion test for Ni20Cr-xMo alloys. In fact, cross-sections of the 30 wt.% Fe alloy after 4 h of corrosion indicated the formation of Fe rich-Cr oxide nodules, as shown in Fig. 57. Although the oxide scale was too thin to observe via FE-SEM, the protective Cr rich oxide layer is expected to form beneath these nodules. This oxide structure is similar to that observed in a previous study for oxidation of Fe-20Cr-34Ni alloy at 600ºC [70]. As it mentioned previously, the formation of a protective Cr_2O_3 scale on an Fe-free alloy during oxidation in air was confirmed, thus, the difference in the oxidation behavior of alloys with and without Fe addition is the formation of Fe-rich oxide nodules on the Fe-containing alloys.
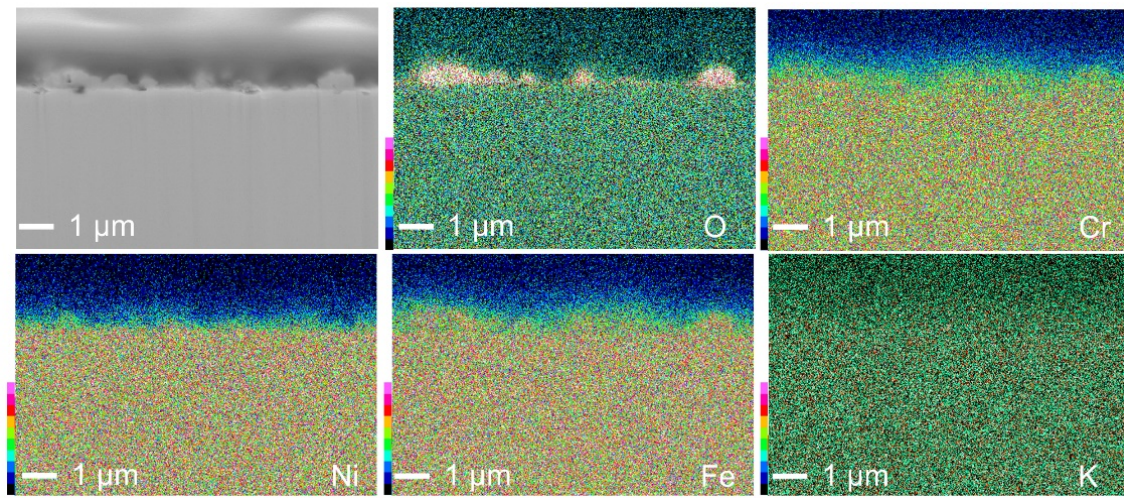
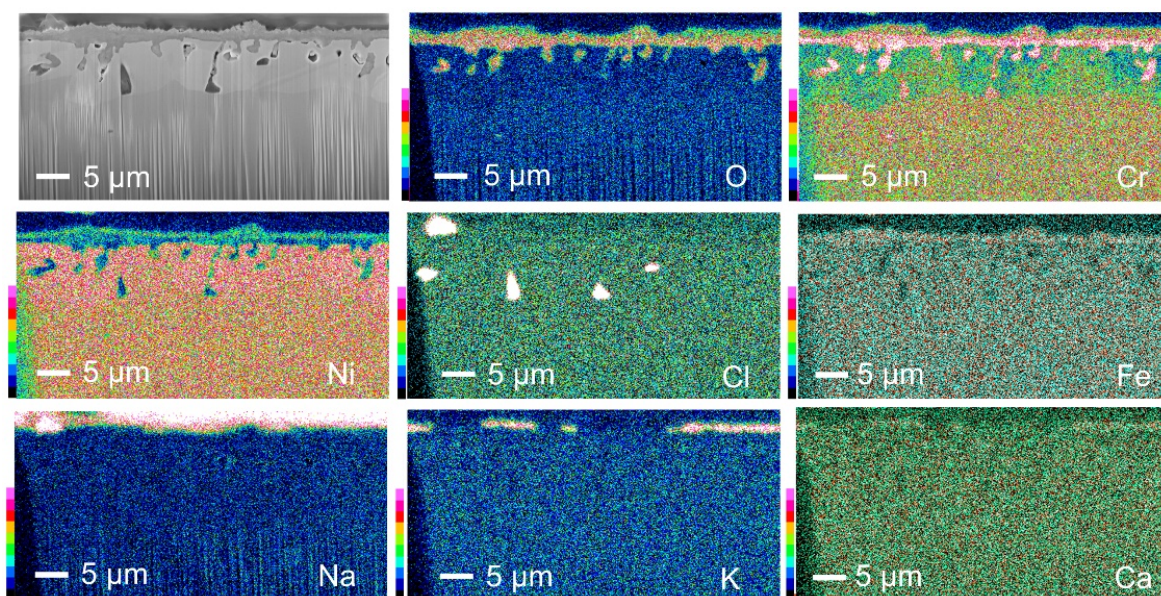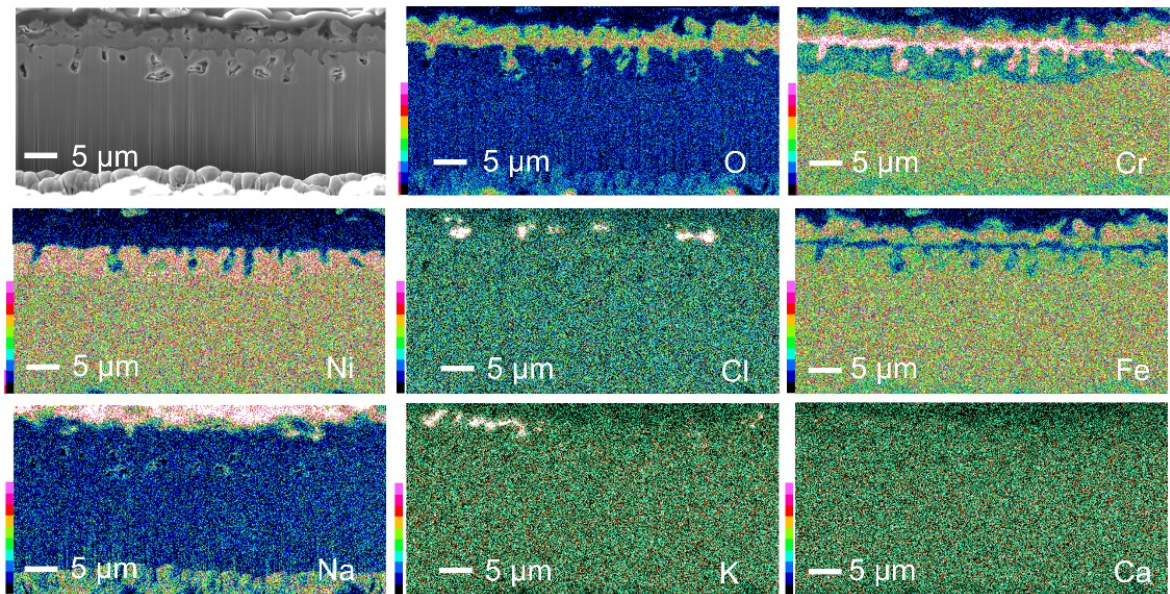

Fig. 57 Cross‑sectional elemental distribution maps of the 30Fe alloy after 4 h of corrosion in the oxidizing-chlorine containing atmosphere.

Dendritic deposits of NaCl were observed on the surfaces of all of the alloys. The formation of these deposits was ascribed to the condensation of salt-vapor at the oxide scale surface. However, potassium was not detected in these deposits, which indicates that this element was consumed by the formation of chromate according to the following reactions:

$$4KCl(g) + Cr_2O_3 (s) + 5/2O_2(g) \rightarrow 2K_2CrO4(s) + 2Cl_2(g) \tag{16}$$

ΔG (16) = -71.771 kJmol^{-1}

$$2KCl(g) + Cr_2O_3 (s) + 2O_2(g) \rightarrow K_2Cr_2O_7(s) + Cl_2(g) \tag{17}$$
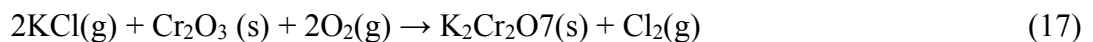
Because no thermodynamic data for reaction (17) could be found in the literature, we will limit our discussion to reaction (16).

Potassium chromate formation generates chlorine, which increases the local chlorine potential at the potassium chromate/Cr_2O_3 interface. The chlorine potential due to a potassium chromate formation was calculated to be $P_{Cl_2} = 1.11 \times 10^{-5}$ atm at 570 °C under the assumption that the vapor pressure of KCl, P_{KCl} is 1.56×10^{-6} atm at equilibrium in a static atmosphere. This calculated chlorine potential is approximately three times higher than that in the furnace atmosphere, which could directly affect the alloy surface because the Cr_2O_3 was consumed by potassium chromate formation, resulting in enhanced internal chlorination in the alloy.

From the results of corrosion of Ni20Cr-xFe alloys, potassium chromate formation was confirmed from the EDS mapping shown in Figs. 48, 49, and 52-54. Moreover, K_2CrO_4, $K_2Cr_2O_7$, and Na_2CrO_4 were identified in the XRD patterns shown in Fig. 50. Unfortunately, ΔG value for $K_2Cr_2O_7$ formation could not be calculated owing to the absence of this reaction in thermodynamic databases. Thus, Fe addition did not completely suppress the formation of chromates, which resulted in an increased local P_{Cl_2} at the oxide scale surface due to reactions (16) and (17). Moreover, the Cr activities in Ni20Cr and Ni20Cr-30Fe alloys were 0.14 and 0.33, respectively, as calculated using FactSage software [65]. Thus, the alloy with a higher Fe content is more likely to form internal Cr-chloride precipitates. However, as mentioned above, the formation of internal Cr-chloride decreased, and the internal oxidation/chlorination kinetics was also decreased with increasing Fe content (Figs. 51 and 55). Thus, it is reasonable to consider that chlorine penetration into the alloy substrate decreased with Fe addition. The areas of potassium chromate tended to decrease with increasing Fe content, suggesting that Fe addition inhibited chromate formation.

The reactions between salt-vapor (KCl and NaCl) and Fe_2O_3, as described by the reactions (18) and (19), are thermodynamically less favorable than those involving Cr_2O_3 [65].

$$2KCl(g) + Fe_2O_3(s) + 1/2O_2(g) \rightarrow 2KFeO_2(s) + Cl_2 (g) \qquad (18)$$
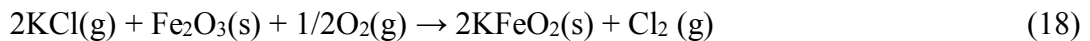
$$\Delta G \text{ (18)} = 168.365 \text{ kJmol}^{-1} \text{ (at 570 °C)}$$

$$2NaCl(g) + Fe_2O_3(s) + 1/2O_2(g) \rightarrow 2NaFeO_2(s) + Cl_2 (g) \qquad (19)$$

$$\Delta G \text{ (19)} = 97.211 \text{ kJmol}^{-1} \text{ (at 570 °C)}$$

NaCl, KCl (g)

Cr$_2$O$_3$

Ni-Cr

a)

NaCl, KCl (g)

Fe rich-Cr Oxide
Cr rich-Fe Oxide

Ni-20Cr-30Fe

d)

K$_2$CrO$_4$/K$_2$Cr$_2$O$_7$
Cr$_2$O$_3$

Cl$_2$

Cr depleted

Cr-Chloride
Cr$_2$O$_3$
Ni-Cr

b)

K$_2$CrO$_4$/K$_2$Cr$_2$O$_7$

Fe rich-Cr Oxide
Cr$_2$O$_3$

Cl$_2$

Cr depleted

Cr-Chloride
Cr$_2$O$_3$
Ni-20Cr-30Fe

e)

K$_2$CrO$_4$/K$_2$Cr$_2$O$_7$

NiCr$_2$O$_4$

Ni

Cr depleted

Ni-Cr

c)

Fe rich-Cr Oxide
K$_2$CrO$_4$/K$_2$Cr$_2$O$_7$
Cr$_2$O$_3$

Fe

Cr depleted

Ni-20Cr-30Fe

f)
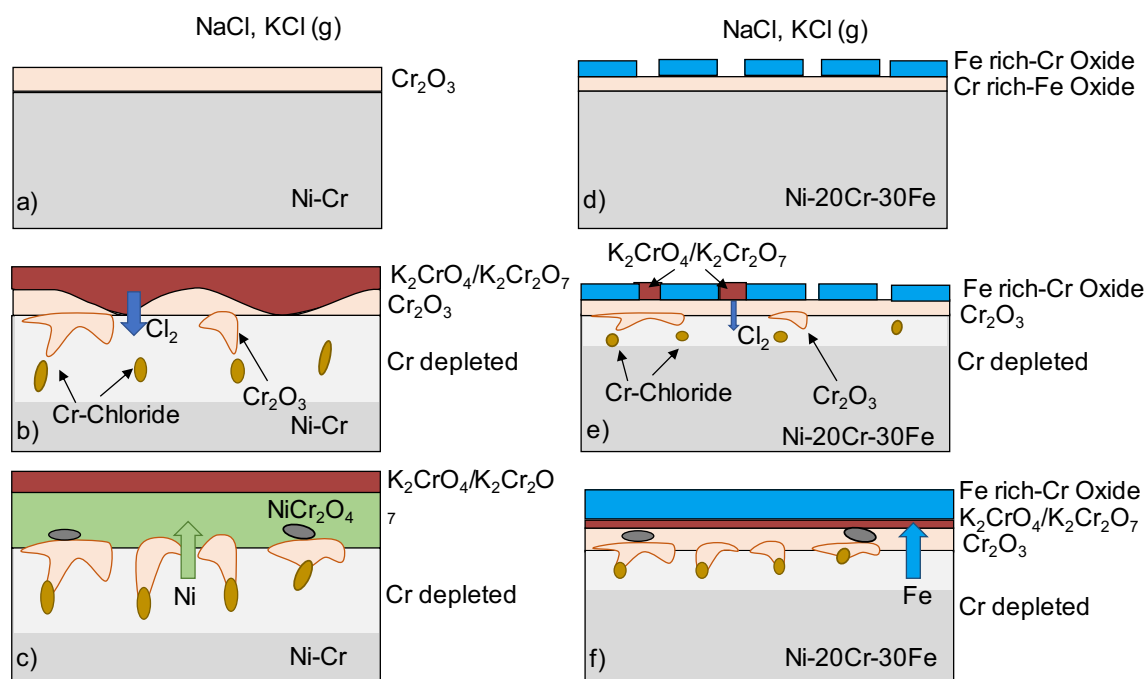
Fig. 58 Proposed model for the corrosion of Ni20Cr alloys with and without Fe addition in an atmosphere containing air and salt-vapor.

Therefore, once Fe$_2$O$_3$ had formed on the alloy substrate, it prevented the formation of chromates on the Cr$_2$O$_3$ scale surface and thus the increase in local chlorine potential. Figure 59 shows a proposed model for the corrosion of Ni20Cr alloy and the effect of Fe addition on the corrosion behavior. In the initial stage of corrosion, a Cr-rich oxide scale is formed on the Fe-free alloy (Fig. 58a), whereas Fe-rich nodules are formed on the Cr$_2$O$_3$ scale of Fe-containing alloys (Fig. 58d). The Fe content in the Cr-rich oxide scale or the number of Fe-rich nodules increases with increasing Fe content. The internal oxidation and chlorination of Cr does not occur or proceeds only very slowly during this initial oxidation stage up to approximately 25 h, because the chlorine potential at the scale/alloy interface remains low. Chromates formation then occurs on both the Fe-free alloy and Fe-containing alloys, mainly via reactions (16) and (17), which increases the local P_{Cl_2} the chromate/oxide interface. The generated Cl$_2$ migrates through cracks and/or pores in the oxide scale and penetrates into the alloy substrate, leading to chlorination of the alloy and resulting in the formation of internal Cr-chloride precipitates, which consumes the Cr in the subsurface region to form a Cr-depletion zone (Figs. 58b and e). However, the areas of chromate formation are limited on the Fe-containing alloys. Because there is less chromate formation on the alloys with the higher Fe content, the P_{Cl_2} at the surface does not increase, which

results in slower internal oxidation/chlorination kinetics and a thinner Cr-depletion zone. Greater metal chloride formation on the Fe-free alloy results in higher evaporation of Cr-chloride, as shown in Fig. 35. Since the Cr-depletion of the alloys with higher Fe content is low owing to reduced internal chlorination, these alloys can maintain a continuous Cr_2O_3 scale beneath the Fe-rich oxide scale (Figs. 52 and 53), which is favorable for reducing the corrosion kinetics of the alloy.

6.4　Conclusion

The corrosion behavior of Ni20Cr alloys containing various Fe contents (0, 4, or 30 wt.%) was investigated. The obtained results can be summarized as follows:

1) Fe addition to Ni20Cr alloy led to improve the corrosion resistance in an oxidizing chlorine-containing environment.

2) Ni20Cr alloys with different Fe contents exhibited an oxide scale structure and internal precipitation zone similar to those in the Fe-free alloy, albeit with reduced internal Cr-chloride penetration and a thinner Cr-depletion zone.

3) For the Fe-containing alloys, Fe-oxide formation above the Cr_2O_3 scale inhibited chromate formation and maintained a low chlorine potential at the alloy surface. Thus, the protective Cr_2O_3 scale could be maintained for a longer corrosion period.

CHAPTER 7
GENERAL SUMMARY

The corrosion behavior of Ni20Cr-based Alloys with different Fe and or Mo additions in the oxidizing-chlorine containing atmosphere was studied in this research, and the effects of Fe or Mo addition were systematically evaluated. The results obtained in this study can be summarized as follows:

1. In the oxidizing chlorine containing atmosphere with air and salt vapor:
    a. Combination of Mo and Fe addition gives better corrosion resistance to the Ni20Cr-based alloys. The corrosion performance was found to be improved with increased both Mo and Fe contents.
    b. The binary Ni20Cr alloy was corroded with highest corrosion rate. The corrosion behavior of the binary Ni20Cr alloy was heavily affected by chromate formation at the beginning of corrosion leading higher chlorine potential at the chromate/Cr_2O_3 interface and resulted in the internal precipitation of chromium chloride and a Cr-depleted zone.
    c. Mo addition to Ni20Cr alloy has given better the corrosion resistance in the oxidizing chlorine-containing environment. Mo addition promoted the formation of NiO scale, which prevented the production of chromate.
    d. Fe addition to Ni20Cr alloy also has given better to improve the corrosion resistance in an oxidizing chlorine-containing environment. Fe oxide in the outer scale could inhibit chromate formation and maintained a low chlorine potential at the alloy surface. Thus, the protective Cr_2O_3 scale could be maintained for a longer corrosion period.

2. In the low oxidizing chlorine containing atmosphere with Ar and salt vapor:
    a. The Ni20Cr-based alloy has better corrosion performance in this low oxidizing-chlorine containing atmosphere than that of the Mo containing alloys. No chromate and internal Cr-precipitation zone were formed on the all of alloys.
    b. The Mo-free alloys formed thin continuous protective Cr_2O_3 scale after the corrosion. Meanwhile, a dense NiO outer scale and a dense inner oxide layer

with "island-bridges" structures formed on Mo containing alloys after the corrosion.

3. The proposed corrosion mechanism has been confirmed that chromate formation is highly detrimental for the corrosion performance of the chromia-forming alloys in the oxidizing salt-vapor containing atmospheres.

REFERENCES

[1]   D. Hoornweg and P. Bhada-Tata, "What a Waste : A Global Review of Solid Waste Management," World Bank, Washington, DC, 2012. [Online]. Available: https://openknowledge.worldbank.org/handle/10986/17388.

[2]   L. Makarichi, W. Jutidamrongphan, and K. Techato, "The evolution of waste-to-energy incineration: A review," *Renewable and Sustainable Energy Reviews*, 91, November 2017, 812–821, 2018.

[3]   J. W. Lu, S. Zhang, J. Hai, and M. Lei, "Status and perspectives of municipal solid waste incineration in China: A comparison with developed regions," *Waste Management*, 69, 170–186, 2017.

[4]   IRENA, *Renewable Energy Statistics 2019*, 1, 1. 2019.

[5]   A. Kumar and S. R. Samadder, "A review on technological options of waste to energy for effective management of municipal solid waste," *Waste Management*, 69, 407–422, 2017.

[6]   L. Lombardi, E. Carnevale, and A. Corti, "A review of technologies and performances of thermal treatment systems for energy recovery from waste," *Waste Management*, 37, 26–44, 2015.

[7]   S. Iannello, S. Morrin, and M. Materazzi, "Fluidised bed reactors for the thermochemical conversion of biomass and waste†," *KONA Powder and Particle Journal*, 37, 37, 114–131, 2020.

[8]   Y. Kawahara, Kawahara, and Yuuzou, "An Overview on Corrosion-Resistant Coating Technologies in Biomass/Waste-to-Energy Plants in Recent Decades," *Coatings*, 6, 3, 34, 2016.

[9]   P. H. Brunner and H. Rechberger, "Waste to energy - key element for sustainable waste management," *Waste Management*, 37, 3–12, 2015.

[10]   M. Noguchi and H. Yakuwa, "Lecture on Fundamental Aspects of High Temperature Corrosion and Corrosion Protection Part 3: High Temperature Corrosion and Corrosion Protection of the Boilers in Waste to Energy Plants," Tokyo, Japan, 2017. Accessed: Nov.   28,   2019.   [Online].   Available:

https://www.ebara.co.jp/en/about/technologies/abstract/detail/1220901_4377.html.

[11] T. Hirose, S. Kosugi, T. Hirota, Y. Makiyama, T. Ohshita, and N. Inumaru, "Characteristics of the internally circulating Fluidized bed Boiler," *Proceedings of the International Conference on Fluidized Bed Combustion*, 2, 559–570, 1991.

[12] W. R. Niessen, *Combustion and Incineration Process: Application in Environmental Engineering*, 4th Editio. CRC Press, 2010.

[13] E. Alakangas *et al.*, *Biomass Technology Roadmap*. The European Technology Platform on Renewable Heating and Cooling, 2014.

[14] A. J. Pedersen *et al.*, "A full-scale study on the partitioning of trace elements in municipal solid waste incinerations-Effects of firing different waste types," *Energy and Fuels*, 23, 7, 3475–3489, 2009.

[15] S. R. Frederik Neuwahl, Gianluca Cusano, Jorge Gómez Benavides, Simon Holbrook, "Best Available Techniques (BAT) Reference Document for Waste Treatment Industries: : Industrial Emissions Directive 2010/75/EU (Integrated Pollution Prevention and Control), EUR 29971 EN," Publications Office of the European Union, Luxembourg, 2019.

[16] G. Sorell, "The role of chlorine in high temperature corrosion in waste-to-energy plants," *Materials at High Temperatures*, 14, 3, 207–220, 1997.

[17] K. O. Davidsson *et al.*, "Potassium, chlorine, and sulfur in ash, particles, deposits, and corrosion during wood combustion in a circulating fluidized-bed boiler," *Energy and Fuels*, 21, 1, 71–81, 2007.

[18] S. H. Lee, N. J. Themelis, and M. J. Castaldi, "High-temperature corrosion in waste-to-energy boilers," *Journal of Thermal Spray Technology*, 16, 1, 104–110, 2007.

[19] D. A. Tillman, D. Duong, and B. Miller, "Chlorine in solid fuels fired in pulverized fuel boilerss-sources, forms, reactions, and consequences: A literature review," *Energy and Fuels*, 23, 7. American Chemical Society, 3379–3391, Jul. 16, 2009.

[20] P. Lu, Q. Huang, A. C. (Thanos) Bourtsalas, N. J. Themelis, Y. Chi, and J. Yan, "Review on fate of chlorine during thermal processing of solid wastes," *Journal of Environmental Sciences*, 78, 13–28, 2019.

[21] Z. Abbas, A. P. Moghaddam, and B. M. Steenari, "Release of salts from municipal

solid waste combustion residues," *Waste Management*, 23, 4, 291–305, 2003.

[22]   J. Zhao, X. Wei, T. Li, H. Li, and F. Bin, "Behavior of Alkali Metals in Fly Ash during Waste Heat Recovery for Municipal Solid Waste Incineration," *Energy and Fuels*, 32, 4, 4417–4423, 2018.

[23]   K. TSUKAMOTO, S. WATANABE, and E. ISHIKAWA, "Biomass Power Plant ICFB for Nakoso Mill, Nippon Paper Industries Co., Ltd.," 2004. [Online]. Available: https://www.ebara.co.jp/about/technologies/abstract/detail/__icsFiles/afieldfile/2016 /04/25/208_P32.pdf.

[24]   H. P. P. Nielsen, F. J. J. Frandsen, K. Dam-Johansen, and L. L. L. Baxter, "Implications of chlorine-associated corrosion on the operation of biomass-fired boilers," *Progress in Energy and Combustion Science*, 26, 3, 283–298, 2000.

[25]   W. Ma and S. Rotter, "Overview on the chlorine origin of MSW and Cl-originated corrosion during MSW & RDF combustion process," in *2nd International Conference on Bioinformatics and Biomedical Engineering, iCBBE 2008*, May 2008, 4255–4258.

[26]   J. Liu, D. Dyson, and E. Asselin, "Long-term Hot Corrosion Behavior of Boiler Tube Alloys in Waste-to-Energy Plants," *Oxidation of Metals*, 86, 1–2, 135–149, 2016.

[27]   R. Bender and M. Schütze, "The role of alloying elements in commercial alloys for corrosion resistance in oxidizing-chloridizing atmospheres. Part I: Literature evaluation and thermodynamic calculations on phase stabilities," *Materials and Corrosion*, 54, 8, 567–586, 2003.

[28]   R. Bender and M. Schütze, "The role of alloying elements in commercial alloys for corrosion resistance in oxidizing-chloridizing atmospheres. Part II: Experimental investigations," *Materials and Corrosion*, 54, 9, 652–686, 2003.

[29]   Y. Y. Lee and M. J. McNallan, "Ignition of nickel in environments containing oxygen and chlorine," *Metallurgical and Materials Transactions A*, 18, 6, 1099–1107, 1987.

[30]   H. J. Grabke, E. Reese, and M. Spiegel, "The effects of chlorides, hydrogen chloride, and sulfur dioxide in the oxidation of steels below deposits," *Corrosion Science*, 37, 7, 1023–1043, 1995.

[31]   A. Zahs, M. Spiegel, and H. J. Grabke, "Chloridation and oxidation of iron, chromium, nickel and their alloys in chloridizing and oxidizing atmospheres at 400–

700°C," *Corrosion Science*, 42, 6, 1093–1122, 2000.

[32] Y. Shinata, "Accelerated oxidation rate of chromium induced by sodium chloride," *Oxidation of Metals*, 27, 5–6, 315–332, 1987.

[33] J. Pettersson, H. Asteman, J.-E. Svensson, and L.-G. Johansson, "KCl Induced Corrosion of a 304-type Austenitic Stainless Steel at 600°C; The Role of Potassium," *Oxidation of Metals*, 64, 1–2, 23–41, 2005.

[34] Y. S. Li, M. Spiegel, and S. Shimada, "Corrosion behaviour of various model alloys with NaCl–KCl coating," *Materials Chemistry and Physics*, 93, 1, 217–223, 2005.

[35] S. Karlsson, J. Pettersson, L. G. Johansson, and J. E. Svensson, "Alkali Induced High Temperature Corrosion of Stainless Steel: The Influence of NaCl, KCl and CaCl2," *Oxidation of Metals*, 78, 1–2, 83–102, 2012.

[36] E. Sadeghimeresht, L. Reddy, T. Hussain, N. Markocsan, and S. Joshi, "Chlorine-induced high temperature corrosion of HVAF-sprayed Ni-based alumina and chromia forming coatings," *Corrosion Science*, 132, 170–184, 2018.

[37] V. A. C. Haanappel and P. J. Gellings, "Chlorine-induced high temperature corrosion: Ii. The tedmon equation as a theoretical approach of the kinetics," *High Temperature Materials and Processes*, 10, 2, 91–100, 1992.

[38] S. Y. Lee, "Inhibition of Oxidation of Iron in Environments Containing Chlorine at 1100 and 1200 K," *Journal of The Electrochemical Society*, 137, 2, 472, 1990.

[39] D. J. Young, *High Temperature Oxidation and Corrosion of Metals: Second Edition*. 2016.

[40] M. J. McNallan, "Oxidation-Chlorination of Binary NiCr Alloys in Flowing Ar-O[sub 2]-Cl[sub 2] Gas Mixtures at 1200 K," *Journal of The Electrochemical Society*, 138, 12, 3692, 1991.

[41] M. C. Galetz, B. Rammer, and M. Schütze, "Refractory metals and nickel in high temperature chlorine-containing environments - thermodynamic prediction of volatile corrosion products and surface reaction mechanisms: a review," *Materials and Corrosion*, 66, 11, 1206–1214, 2015.

[42] A. S. Kim and M. J. McNallan, "Mixed oxidation of iron-chromium alloys in gases containing oxygen and chlorine at 900 to 1200°K," *Corrosion*, 46, 9, 746–755, 1990.

[43] I. Gaballah, S. Ivanaj, and N. Kanari, "Kinetics of chlorination and oxychlorination of chromium (III) oxide," *Metallurgical and Materials Transactions A: Physical Metallurgy and Materials Science*, 29, 4, 1299–1308, 1998.

[44] G. R. Holcomb, "Calculation of reactive-evaporation rates of chromia," *Oxidation of Metals*, 69, 3–4, 163–180, 2008.

[45] J. Oh, M. McNallan, G. Lai, and M. Rothman, "High temperature corrosion in an environment containing potassium and chlorine," *Metallurgical and Materials Transactions A*, 17, 6, 1087–1094, 1986.

[46] F. H. Stott, R. Prescott, and P. Elliott, "The Corrosion of metals in an oxidizing-chloridizing environment at high temperature," *Materials and Corrosion/Werkstoffe und Korrosion*, 39, 9, 401–405, 1988.

[47] C. Schwalm and M. Schütze, "The corrosion behavior of several heat resistant materials in air + 2 vol-% Cl2 at 300 to 800 °C. Part I - Fe-base and Fe-containing alloys," *Materials and Corrosion*, 51, 1, 34–49, 2000.

[48] C. Pettersson, J. Pettersson, H. Asteman, J.-E. Svensson, and L.-G. Johansson, "KCl-induced high temperature corrosion of the austenitic Fe–Cr–Ni alloys 304L and SaNi20Cro 28 at 600 °C," *Corrosion Science*, 48, 6, 1368–1378, 2006.

[49] S. Kiamehr, K. V. Dahl, M. Montgomery, and M. A. J. Somers, "KCl-induced high temperature corrosion of selected commercial alloys: Part I: chromia-formers," *Materials and Corrosion*, 66, 12, 1414–1429, 2015.

[50] Y. Kawahara, "Application of High Temperature Corrosion-Resistant Materials and Coatings Under Severe Corrosive Environment in Waste-to-Energy Boilers," *Journal of Thermal Spray Technology*, 16, 2, 202–213, 2007.

[51] Y. Lu, W. Chen, and R. Eadie, "Evaluation of high temperature corrosion resistance of a Ni3Al (Mo) alloy," *Intermetallics*, 12, 12, 1299–1304, 2004.

[52] Y. Behnamian *et al.*, "A comparative study of oxide scales grown on stainless steel and nickel-based superalloys in ultra-high temperature supercritical water at 800 °C," *Corrosion Science*, 106, 188–207, 2016.

[53] N. S. Jacobson, M. J. McNallan, and Y. Y. Lee, "Mass spectrometric observations of metal oxychlorides produced by oxidation-chlorination reactions," *Metallurgical*

Transactions A, 20, 8, 1566–1568, 1989.

[54] M. Schütze, "Corrosion Resistance at Elevated Temperatures in Highly Aggressive Environments," *CORROSION*, 63, 1, 4–18, 2007.

[55] H. J. Grabke, A. Zahs, M. Spiegel, H. J. Grabke, A. Zahs, and M. Spiegel, "The influence of alloying elements on the chlorine-induced high temperature corrosion of Fe-Cr alloys in oxidizing atmospheres," *Materials and Corrosion*, 50, 10, 561–578, 1999.

[56] A. Altomare, N. Corriero, C. Cuocci, A. Falcicchio, A. Moliterni, and R. Rizzi, "QUALX2.0: A qualitative phase analysis software using the freely available database POW-COD," *Journal of Applied Crystallography*, 48, 598–603, 2015.

[57] K. Segerdahl, J. Pettersson, J.-E. Svensson, and L.-G. Johansson, "Is KCl(g) corrosive at temperatures above its dew point? Influence of KCl(g) on initial stages of the high temperature corrosion of 11% Cr steel at 600°C," *Materials Science Forum*, 461–464, I, 109–116, 2004.

[58] E. Sadeghimeresht, L. Reddy, T. Hussain, M. Huhtakangas, N. Markocsan, and S. Joshi, "Influence of KCl and HCl on high temperature corrosion of HVAF-sprayed Ni20CrAlY and Ni20CrMo coatings," *Materials and Design*, 148, 17–29, 2018.

[59] S. Chevalier, S. Ched'Homme, A. Bekaddour, K. Amilain-Basset, and L. Buisson, "High temperature alloy chloridation at 850°C. Part I: Comparison of Ni-based and Fe-based alloy behaviour," *Materials and Corrosion*, 58, 4, 254–264, 2007.

[60] J. R. Keiser, W. B. A. Sandy Sharp, and D. L. Singbeil, "Could biomass-fueled boilers be operated at higher steam temperatures? 2. Field tests of candidate superheater alloys," *2013 PEERS Conference, Co-located with the 2013 International Bioenergy and Bioproducts Conference*, 2, August 2014, 1107–1125, 2013.

[61] C. Schwalm and M. Schütze, "The corrosion behavior of several heat resistant materials in air + 2% Cl2 at 300 to 800 °C. Part 2 - Nickel base alloys," *Materials and Corrosion*, 51, 2, 73–79, 2002.

[62] D. W. Yun, H. S. Seo, J. H. Jun, J. M. Lee, and K. Y. Kim, "Molybdenum effect on oxidation resistance and electric conduction of ferritic stainless steel for SOFC interconnect," *International Journal of Hydrogen Energy*, 37, 13, 10328–10336,

2012.

[63] E. Godlewska, "Effect of molybdenum on high-temperature corrosion of Fe-Al intermetallics," *Intermetallics*, 14, 3, 280–286, 2006.

[64] H. J. Grabke *et al.*, "The influence of alloying elements on the chlorine-induced high temperature corrosion of Fe-Cr alloys in oxidizing atmospheres," *Materials and Corrosion*, 50, 10, 561–578, 1999.

[65] C. W. Bale *et al.*, "FactSage thermochemical software and databases, 2010–2016," *Calphad*, 54, 35–53, 2016.

[66] B. H. Zimm and J. E. Mayer, "Vapor pressures, heats of vaporization, and entropies of some alkali halides," *The Journal of Chemical Physics*, 12, 9, 362–369, 1944.

[67] Y. Sato, K. Kawabe, K. Sugawara, and M. Hara, "High temperature corrosion of Ni-5, -8 and -10 at%Al alloys in air with a trace amount of NaCl vapor," *Journal of the Japan Institute of Metals*, 81, 9, 441–446, 2017.

[68] T. Mathews, D. Krishnamurthy, and T. Gnanasekaran, "An electrochemical investigation of the thermodynamic properties of Na2Mo2O7 and Na2NiO2," *Journal of Nuclear Materials*, 247, 280–284, 1997.

[69] H. Izzuddin, S. Hayashi, S. Yoneda, T. Kogin, E. Ishikawa, and M. Noguchi, "Effect of Mo on corrosion behavior of Ni20Cr- *x* Mo alloys in air with NaCl-KCl-CaCl 2 vapor at 570°C," *Materials and Corrosion*, 2020.

[70] W. M. Stobbs and E. Metcalfe, "A microstructural study of the oxidation of Fe-NiCr alloys II. 'Non-protective' oxide growth," *Philosophical Transactions of the Royal Society of London. Series A, Mathematical and Physical Sciences*, 319, 1546, 219–247, 1986.

ACKNOWLEDGEMENTS